Physics Theses & Dissertations   Physics

Fall 2016

Electroproduction of Neutral Pion Off Helium-4

Bayram Torayev
Old Dominion University

ELECTROPRODUCTION OF NEUTRAL PION OFF ^{4}HE

by

Bayram Torayev
B.S. June 2007, Middle East Technical University, Turkey

A Dissertation Submitted to the Faculty of
Old Dominion University in Partial Fulfillment of the
Requirements for the Degree of

DOCTOR OF PHILOSOPHY

PHYSICS

OLD DOMINION UNIVERSITY
December 2016

Approved by:

Stephen Bueltmann (Director)

Sebastian Kuhn (Member)

Rocco Schiavilla (Member)

Alex Godunov (Member)

Jennifer Poutsma (Member)

ABSTRACT

ELECTROPRODUCTION OF NEUTRAL PION OFF ^{4}HE

Bayram Torayev
Old Dominion University, 2016
Director: Dr. Stephen Bueltmann

Deeply virtual exclusive processes offer a unique opportunity to study the internal structure of the nucleon and nuclei. The goal of this work is to extract the beam-spin asymmetry in deeply virtual coherent neutral pion electroproduction, $e^4\text{He} \rightarrow e'^4\text{He}'\pi^0$, using the CLAS detector in the experimental Hall B at Thomas Jefferson National Accelerator Facility. The data were collected in 2009 with a 6 GeV longitudinally polarized electron beam impinging on a 30 cm long, 6 atm Helium-4 gaseous target. In order to ensure that the process is coherent, a new Radial Time Projection Chamber was used to detect and identify low energy recoil α-particles. The Beam Spin Asymmetry in the coherent deep exclusive regime was measured at $Q^2 = 1.50$ GeV^2, $x_B = 0.18$ and $-t = 0.14$ GeV^2. The measured asymmetry has an amplitude of $10\% \pm 5\%$ and has the opposite sign compared the asymmetry measured for π^0 production on the proton.

ACKNOWLEDGEMENTS

TABLE OF CONTENTS

LIST OF TABLES

LIST OF FIGURES

CHAPTER 1

INTRODUCTION

One of the important goals of high energy physics is to understand the internal structure of the nucleon. Electron, photon and hadron scattering processes have been used for decades to explore the nucleon structure. The first electron-proton elastic scattering experiment at SLAC [2] showed that the cross-section calculations do not agree with experimental data when assuming the proton to be a point-like particle. In 1961, Hofstadter proposed that the proton has an internal structure which led him to win the Nobel prize [3]. In the first deep inelastic scattering (DIS) experiments with higher energies at SLAC it had been observed that the cross-section did not show a sharp decrease at large momentum transfer as it had been for elastic scattering (ES). This results revealed that the nucleon contained point-like constituent particles. In the Feynman parton model, these constituent particles were identified as quarks which were introduced by Gell-Man [4]. In DIS experiments with increased statistics and accuracy, it was found that about half of the nucleon momentum was carried by quarks and only about 25% of the nucleon spin was originating from the spin of the quarks. However, still very little is known about the internal structure of the nucleon such as transverse momentum distributions of the quarks and contributions of their angular momentum to the total spin of the nucleon. This information is not possible to access through ES and DIS experiments. Recently, General Parton Distributions (GPDs) were introduced to obtain a unifying picture of the nucleon structure [7, 8, 9].

The GPDs contain information about the distribution of the partons with respect to both longitudinal momentum and transverse position. In addition, theses functions provide correlations of the spatial and momentum distributions and give access to the total angular momentum carried by the partons. It has been proven that hard scattering processes, Deeply Virtual Compton Scattering (DVCS) and Deeply Virtual Meson Production (DVMP), can be factorized into a hard part and soft part in the limit $Q^2 \to \infty$ and fixed x_b and t which leads to the possibility to study GPDs in theses processes. Q^2 is the squared four-momentum of the virtual photon, x_B is the fraction of the momentum held by struck quark and $-t$ is the squared four-momentum transfer to the nucleon. The meson electroproduction process is the subject of this work.

Another model used to describe meson photo production and electroproduction is based on Regge theory [20]. In this model, trajectories are exchanged in the t-channel as mediators of the interaction. The Regge model has been studied for photoproduction where $Q^2 = 0$ and photons are transversely polarized. The extension and applicability of this model to the electroproduction case is so far only limited to vector mesons and charged pseudo-scalar mesons.

The goal of this work is to measure the beam-spin asymmetry in coherent electroproduction of π^0 off a helium-4 target using a longitudinally polarized electron beam. The beam asymmetry originates from the interference of the longitudinal and transverse amplitudes of the virtual photons. This coherent channel is studied using the data collected from the experiment "EG6" at Thomas Jefferson Laboratory by the CLAS collaboration in 2009. In this experiment, a 6 GeV longitudinally polarized electron beam was used to scatter off a 6 atm helium-4 gas target. The final state particles were detected using the CLAS detector, an additional Inner Calorimeter (IC) and a Radial Time Projection Chamber (RTPC).

In the next chapter, we will discuss the physics motivation. The experimental setup and detector calibrations are discussed in chapters 3 and 4. Particle identification and event selection are explained in chapters 5 and 6. The beam-spin asymmetry extraction and systematic uncertainty studies are presented in chapter 7. In chapter 8, we will summarize the work.

CHAPTER 2

PHYSICS MOTIVATION

2.1 ELASTIC SCATTERING

The internal structure of any object can be explored by scattering point-like particles off the constituent particles within the object. The structure of the gold atom has been resolved by Rutherford in 1911. He used α-particles to strike a thin gold foil where α-particles can be assumed to be point-like particle in comparison to gold atoms. By measuring the scattering angles of the particles off the gold atoms, he found the cross-section formula:

$$\frac{d\sigma}{d\Omega} = \frac{\alpha^2}{2(p\beta)^2 \sin^4(\frac{\theta}{2})} \tag{1}$$

where α is the fine structure constant, p and β are momentum and velocity of the α particles. $d\Omega$ is the solid angle into which the α-particles scattered and θ is the scattering angle of the particles in the lab frame. The internal structure of the nucleon can be studied by scattering point-like particles from the nucleon, often leptons are used. One of theses processes is elastic scattering where incoming and outgoing particles are identical. The elastic scattering of the electron off a proton target in the target rest frame is defined as:

$$e(P_e) + p(P_p) \rightarrow e'(P_{e'}) + p'(P_{p'}) \tag{2}$$

where the arguments in the parentheses correspond to the four-momentum vector of each particle. In Fig. 1, the elastic scattering of an electron off a proton is illustrated via virtual photon exchange. The theoretical cross-section of the elastic scattering process, where a relativistic electron is scattered from a point-like particle with charge q was calculated by Mott [1] in 1932 as follows

$$(\frac{d\sigma}{d\Omega})_{Mott} = \frac{\alpha^2}{4E^2 \sin(\frac{\theta}{2})} \frac{E'}{E} \cos^2(\frac{\theta}{2}) \tag{3}$$

where E and E' are the energies of the incident and scattered electron, θ is the scattering angle in the lab frame, α is the fine structure and $d\Omega$ is the solid angle where electrons scatter. However, this calculation failed to agree with the experimental data [2] at large
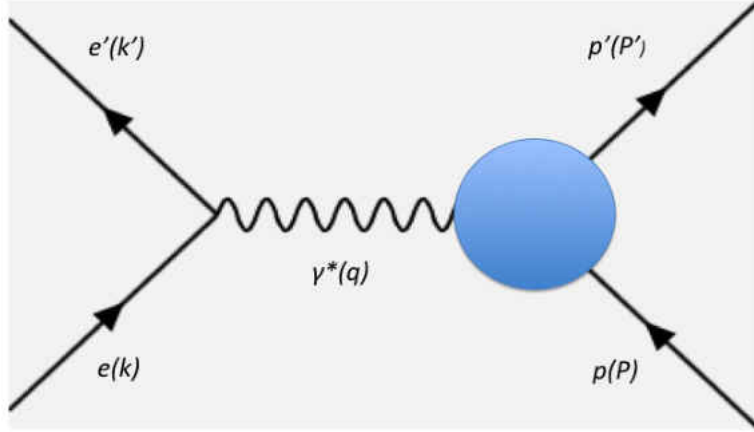
FIG. 1: Illustration of the elastic electron-proton scattering process.

scattering angles as shown in Fig. 2. Other models assuming the proton as a point-like particle disagree with the data, too. As a result, it was introduced by Hofstadter that the proton is not a point-like particle. It has an internal structure [3]. This conclusion led him to win the Nobel prize in 1961.

In 1950, Rosenbluth [1] proposed to use electric and magnetic form factors of the proton to describe the internal structure of the proton and calculated the cross-section of the elastic electron-proton scattering as follows:

$$\frac{d\sigma}{d\Omega}_{ep \to e'p'} = (\frac{d\sigma}{d\Omega})_{Mott} \cdot (\frac{G_E^2(Q^2) + \frac{Q^2}{4 \cdot M^2} \cdot G_M^2(Q^2)}{1 + \frac{Q^2}{4 \cdot M^2}} + \frac{Q^2}{2 \cdot M^2} \cdot G_M^2(Q^2) \cdot \tan^2(\frac{\theta}{2})) \quad (4)$$

where M is the mass of the nucleon, G_E and G_M are electric and magnetic form factors, respectively. Q^2 is the negative squared four-momentum transfer.

$$Q^2 = -q^2 \quad (5)$$

where q is the four-momentum difference of the incident and scattered electron.

2.2 DEEP INELASTIC SCATTERING

Deep inelastic scattering (DIS) is another electron-proton scattering process to investigate the internal structure of the nucleon. In this process, generally only the scattered electron
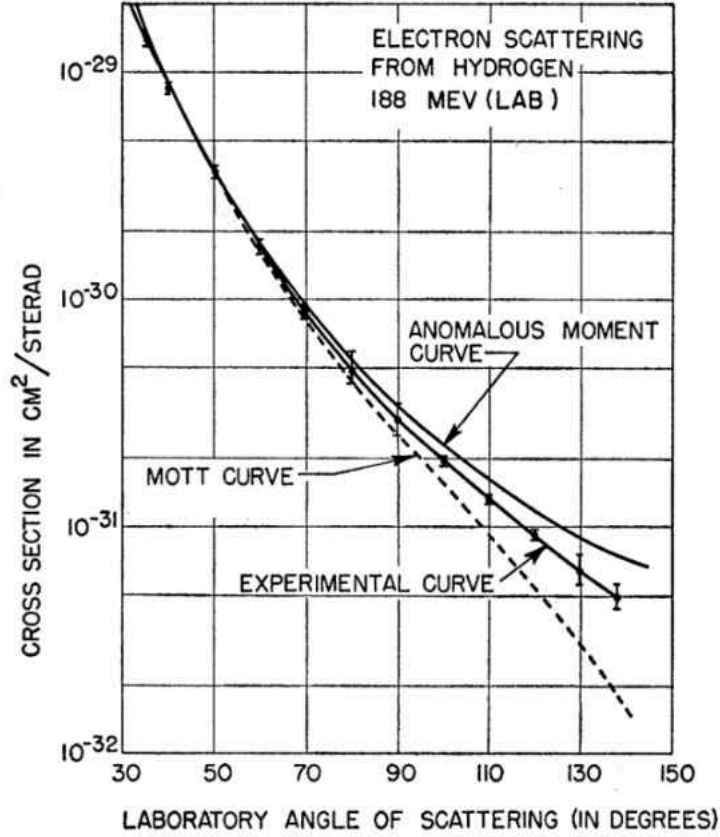
FIG. 2: First elastic electron-proton scattering experiment at Stanford University [2].

is detected. The DIS process can be written as:

$$e(P_e) + p(P_p) \rightarrow e'(P_{e'}) + X(P_X) \tag{6}$$

where the quantities in the parentheses are the four-momentum vector of the particles and X are the unknown final state particles as shown in Fig. 3. The invariant mass of the proton and virtual photon is expressed as :

$$W^2 = (p+q)^2 = M^2 + 2M\nu - Q^2 \tag{7}$$

where p is the four-momentum of the proton, $q = P_e - P_{e'}$ is the four-momentum difference of the incident and scattered electron, and ν is the transferred energy to the proton by the virtual photon. If the final state particles are identical to the initial state particles, which is the elastic scattering process, $W^2 = M_p^2$. In practice, the DIS regime corresponds to $W^2 > 2$ GeV^2 and $Q^2 > 1$ GeV^2 where individual proton resonances cannot be seen. The wavelength

of the virtual photon is proportional to $1/\sqrt{Q^2}$. At large values of Q^2, the wavelength becomes smaller than the proton size and starts to probe the internal structure of it.
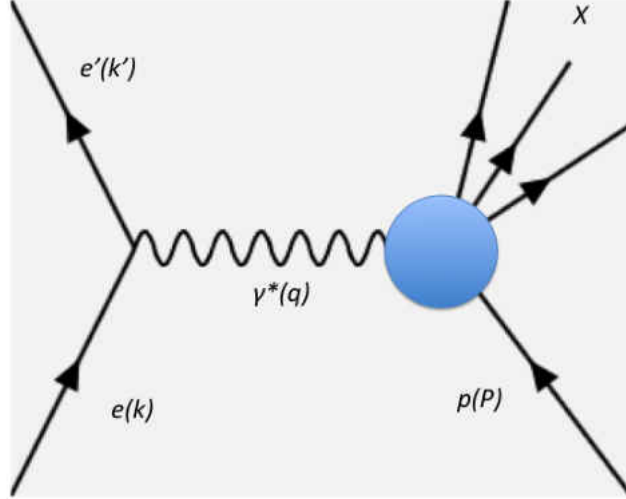
FIG. 3: Illustration of the inelastic electron-proton scattering.

One of the important results of DIS is that in elastic scattering processes, the cross-section was dependent on Q^2, which led to the conclusion that the proton has an internal structure. However, in DIS it is independent of Q^2, which shows that proton's constituent particles have no form factors or that they are point-like particles.

The cross-section of the DIS process was derived by Drell and Walecka [5] by parameterizing the unknown structure of the proton into two structure functions as following:

$$\left(\frac{d^2\sigma}{dE'd\Omega}\right)_{ep \to e'X} = \frac{\alpha^2}{4 \cdot E^2 \cdot \sin^4(\frac{\theta}{4})}\left(W_2(\nu, Q^2) \cdot \cos^2(\frac{\theta}{2}) + 2 \cdot W_1(\nu, Q^2) \cdot \sin^2(\frac{\theta}{2})\right) \quad (8)$$

where W_1 and W_2 are structure functions depending on ν and Q^2. These structure functions can be obtained by experiments. Bjorken proposed to study these structure functions in the energy region where $Q^2 \to \infty$ and $\nu \to \infty$. He used a new dimensionless variable $x_B = \frac{Q^2}{2M\nu}$ which needs to be kept constant. M is the mass of the nucleon. This region also called Bjorken regime.

The structure functions W_1 and W_2 can be written in terms of the Parton Distribution Functions (PDFs) in the Bjorken regime as following:

$$W_1(\nu, Q^2) = \frac{1}{M}F_1(x, Q^2) \quad (9)$$

$$W_2(\nu, Q^2) = \frac{1}{\nu} F_2(x, Q^2) \tag{10}$$

where x is the fraction of the nucleon's momentum carried by struck quark. The relation between $F_2(x, Q^2)$ of the proton and Q^2 is shown in Fig. 4 at fixed values of x. It can be seen that there is almost no dependence of $F_2(x, Q^2)$ on Q^2 when $x \approx 0.08$. The deviations at low x values are due to the increased probability of quark-antiquark interactions.
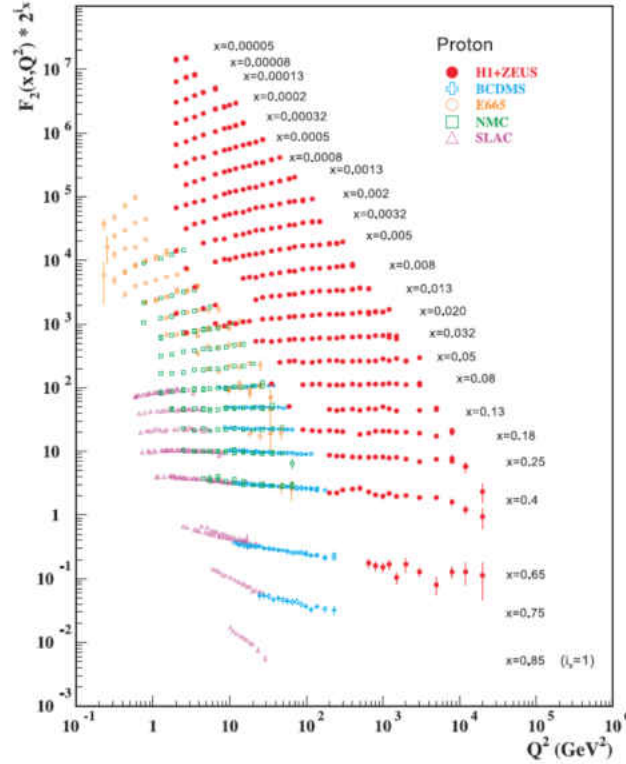
FIG. 4: The parton structure function F_2 measured using electron-proton scattering processes [6].

The connection between these two momentum independent structure functions is given by the Callan-Gross relation by assuming that the partons are spin-$\frac{1}{2}$ particles as following:

$$F_2(x) = 2xF_1(x) \tag{11}$$

Experiments confirmed this relation which supports that partons have similar properties as quarks.

In the frame where the proton is moving with infinite momentum, these structure functions are related to the probability densities of the quarks as following:

$$F_1(x) = \frac{1}{2} \sum_i e_i^2 q_i(x) \tag{12}$$

$$F_2(x) = x \sum_i e_i^2 q_i(x) \tag{13}$$

where e_i is the charge of the quark with flavor i, $q_i(x)$ is the probability density for finding a quark with flavor i and x is the fraction of the proton's momentum carried by the struck quark. In the naive quark model, it is stated that proton is composed of two up and one down valence quarks. In Fig. 5, the PDFs of partons with different flavors versus x at a fixed Q^2 are shown. It can be seen that around $x = 1/3$, the contribution of the up quark is twice that of the down quark in agreement with the quark model. At low x values, a large contribution from other sea quarks and gluons are seen. The Parton Distribution Functions (PDFs) from DIS processes are fundamental information to understand the internal structure of the nucleons. However, they are not enough to describe the structure.
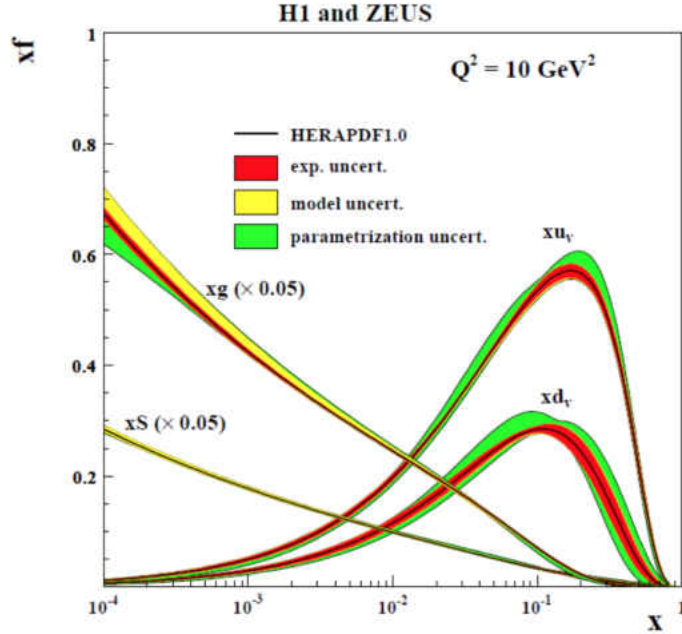
FIG. 5: Unpolarized parton distribution functions [6].

2.3 DEEP EXCLUSIVE SCATTERING

In the DIS process, it is possible to obtain longitudinal momentum distributions of the partons inside the nucleon which has infinite momentum. However, it is not possible to get any information about the spatial distributions perpendicular to the nucleon motion in DIS processes. Recent developments in both the theoretical and experimental area showed that deep exclusive scattering (DES) can provide more complete information about nucleon structure which is encoded in so-called Generalized Parton Distributions (GPDs) [7, 8, 9]. The

GPDs can provide simultaneous multidimensional information about the internal structure of the nucleon.

One of the important properties of the hard scattering processes (DIS and DES) is factorization. In other words, it is possible to separate the reactions into two parts, hard (perturbative) and soft (non-perturbative) parts. This feature of the hard processes makes it possible to study GPDs in Deeply Virtual Compton Scattering (DVCS) [10] and Deeply Virtual Meson Production (DVMP) [11] in the limit $Q^2 \to \infty$ at a fixed t and x_B. The amplitude of the hard part of the exclusive processes can be calculated using perturbative methods while the amplitude of soft part (lower blob) is non-perturbative and can be parameterized in terms of GPDs as shown in Fig. 6.
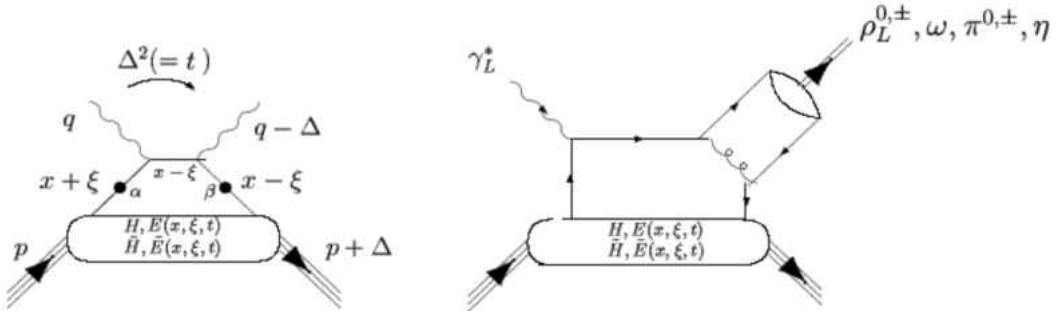
FIG. 6: Illustration of the deep exclusive processes. The figure on the left (right) is the handbag diagram for DVCS (DVMP).

2.3.1 GENERALIZED PARTON DISTRIBUTIONS (GPDS)

There are eight GPDs for a quark with flavor q. Four of them correspond to a parton helicity-conserving (chiral-even) process and are denoted by $H^q(x, \xi, t)$, $\tilde{H}^q(x, \xi, t)$, $E^q(x, \xi, t)$ and $\tilde{E}^q(x, \xi, t)$. The other four correspond to a parton helicity-flip (chirol-odd) process and are denoted by $H_T^q(x, \xi, t)$, $\tilde{H}_T^q(x, \xi, t)$, $E_T^q(x, \xi, t)$ and $\tilde{E}_T^q(x, \xi, t)$ [12, 13]. In the light-cone frame where the virtual photon and nucleon are traveling at the speed of light in the opposite direction to each other, these GPDs correspond to the amplitude where the quark with the momentum fraction $x + \xi$ is taken out and put back with momentum fraction $x - \xi$ as shown in Fig. 6. They depend on three kinematic variables: x, ξ and t. $t = (p - p')^2$ is the four-momentum transfer to the nucleon squared. p and p' are the initial and final four-momentum of the nucleon. x is the average longitudinal momentum fraction held by the struck parton and ξ (skewness) is half of the longitudinal momentum fraction transferred to the parton.

In the Bjorken limit, the skewness is defined as:

$$\xi = \frac{x_B}{2 - x_B}.$$

(14)

The chiral-even GPDs, H and $\tilde{H}$, are spin-independent functions which conserve the spin of the nucleon while E and $\tilde{E}$ are spin-dependent functions which flip the spin of the nucleon. The H and E GPDs are called unpolarized since they correspond to the sum over parton helicities and $\tilde{H}$ and $\tilde{E}$ are correspond to the difference of the parton helicities and called polarized GPDs, respectively. In the light-cone frame, the range of the variables x and ξ is between -1 and 1, thus there are three cases: $x > \xi$, $-\xi < x < \xi$ and $x < -\xi$. When both momentum fractions, $x + \xi > 0$ and $x - \xi > 0$, are positive, the virtual photon interacts with quarks. If the momentum fractions are negative, anti-quarks are involved in the interaction process. In the third case, where $|x| < \xi$, a quark is taken out and an anti-quark is put back or vice-versa.

In the forward limit, where $t \to 0$, the helicity conserving GPDs, H and $\tilde{H}$, reduce to the parton distribution functions (PDFs) obtained from DIS process:

$$H^f(x, 0, 0) = \begin{cases} q^f(x), & x > 0 \\ -\bar{q}^f(-x), & x < 0 \end{cases}$$

(15)

$$\tilde{H}^f(x, 0, 0) = \begin{cases} \Delta q^f(x), & x > 0 \\ -\Delta \bar{q}^f(-x), & x < 0 \end{cases}$$

(16)

where $q^f(x)$ and $\bar{q}^f(x)$ are quark and anti-quark density distributions and $\Delta q^f(x)$ and $\Delta \bar{q}^f(x)$ quark and anti-quark helicity distributions with flavor f, respectively. In addition, at finite momentum transfer, the relation of the the first moments of chiral-even GPDs to the elastic form factors of the nucleon via model independent sum rules is as following:

$$\int_{-1}^{1} dx H^f(x, \xi, t) = F_1^f(t)$$

(17)

$$\int_{-1}^{1} dx E^f(x, \xi, t) = F_2^f(t)$$

(18)

$$\int_{-1}^{1} dx \tilde{H}^f(x, \xi, t) = g_A^f(t)$$

(19)

$$\int_{-1}^{1} dx \tilde{E}^f(x, \xi, t) = h_A^f(t)$$

(20)

where $F_1^f(t)$ and $F_2^f(t)$ are the elastic Dirac and Pauli form factors of the quark with flavor f, respectively. Similarly, $g_A^f(t)$ is the axial form factor and $h_A^f(t)$ is the pseudo-scalar form factor [14].

Another property of the GPDs is the polynomiality which is the relation between x-moments of the GPDs and ξ. The x^n moment of the unpolarized GPDs, H and E, are a polynomial in even powers of ξ with maximum power $n+1$ [8].

$$\int_{-1}^{1} x^n H^f(x,\xi,t)dx = \sum_{i=0}^{\frac{n-1}{2}}(2\xi)^{2i} A_{n+1,2i}^f(t) + Mod(n,2)(2\xi)^{n+1}C_{n+1}^f(t) \tag{21}$$

$$\int_{-1}^{1} x^n E^f(x,\xi,t)dx = \sum_{i=0}^{\frac{n-1}{2}}(2\xi)^{2i} B_{n+1,2i}^f(t) - Mod(n,2)(2\xi)^{n+1}C_{n+1}^f(t) \tag{22}$$

Similarly, for polarized GPDs, the maximum power is n.

$$\int_{-1}^{1} x^n \tilde{H}^f(x,\xi,t)dx = \sum_{i=0}^{\frac{n-1}{2}}(2\xi)^{2i} \tilde{A}_{n+1,2i}^f(t) \tag{23}$$

$$\int_{-1}^{1} x^n \tilde{E}^f(x,\xi,t)dx = \sum_{i=0}^{\frac{n-1}{2}}(2\xi)^{2i} \tilde{B}_{n+1,2i}^f(t) \tag{24}$$

where $Mod(n,2)$ is equal to 0 (1) for n even (odd). The integrals of the first moment GPDs results in form factors as in the Eqns. (17), (18), (19) and (20). The sum of the second moments of the unpolarized GPDs, $H + E$, gives the angular momentum sum rule of X. Ji [8]:

$$J^f = \frac{1}{2} \int_{-1}^{1} x[H^f(x,\xi,t \to 0) + E^f(x.\xi,t \to 0)]dx \tag{25}$$

where J^f is the total angular momentum of the quark with flavor f and it is independent of ξ. The angular momentum carried by the quarks is decomposed as :

$$J^f = \frac{1}{2}\Delta\Sigma + L^f \tag{26}$$

where L^f is the orbital angular momentum of the quark and $\frac{1}{2}\Delta\Sigma$ is the contribution from the spin of the quarks to the nucleon spin.

2.3.2 DEEPLY VIRTUAL MESON PRODUCTION

Exclusive electroproduction processes (DVCS and DVMP) offer a unique opportunity to study the nucleon structure at the parton level, described by GPDs. The description of these

processes in terms of GPDs rests on factorization which is proven when the virtual photon is longitudinally polarized as mentioned in section 2.3. However, factorization for transverse photons is assumed to be applicable. In the DMVP process, it has been shown that the vector mesons are sensitive to the polarized chiral-even GPDs and pseudo-scalar ones are sensitive to the unpolarized GPDs. However, unlike DVMP, the DVCS process depends on both polarized and unpolarized GPDs. In addition, DVCS is at leading order sensitive to the chiral-even GPDs. However, chiral-odd GPDs are needed to describe the complete nucleon structure in addition to chiral-even GPDs. Pseudo-scalar π^0 electroproduction was identified as especially sensitive to the chiral-odd GPDs [15, 16, 17]. Moreover, the pion production amplitudes suppresses helicity-conversing amplitudes relative to the helicity-flip ones [16].
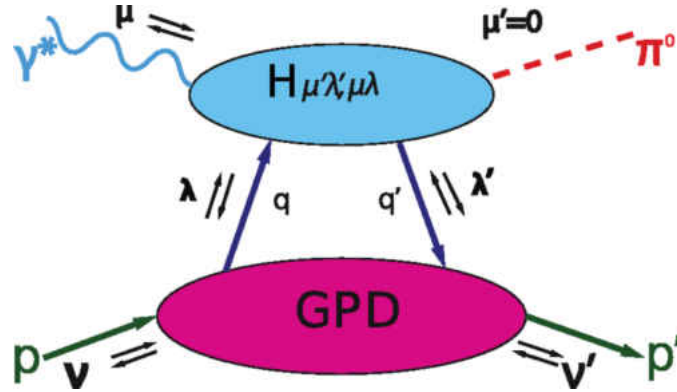
FIG. 7: Neutral pion electroproduction in the framework of the handbag diagram. $\nu(\nu')$ represents the initial (final) nucleon helicities. The helicity of the virtual photon is represented by μ and produced meson's helicity is represented by μ'. Initial and final helicities of the active quark is λ and λ'. The arrows shows the positive and negative helicities [18].

In Fig. 7, the handbag diagram of the reaction $\gamma^*p \rightarrow p'\pi^0$ is shown. The chiral-odd GPDs related to the amplitude of the process where incoming virtual photon with helicity $\mu = \pm1, 0$ takes out and interacts with a single parton with momentum fraction $x + \xi/2$ and helicity $\lambda = \pm1/2$ to produce a meson. Then, the parton is put back with momentum fraction $x - \xi/2$ and helicity $\lambda' = -\lambda$. The GPDs contributing in pseudo-scalar meson production for a transverse photon is H_T and $\bar{E}_T = 2\tilde{H}_T + E_T$. The first one corresponds to nucleon helicity flip and becomes the transversity function, $H_T(x, 0, 0) = h_1(x)$, in the forward limit. The latter GPDs corresponds to the nucleon helicity conserving case.

Regge-type model also describe the pion production processes. It is based on the exchange of Regge trajectories in the t-channel. This model has been studied for meson photoproduction where $Q^2 = 0$ and photons are transversely polarized. In addition, it has been also used to describe vector meson production and charged pion production. The Regge model had

been successfully applied to π^0 electroproduction at DESY [21, 22].

Kinematics and Definitions
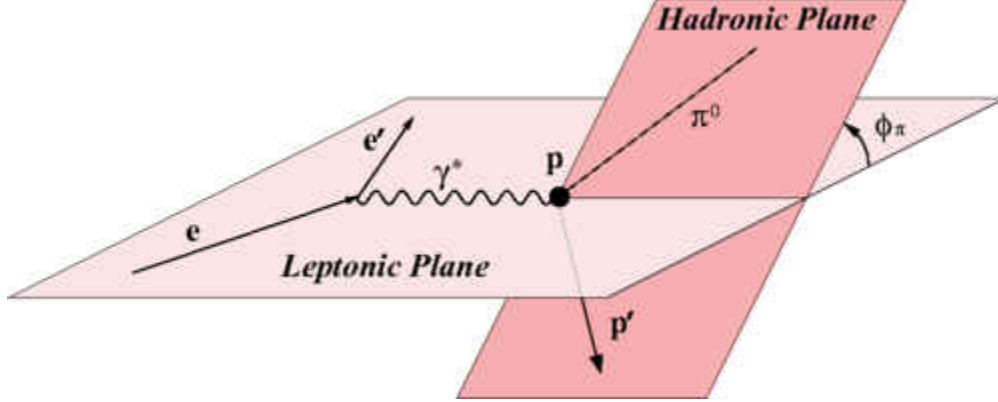
FIG. 8: The electroproduction of neutral pion on a proton. The figure is taken from Ref. [19].

In the deeply virtual meson electroproduction process, the incident electron scatters off a target and the virtual photon interacts with one of the partons inside the nucleon as illustrated in Fig. 8.

$$e(P_e) + p(P_p) \rightarrow e'(P_{e'}) + p'(P_{p'}) + p_\pi(P_\pi) \tag{27}$$

The four-momentum of the incident electron is $P_e = (E, \vec{k})$ and four-momentum of the scattered electron is $P'_e = (E', \vec{k'})$. $q = (\nu, \vec{q})$ is the four-momentum vector of the virtual photon. The initial (final) target four-momentum is defined as $P_p(M_p, 0)$ $(P'_p(E'_p, \vec{p'_p}))$. The four-momentum of the produced meson with mass M is $P'_M(E'_M, \vec{p'_M})$. The kinematic variable of the DIS region can be defined from the final state particle's four-momentum vectors as following:

$$Q^2 = -q^2 = 4E_e E'_e \sin^2(\frac{\theta}{2}) \tag{28}$$

$$W^2 = (P + q)^2 = M_p^2 + 2M_p\nu - Q^2 \tag{29}$$

where θ is the scattered polar angle of the electron in the lab frame and $\nu = E_e - E'_e$ is the energy transfer of the electron to the target. In the DIS region, the kinematics are restricted to $Q^2 > 1$ GeV^2 in order to ensure that perturbative QCD can be applicable and $W^2 > 2$ GeV^2 to exclude the baryon resonance region.

The differential cross-section for exclusive neutral pion electroproduction off an unpolarized target and with an unpolarized electron beam is given as [23]:

$$\frac{d^2\sigma}{d\Omega dE' d\phi dt} = \Gamma\{\frac{d\sigma_{TT}}{dt} + \epsilon_L \frac{d\sigma_L}{dt} + \epsilon\cos(2\phi)\frac{d\sigma_{TT}}{dt} + \sqrt{2\epsilon_L(\epsilon+1)}\cos(\phi)\frac{d\sigma_{LT}}{dt}\} \tag{30}$$

where ϕ is the azimuthal angle between the leptonic plane and the hadronic production plane (see Fig. 8)and ϵ is the polarization parameter of the virtual photon. If the beam is longitudinally polarized with helicity $h = \pm 1$, there is one additional term to the cross-section in Eqn. (30)

$$h\sqrt{2\epsilon_L(1-\epsilon)}\sigma_{LT'}\sin(\phi) \tag{31}$$

where the variables σ_T, σ_L, σ_{TT}, σ_{LT} and $\sigma_{LT'}$ in Eqns. (30) and (31) are structure functions depending on Q^2, x_B and t.

The virtual photon polarization parameter, ϵ, can be written as:

$$\epsilon^{-1} = 1 + 2(1 + \frac{\nu^2}{Q^2})(4\frac{\nu^2}{Q^2}\frac{1-y}{y} - 1)^{-1} \tag{32}$$

where the dimensionless parameter $y = \nu/E$ is the fraction of the electron energy transferred to the target. The longitudinal component of the photon polarization is :

$$\epsilon_L = \frac{Q^2}{\nu^2}\epsilon \tag{33}$$

The Γ factor in Eqn. (30) is given by

$$\Gamma = \sigma_{Mott} f_{rec} M_\pi |\vec{p_\pi}| J(Q^2, \nu, s) \tag{34}$$

where M_π and $\vec{p_\pi}$ is the mass and momentum of the produced pion, respectively. $J(Q^2, \nu, s)$ is the Jacobian for transformation from $\cos(\theta_\pi^{LAB})$ to t. f_{rec} is the hadronic recoil factor and defined as:

$$f_{rec} = |1 + \frac{\nu - |\vec{q}|\cos(\theta_\pi^{LAB})}{M_p}|^{-1} \tag{35}$$

The structure functions in Eqns. (30) and (31) can be decomposed in terms of the helicity amplitudes chosen as $f_1 = f_{1+,0+}$, $f_2 = f_{1+,0-}$, , $f_3 = f_{1-,0+}$, $f_4 = f_{1-,0-}$, $f_5 = f_{0+,0-}$ and $f_6 = f_{0+,0+}$. The first four of the helicity amplitudes correspond to the transverse photons and last two of them correspond to the longitudinally photons. We use the notation: $f_{\Lambda_\gamma \Lambda_{N'}, 0\Lambda_{N'}}$ where $\Lambda_\gamma = \pm 1, 0$ is spin of the photon and $\Lambda_N(\Lambda_{N'}) = \pm \equiv \pm 1/2$ is spin of the initial (final) state. With these definitions, we have:

$$\frac{d\sigma_T}{dt} = N(|f_1|^2 + |f_2|^2 + |f_3|^2 + |f_4|^2) \tag{36}$$

$$\frac{d\sigma_L}{dt} = N(|f_5|^2 + |f_6|^2) \tag{37}$$

$$\frac{d\sigma_{TT}}{dt} = 2N\Re e(f_1^* f_4 - f_2^* f_3) \tag{38}$$

The interference terms for the transversely and longitudinally polarized virtual photon is

$$\frac{d\sigma_{LT}}{dt} = 2N\Re e(f_5^*(f_2 + f_3) + f_6^*(f_1 - f_4)) \tag{39}$$

$$\frac{d\sigma_{LT'}}{dt} = 2N\Im m(f_5^*(f_2 + f_3) + f_6^*(f_1 - f_4)) \tag{40}$$

where $N = [M_p(s - M_p^2)^2]^{-1}G$. $G = \pi/2$ and $G = 1/8\pi$ is the geometrical factor in Regge and GPD approaches.

The beam-spin asymmetry is defined as:

$$A_{LU} = \frac{d\sigma^+ - d\sigma^-}{d\sigma^+ + d\sigma^-} = \frac{\alpha \sin(\phi)}{1 + \beta \cos(\phi) + \gamma \cos(2\phi)} \tag{41}$$

where the $\pm$ signs as superscript of the cross-section indicate the longitudinal beam helicity and parameters α, β and γ are

$$\alpha = \frac{\sqrt{2\epsilon_L(1 - \epsilon)}\frac{d\sigma_{LT'}}{dt}}{\frac{d\sigma_T}{dt} + \epsilon_L \frac{d\sigma_L}{dt}} \tag{42}$$

$$\beta = \frac{\sqrt{2\epsilon(1 + \epsilon)}\frac{d\sigma_{LT}}{dt}}{\frac{d\sigma_T}{dt} + \epsilon_L \frac{d\sigma_L}{dt}} \tag{43}$$

$$\gamma = \frac{\epsilon \frac{d\sigma_{LT'}}{dt}}{\frac{d\sigma_T}{dt} + \epsilon_L \frac{d\sigma_L}{dt}} \tag{44}$$

The polarization of the virtual photon produces the ϕ azimuthal angle dependence of the BSA (see Eqn. 41). The relation between observables and helicity amplitudes are independent of any particular model [24].

Previous Measurements of beam-spin asymmetry on hydrogen target

The azimuthal dependence of beam-spin asymmetries have been measured for exclusive neutral pion electroproduction off the proton above the resonance region for the first time [25] by the CLAS collaboration. In this measurement, CEBAFs 5.77 GeV longitudinally polarized electron beam was scattered off a 2.5 cm long liquid-hydrogen target. The beam polarization, measured by a Moller polarimeter, was 79.4%. All final-state particles were detected. The measured asymmetry amplitudes α (Eqn. 41) are systematically of the order of 0.04 to 0.11 over a wide range in Q^2, x_B and t kinematic variables as shown in Fig. 9. These non-zero asymmetries are a clear sign of a non-zero $\frac{d\sigma_{LT'}}{dt}$ which means both longitudinal and transverse amplitudes participate in the $\gamma^* p \to p' \pi^0$ process.
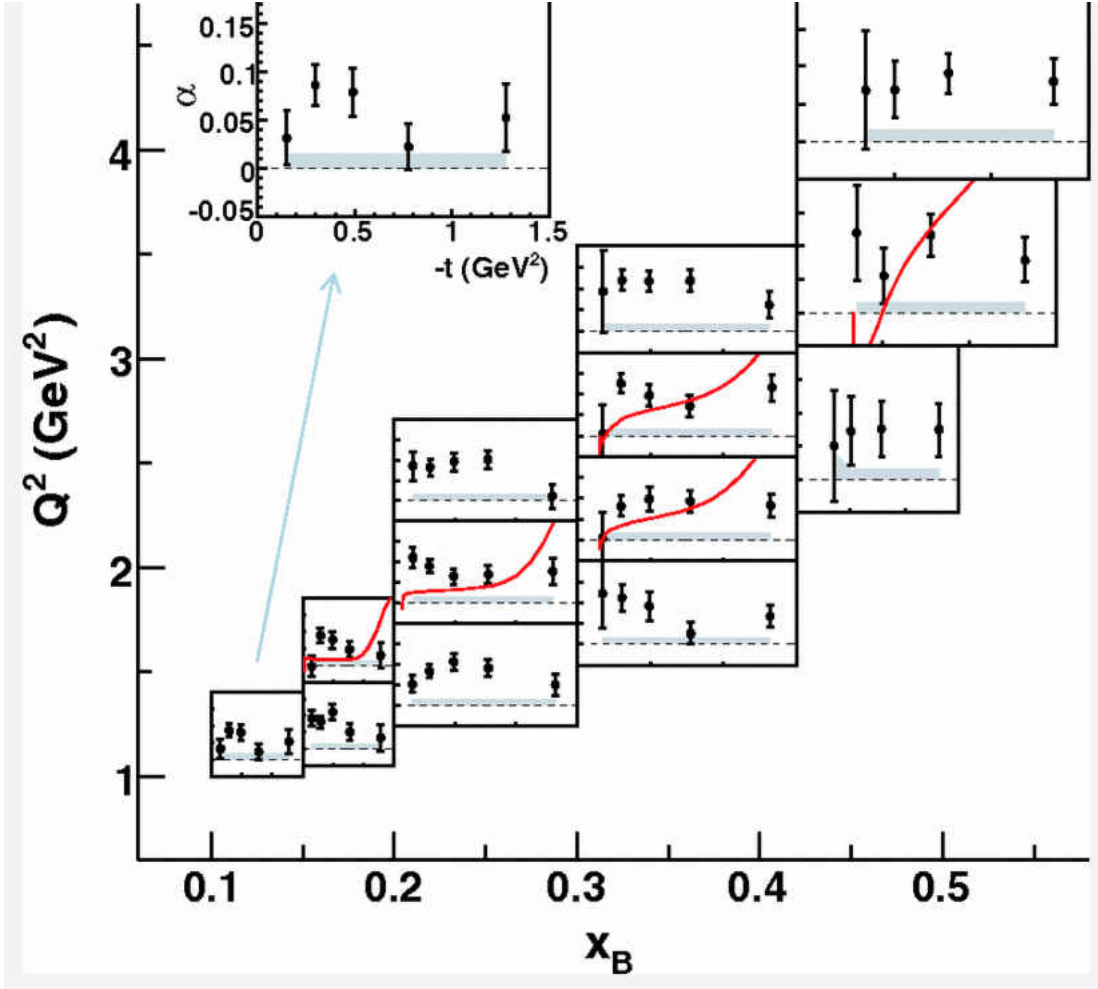
FIG. 9: The extracted beam-spin asymmetries for different bins in Q^2 and x_B as a function of -t. The red curves correspond to the Jean-Marc Laget [25] model and grey areas correspond to the systematic uncertainties.

Nuclear DVMP

In nuclear targets, it is possible to measure beam-spin asymmetry in neutral pion electro-production in two processes, coherent and incoherent. In the incoherent process, the nucleus breaks up and makes it possible to measure BSA on a bound nucleon. However, in the coherent process, the recoil nucleus remain intact after the meson production. In this work, we will investigate only the coherent process.

The number of chiral-even GPDs in the parametrization of the structure functions via DMVP is equal to $(2s + 1)^2$ where s is the spin of the target. For instance, the number of GPDs is equal to four for proton ($s = 1/2$) and nine for deuteron ($s = 1$) target. However,

there is only one chiral-even GPD for helium-4 targets since it is spinless. In addition, the spin of the helium-4 before and after scattering is the same which results will simplify the description of the interference term of the cross-section in Eqn. (40) in terms of helicity amplitudes. These features of the helium-4 target makes it an important target to study the electroproduction processes.

CHAPTER 3

EXPERIMENTAL SETUP

3.1 OVERVIEW
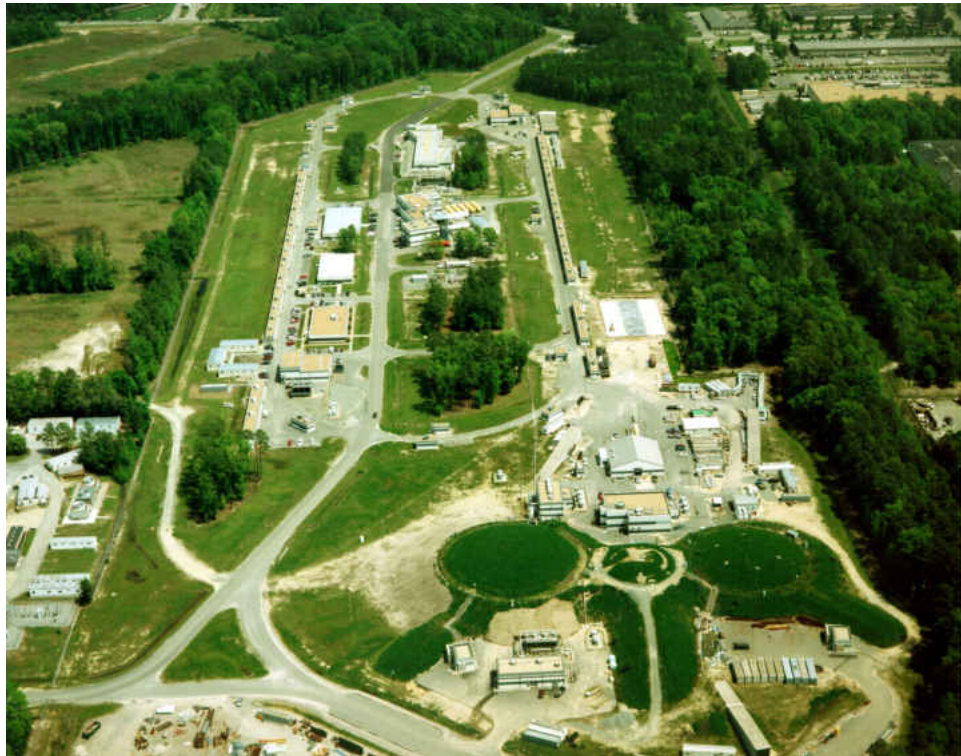
FIG. 10: Experimental site of Jefferson National Labaratory.

In this chapter, the experimental setup which was used to collect data for the EG6 experiment will be described. The experiment was conducted at the Thomas Jefferson National Accelerator Facility (Jefferson Lab) in Newport News, Virginia, over the period of three months in the Fall of 2009. This laboratory is home to an electron accelerator called Continuous Electron Beam Accelerator Facility (CEBAF) and three experimental halls (A, B, and C). CEBAF has the capability to supply a continuous electron beam of up to 6 GeV energy to all three experimental halls, simultaneously. There is more information about the accelerator in the next section below. In this experiment, 6 GeV electrons were incident

on a ^{4}He gas target at rest in Hall B. This experimental hall houses the CEBAF Large Acceptance Spectrometer (CLAS) detector package which features almost a 4π acceptance. It is used to identify and reconstruct the momentum and energies of final state particles. In addition to the CLAS detector package, an inner calorimeter (IC) was used to detect low angle scattered particles, and a Radial Time Projection Chamber (RTPC), to detect low momentum α particles. Finally, I will provide information about data acquisition system of Hall B and the 20 cm long Kapton tube target, filled with ^{4}He gas at 6 atmospheres pressure.

3.2 CEBAF

The Continuous Electron Beam Accelerator Facility (CEBAF) provides an (almost) continuous beam of electrons [26]. The schematic overview of CEBAF is shown in the Fig. 11. It is 30 feet below the surface and has two linear accelerators (Linacs) connected through nine recirculation arcs. The radii of the arcs are large enough that when electrons pass through them, the energy loss due to radiation is negligible. In CEBAF, electrons are produced at the injector and accelerated up to 6 GeV in the Linacs. Then, the beam is sent into the different experimental halls. The accelerator has the capability to produce electron beam pulses separated by 2 ns with a polarization of up to $\approx 88\%$. The duty factor of the beam produced by CEBAF is $\approx 100\%$.
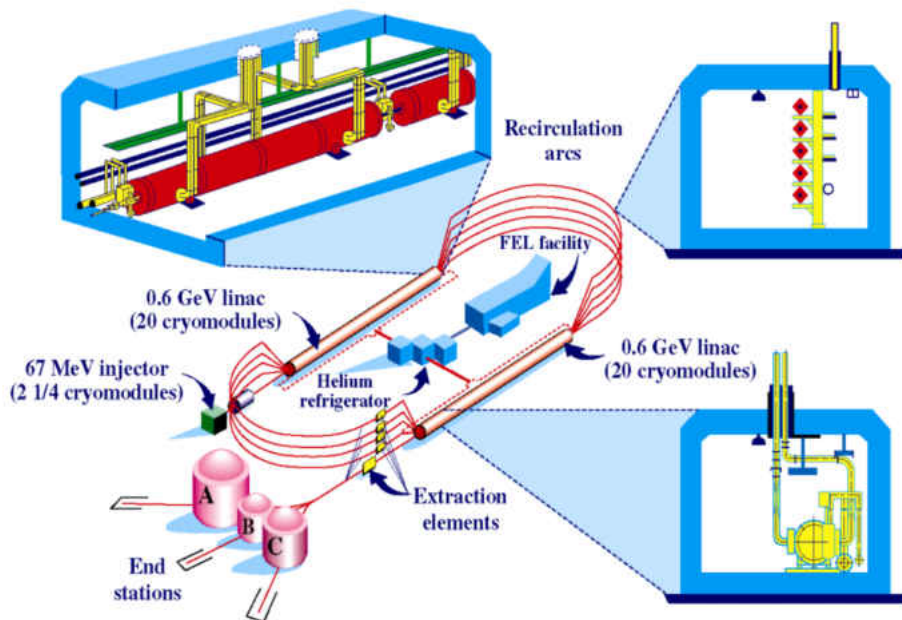
FIG. 11: Shematic diagram of CEBAF.

The injector has two electron guns and three lasers. Each laser produces electrons at a frequency of 499 MHz shifted in phase such that each experimental hall can have electron beams with different energies and currents independently and simultaneously. This is a very important requirement because Hall B operates at a few nA while other halls can run in the μA range.The beam starts in the injector by knocking off electrons from a photocathode (GaAs) by these lasers. These electrons initially gain energy of about 100 kV as a result of potential difference between anode and cathode. Next, the electrons are accelerated at two 5-cell superconducting radio frequency (SRF) niobium cavities and then, two 8-cell SRF cryomodules up to 67 MeV. Then, these electrons have the required energy to be sent into the North Linac.
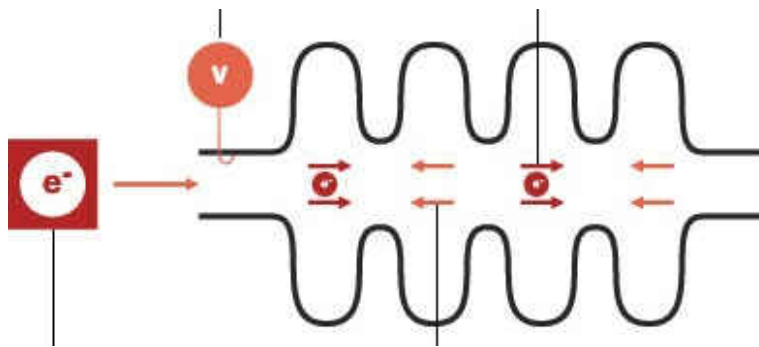
FIG. 12: Accelerating cavity.

The North Linac consists of 20 cryomodules. Each cryomodule has eight 5-cell niobium cavities as illustrated in Fig. 12. These niobium cavities are contained in a liquid helium bath to keep temperatures at about 2 K. At this temperature, the cavities become super-conducting which means electromagnetic waves can travel inside cavities with no resistance. The electrons are given a series of boosts in the cavities at a frequency of 1497 MHz of the electric field for acceleration. At the end of the North Linac, electrons have passed through 20 cryomodules, gained energy of 600 MeV and reached a region called spreader. In the spreader, the electrons are separated vertically according to their momentum by dipole magnets and directed to the different East Recirculation arcs. The highest energy electrons go to the lowest level arc9 while the lowest energy electrons go to the highest level arc1.In the East arcs, the beam is turned 180^0 degrees by a series of dipole magnets, recombined at the end of arc and directed into the South Linac. In the South Linac, which is identical to North Linac, the beam also gains 600 MeV and reaches the West Spreader. It is separated again according to its energy, bent 180^0 in the West arcs and recombined again just before it goes into North Linac. At the end of this one full pass, the beam gains 1200 MeV energy.

After five successive full-passes the electron beam has reached an energy of up to 6.067 GeV. Finally, it is separated and distributed to the three experimental halls.

3.3 CLAS DETECTOR PACKAGE

The CEBAF Large Acceptance Spectrometry (CLAS) was built to study multi-particle final state reactions. As one can see in Fig. 13, CLAS has a roughly spherical shape in order to have a large acceptance. Its acceptance is almost 4π. Its design is based on a torus magnet, which is used to bend charged particles in order to measure their momenta, divides the spectrometer into six independent sectors. Each sector consists of multi-layered detectors:

- Drift Chambers consist of three regions. They are used to provide tracking information for the trajectory and momentum reconstruction of charged particles.

- Cherenkov light detectors are used to differentiate between electrons and pions.

- Time Of Flight scintillators are used to measure the flight time from the interaction vertex.

- A Electromagnetic Calorimeter is used to detect showering particles and measure their energy.

Each of the subsystems of the CLAS detector package above will be described in detail in the following sections.

3.3.1 TORUS MAGNET

The torus magnet has six superconducting coils which are made of NbTi. Inside of these coils, liquid helium is circulated to cool the coils to 4.5 K and keep the temperature stable. The magnet can produce fields of up to 2 Tesla at the maximum current. The design of the coils are of a kidney shape arranged around the beam line as illustrated in Fig. 14, which produces a magnetic field in the azimuthal direction. The azimuthal magnetic field bends particles in polar angle and leave the azimuthal angle almost unchanged. The magnetic field, B, generated by the torus is used to deflect charged particles and measure their momentum. Relation between momentum, p, and curvature, r, of the particle is given in equation (45).

$$Br = \frac{p}{q} \tag{45}$$
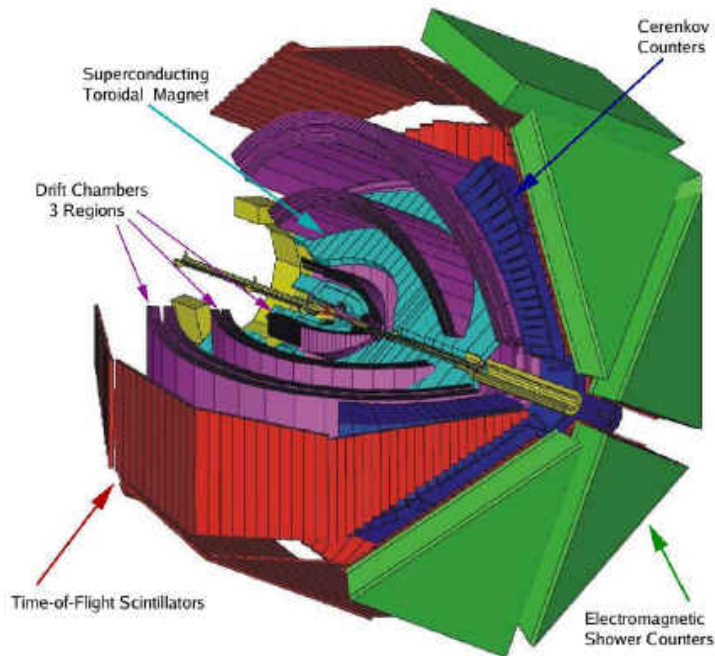
FIG. 13: CLAS Detector Package

where q is the charge of the particle. The radius of curvature is measured by fitting the trajectory of the particle.

3.3.2 DRIFT CHAMBERS

The purpose of the CLAS Drift Chambers [27] is to measure the trajectory and momentum of the charged particles. They are placed inside the toroidal magnet which bends charged particles towards or away from the beam line depending on the charge of the particle. The polar angular coverage of the drift chambers ranges from 8° to 142° and coverage of the azimuthal angle is 80%. The restrictions are due to the beam pipeline and toroidal coils, respectively. The momentum resolution for 1 GeV/c charged particles is $\delta p/p \leq 0.5\%$ and the angular resolution is $\delta\theta \leq 2$ mrad and $\delta\phi \leq 2$ mrad.

The CLAS drift chambers are separated into six sectors due to the magnet coils. In each sector, there are three sets of drift chambers organized radially, called Regions, as illustrated in the Fig 15 .

- Region 1 is the section of drift chambers closest to the target, where there is almost no
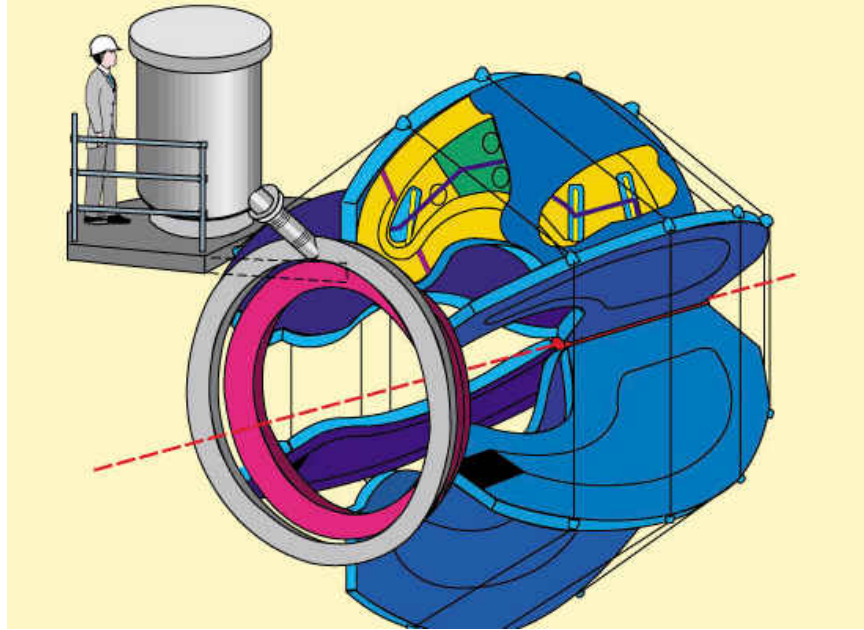
FIG. 14: The Design of the Torus Magnet.

magnetic field. Therefore, the direction of the charged particle is measured just after the reaction in this region.

- Region 2 is located between magnetic coils where the magnetic field is maximum.

- Region 3 is located outside of the magnetic coils. The direction of charged particle is measured before entering the downstream detectors.

All three regions combined provide the particle trajectory measurement used for the momentum and vertex reconstruction.

There are two superlayers of wires in each region of drift chambers. The wires in the first superlayer are axial or parallel to the field direction. The second superlayer wires are tilted at a 6° stereo angle with respect to axial ones which provides azimuthal information of the track. Six field wires surrounding one sense wire form a drift cell in a hexagonal pattern. The superlayers of Region 2 and Region 3 have six layers of these hexagonal cells while the superlayer on Region 1 has only four layers of cells due to space limitation. The high voltage difference between sense wire (positive potential) and field wires (negative potential) creates a drift region for ionization electrons produced by the charged particle when passing through the drift chamber gas. Gas amplification through an electron avalanche is obtained close to
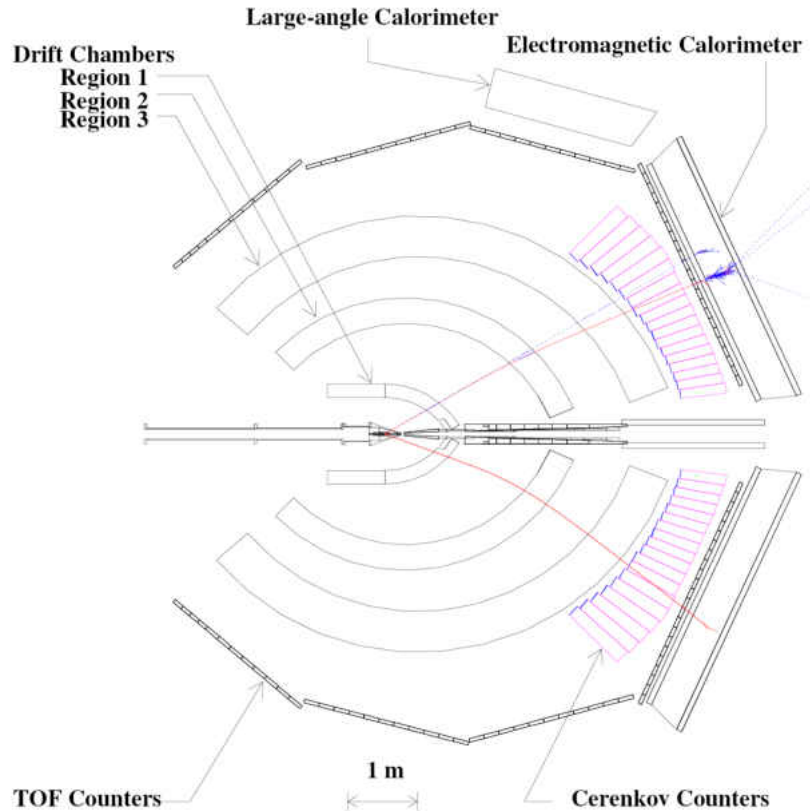
FIG. 15: The side view of the CLAS Detector.

the sense wire where this electric field is highest. As can be seen in Fig. 16, the drift cells are fired along the track of the charged particle when it passes through these cells. In this pattern of wires, the relation between drift time and drift distance is largely independent of the angle of the particle entering the cell since this shape is very close to a circle. In addition, the hexagonal configuration of these wires also decreases the electrostatic force between the sense and field wires which reduces tensions of the wires, which results in thinner endplates for chamber support. Thin endplates help to improve the geometrical acceptance of the spectrometer since they do not project out of the shadow of the torus.

The volume of each part of the drift chambers is filled with a gas mixture of 90% of argon and 10% of CO_2 which reduces multiple scattering. Moreover, this mixture of gas has high gain, high drift velocity (>4 cm/μs) and also has operating voltage range of several hundred volts before breakdown.
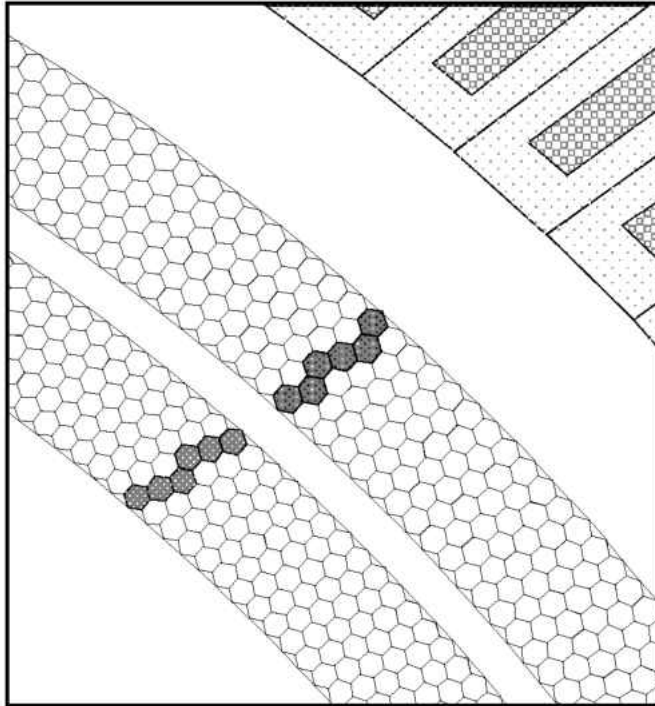
FIG. 16: The shape of two superlayers of Region 3. The highlighted pattern shows the path of a charged particle.

3.3.3 CHERENKOV DETECTORS

When the velocity of a fast particle is larger than the speed of light in the medium, that is c/n, where $n > 1$ is the refractive index of the gas, it produces Cherenkov light in the forward direction. This light is focused onto photomultiplier tubes by mirrors. In Fig. 17, the track of an electron passing through the CLAS Cherenkov detector [28] is shown. In electron scattering experiments, Cherenkov counters are used to distinguish pions from electrons. If pions and electrons have the same momentum, pions will be slower, since they have larger mass compared to electrons. Therefore, pions will not produce Cherenkov light below threshold. The threshold velocity of the particles to produce Cherenkov light will depend on the refractive index of the radiator gas inside detector. Perfluorobutane (C_4F_{10}) with a refractive index of $n = 1.00153$ is used as the radiator gas inside the Cherenkov detector. This gas provides a pion momentum threshold of 2.5 GeV/c and has very good transmission for short wavelength light.

The position of the Cherenkov counter is between Drift Chamber Region 3 and the Time
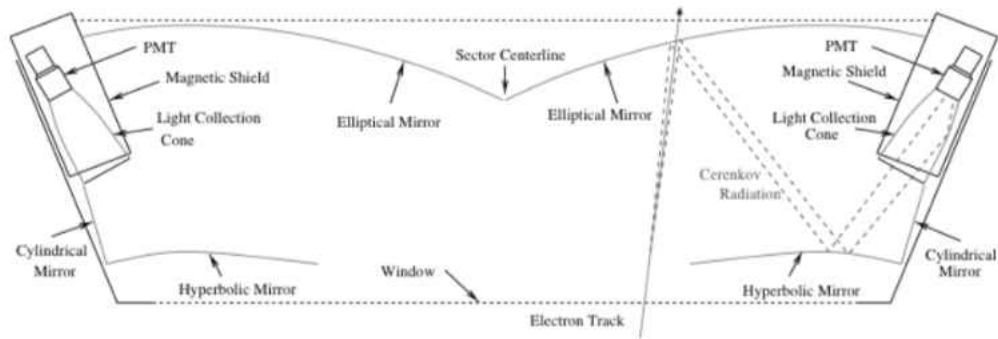
FIG. 17: Vertical cut of the one of the Cherenkov detector's segments. Cherenkov light from electrons is reflected by mirrors and guided by the Winston cones onto the photomultiplier.

Of Flight counter (see Fig 13). There are six sectors of the Cherenkov detector, each consisting of eight segments. In each segment, there are two focusing mirrors, Winston cones and photomultiplier tubes (PMT) as shown in Fig. 18. The polar angle coverage is $7° < \theta < 48°$ and the azimuthal angle coverage is almost complete.
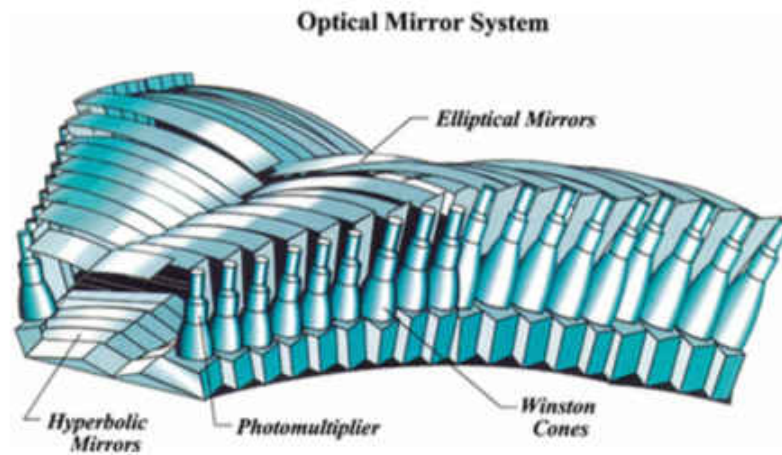
FIG. 18: Cherenkov optical modules of one sector.

3.3.4 TIME OF FLIGHT COUNTERS

The CLAS time of flight (TOF) counters [29] measure the time it takes a particle to reach it from the target. Using this information and the length of the path, it is possible to

calculate the velocity β of the particle. By combining this information with the momentum of the particle, given by the drift chambers, one can estimate the mass of the particle and identify it.
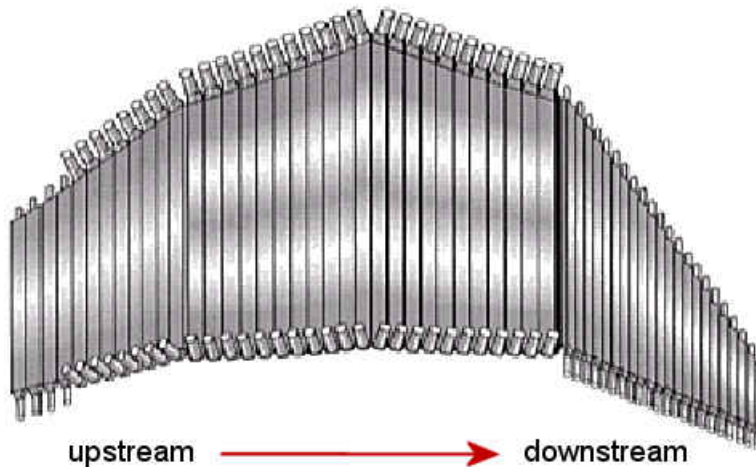
FIG. 19: Time Of Flight scintillators of one sector.

The location of the TOF is between Cherenkov counters and the calorimeter (see Fig. 13). There are six sectors, in each sector there are 57 scintillators bars. Each scintillator bar has two photomultiplier tubes at the ends, which produce the signal. The time difference from the light of the passing particle between these PMTs will allow the calculation of the position of particles. These scintillators are mounted in four panels. The first 23 scintillators are mounted in panel 1 and are referred to as forward-angle counters, which correspond to scattering angles less than 45°. The other scintillators are mounted in panel 2, 3 and 4, and these correspond to large-angle counters. They cover polar angles between 45° and 142°. In the Fig. 19, only one sector TOF is shown.

3.3.5 FORWARD CALORIMETER

The forward electromagnetic calorimeter [30] is the last layer of detectors in CLAS, located just after the TOF as shown in the Fig. 13. It has several functions: detection and triggering of electrons with energies greater than 0.5 GeV, detection of photons with threshold energy 0.2 GeV, reconstruction of π^0 and η from their 2γ decays, and also detection of neutrons. When charged or neutral particle pass through dense material, they will deposit their energy by producing electromagnetic showers or ionization. The amount of energy deposited as a function of the total momentum will give information about the particle. For

example, the electron is a showering particle and the energy deposited in the calorimeter is proportional to its total momentum, while the pion is a mimimum-ionizing particle and its energy deposition is independent of its energy. This information provides electron/pion separation. In addition, it is possible to identify neutrons in the EC by using the information of the particle from its time of flight.

(a)   (b)
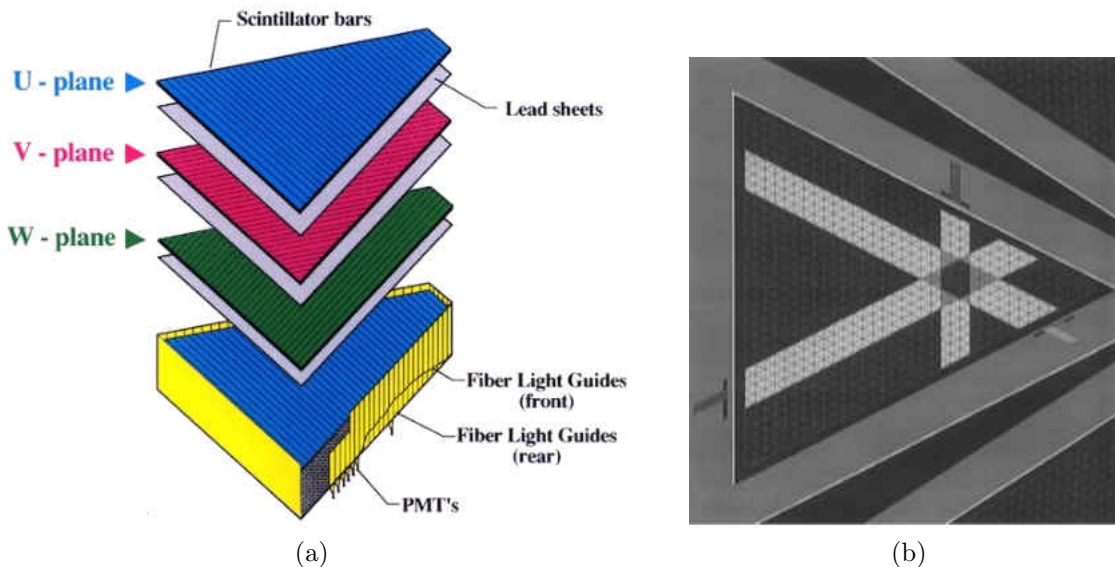
FIG. 20: (a) Electromagnetic calorimeter layers in one sector. (b) The view of the hit position on EC.

The EC has been divided into six independent sectors and the shape of each sectors looks like an equilateral triangle to match the hexagonal geometry of CLAS. In each sector of the EC, there are 39 layers of alternating plastic scintillators and thick layers of lead. Each scintillator layer consists of 36 scintillator bars, placed in parallel with respect to each other. These bars are rotated 120° in each successive layer. Each successive layer is labeled as U, V and W. This design has equilateral triangle cells, which gives position information of energy deposition as illustrated in Fig. 20.

3.4 INNER CALORIMETER

The CLAS forward electromagnetic calorimeter can not detect particles at small polar angles since the acceptance of CLAS decreases as the polar angle decreases. However, the detection of photons with small polar angle is important in exclusive photon or neutral pion production experiments. To overcome this problem, the inner calorimeter [31] was built and

tested in the e1-DVCS experiment. The performance of this detector was good in e1-DVCS experiment. The polar angular coverage of IC is about 4° to 15°. However, there will be extremely high number of Moller electrons at small angle that will hit IC. In order to shield IC from these electrons, a solenoid magnet with 4.5 T field was mounted around the target as illustrated in Fig. 21(b).

(a)   (b)
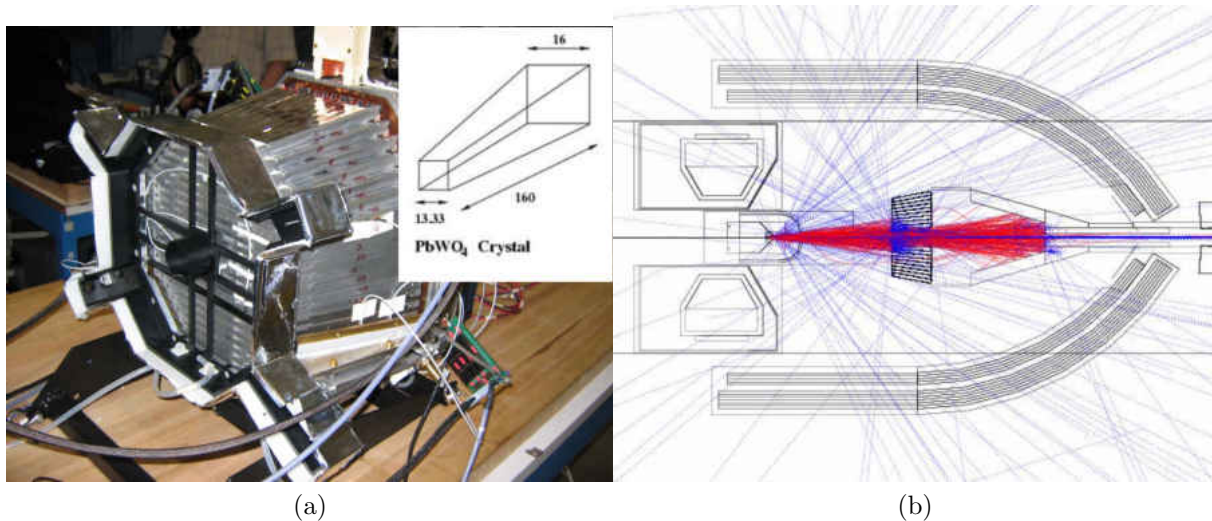
FIG. 21: (a) A picture of the Inner calorimeter. (b) Side view of the target, IC, solenoid magnet and first region of the DC produced by simulation. The red lines represent Moller electron paths. These electrons are focused by the magnetic field produced by the solenoid magnet to avoid them reaching the active region.

The inner calorimeter is made up of 424 $PbWO_4$ crystals and these crystals are arranged in an octagonal shape as shown in Fig. 21(b). The front cross-sectional area of each crystal is 13x13 mm^2 and the length is 160 mm. The beam passes through the hole in the center of IC. Avalanche Photo-Diodes (ADP), which are attached to the back of crystals, read out the light and pre-amplifiers amplify signals from the ADP. In order to have high precision energy measurements, the temperature of the IC is stabilized to vary less than 0.1 K. When a high energy photon or electron hits a crystal, it produces an electromagnetic shower and deposits its energy. If the deposited energy is bigger than the threshold energy, it is detected and labelled as hit energy. Reconstructed clusters, which are a set of hits, give information about position and energy of the particle.

3.5 RADIAL TIME PROJECTION CHAMBER AND DVCS SOLENOID

In the eg6 experiment, it is important to detect the recoiling ^{4}He and ensure that it

remains intact. However, these recoiling α-particles have low momentum and energy and the loss due to ionization will be high. They will stop and leave no tracks in solid detectors. Therefore, gas detectors will be a good choice to detect these particles. To meet these criteria, a new Radial Time Projection Chamber [32] was built which has similar design compared to the RTPC used in the BoNuS [33] experiment as shown in the Fig. 22.
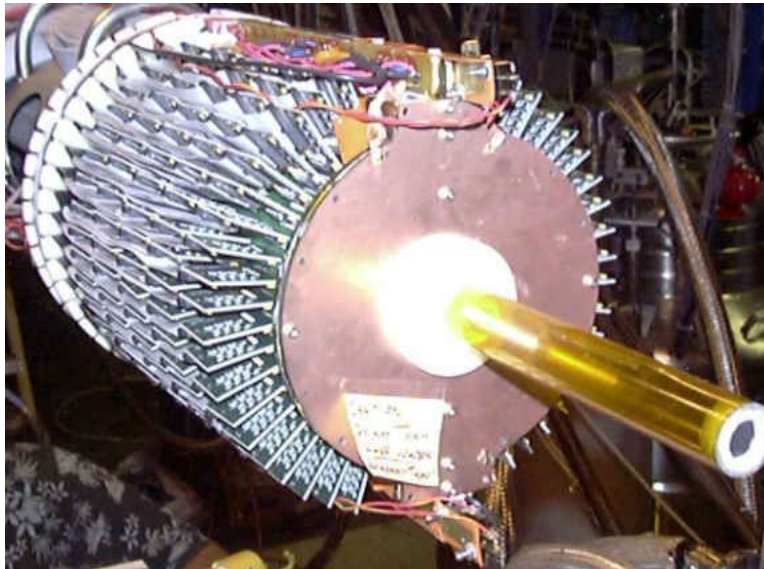
FIG. 22: Image of the BONUS Radial Time Projection Chamber.

If a particle passes through gas, it will ionize it along the path. Information about the path will be obtained by collecting these ionization electrons. The collection of electrons was done by the RTPC. The Radial TPC has cylindrical shape with outer radius 7 cm as illustrated in Fig. 23. The axis of the RTPC is parallel to the beam line and the length is 20 cm. There are three regions in the RTPC from target wall to outer surface. The first region is filled with low pressure ^{4}He gas in order to reduce secondary scattering and it extends from 3 mm to 20 mm. It is enclosed by a 4 μm thick Al-Mylar foil which is grounded. The second region is surrounded by 4 μm thick Al-Mylar foil with radius 30 mm (cathode) and connected to high voltage to produce an electrical field in the drift region. The third region or drift region of this detector is between 30 mm and 60 mm. This region and the second region are filled with a mixture of 80% Ne and 20% dimethyl ether (DME) gas. Here, DME is used to absorb photons to prevent secondary ionization. The drift region is surrounded by three concentric Gas Electron Multiplier (GEM) layers with radii 60 mm, 63 mm and 66 mm, respectively, which will be discussed in the next section. The electronic readout pad layer also has cylindrical shape and is located 70 mm from the axis of RTPC. There are

3,200 pads on this readout surface and for every 16 pads there is one 16-channel preamplifier connected on the outer surface.
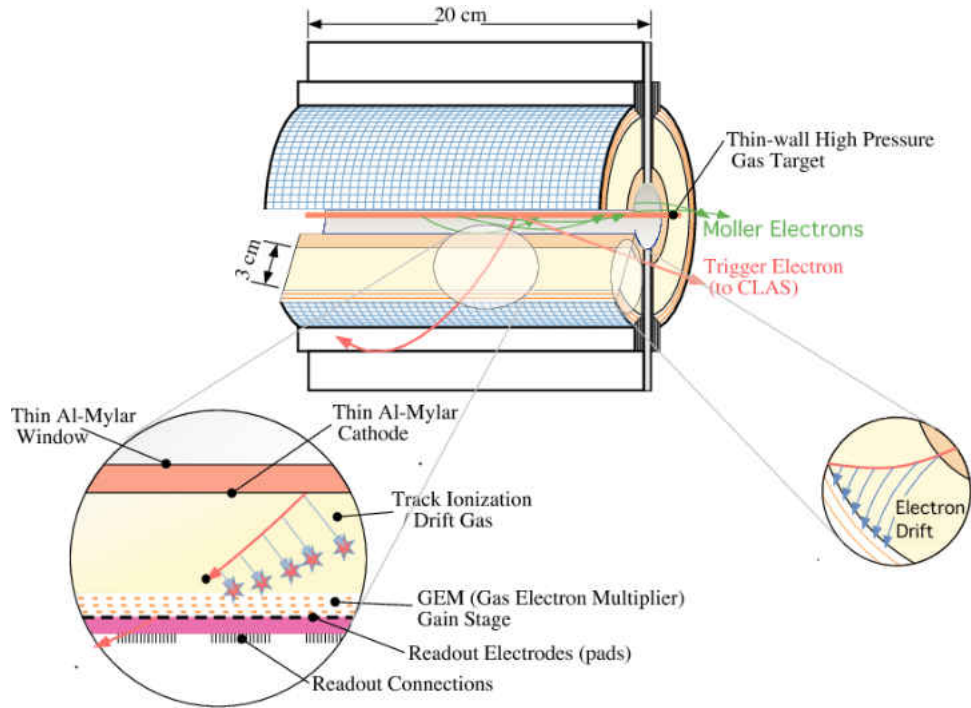
FIG. 23: Working principle of the RTPC. The picture is from [33].

When the recoiling nucleus passes through the drift region, it ionizes the neon gas. By applying a voltage difference across the region, the electrons will move toward the readout surface where they are amplified by GEMs. Then, readout pads collect these amplified electrons and the location of pads give information about the position of drift electrons. Also, the time for drift electrons to reach the outer surface allows measuring radially where they were produced. Here, it is important to calculate accurately the drift velocity of electrons inside the gas mixture. However, during the experiment, Moller electrons are also produced. If these electrons enter the sensitive region, they will mix with the electrons produced by ^{4}He. To avoid these electrons entering the drift region, a magnetic field, which is supplied by the DVCS solenoid, parallel to the beam is applied. As a result, Moller electrons are bend into helical paths around the beam axis and they do not enter the active region which begins only at a radius of 3 cm. Moreover, this magnetic field also bends nuclei and thus, allows measuring the momentum via the curvature of the trajectory.

3.6 GAS ELECTRON MULTIPLIER (GEM)

The Gas Electron Multiplier foils are made up of a thin polymer foil as insulator, both sides coated with copper layers. It consists of a high density of chemically pierced holes as illustrated in Fig. 24(a). The diameter of these holes is 50 μm. When an electrical potential difference (up to 300 V) is applied between the copper layers, a strong electric field will be generated inside the holes, as shown in Fig. 24(b).

(a)

(b)
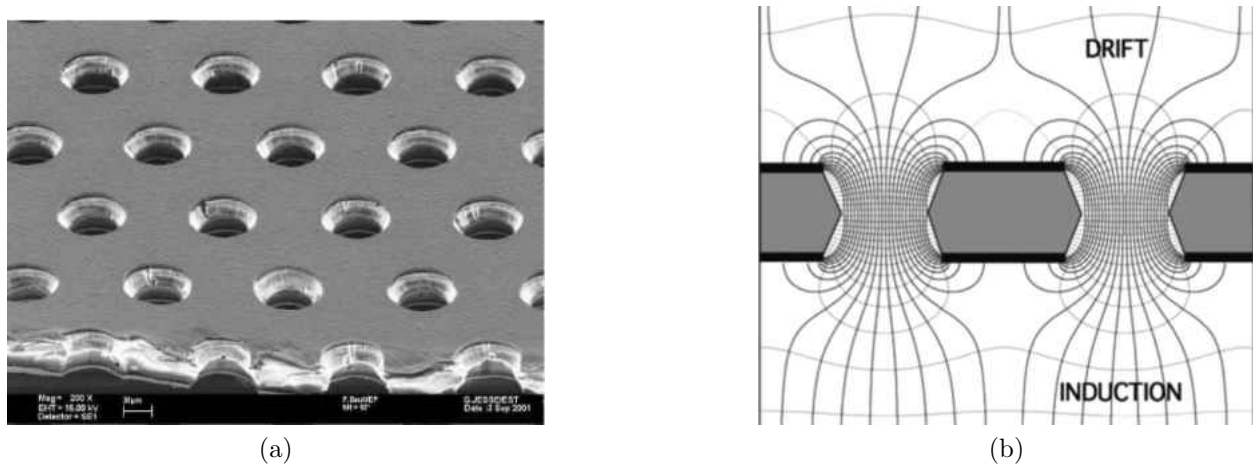
FIG. 24: (a) A picture of the GEM foils showing holes and Kapton insulator. (b) Side-view of the GEM showing electric fields.

The electrons ionized by charged particles in the drift region will be subjected to a high electric field inside the holes and will gain enough energy to ionize molecules of the gas in the medium. A large amount of avalanche electrons will be produced in the holes, resulting in amplification of the signal. Then, these electrons will be directed to the next GEM layer for additional amplification or readout pads where they can be collected.

3.7 TARGET

In the eg6 experiment, the momentum of the recoil nucleus is very small. It is very important that there is as little material as possible in the path of the nucleus:

- As diameter of the target cell increases, the thickness of the cell wall also increases to keep the target gas at the same pressure.

- If the target cell diameter is small, there is the possibility that the beam will pass through it.

Taking into account these constaints, a helium-4 gas target with 20 cm length and 6 mm diameter was used in the experiment. It is located at -64 cm from the nominal CLAS center.

The cell wall of the target was made out of 27 μm thick spirally wound Kapton foil. There are two aluminum windows of 15 μm thickness at the upstream and downstream ends of the target. The pressure of the gas was kept at 6 atm.

CHAPTER 4

DETECTOR CALIBRATIONS

In the eg6 experiment, the CLAS detector package, Inner Calorimeter and Radial TPC were used in order to detect scattering particles. The purpose of the calibration is to obtain calibration constants for each detector to extract timing and energy information. Thus, the calibration of detectors is very important for the reconstruction of particles. In this experiment, the TOF was calibrated by Lamiaa Elfassi, DC and EC timing was done by the author, IC was calibrated by F.X. Girod and the RTPC was calibrated and alignment was done by Nathan Baltzell, Mohammed Hattawy and Raphel Dupre [37, 38, 34]. In the following sections, DC [35] and EC [30] timing calibrations will be discussed briefly.

4.1 DRIFT CHAMBER CALIBRATION

CLAS drift chambers are separated into six sectors due to the torus magnet. Each sector has been divided into three regions and each region has two super-layers as shown in Fig. 25. Each superlayer has six layers of sense wires except the first superlayer which has only four layers of wires due to space limitation.
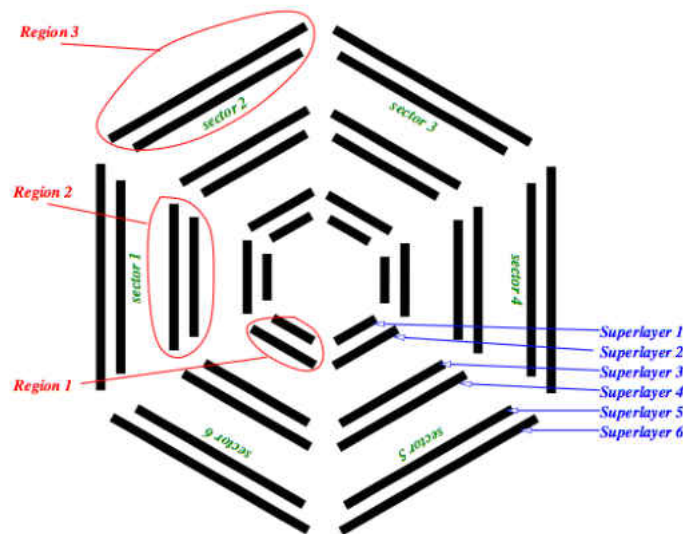
FIG. 25: The schematic view of drift chambers showing regions and superlayers.

When a charged particle passes through drift chambers, in average 30 layers out of 34 layers of the sense wires will be fired due to inefficiencies and dead regions in the DC. Each hit detected in the chamber is used to reconstruct the particle's track by using a least squares fit with the CLAS reconstruction software. The distance from the fired sense wire to the fitted track is called the distance of closest approach, DOCA. The calculated distance, using drift velocity and drift time, from the sense wire to track is known as DIST. The drift time is the time it takes ionized electrons to reach the sense wire from the track. The difference DOCA and DIST, known as "time residual" is called RESI. The track reconstruction process has two steps. In the first step, all fired sense wires are connected to obtain the form of the track, known as Hit-Based Tracking (HBT). In the next step, DIST is calculated using the drift velocity with calibrated parameters, and drift time of the particle is obtained. This is referred to as Time-Based tracking.
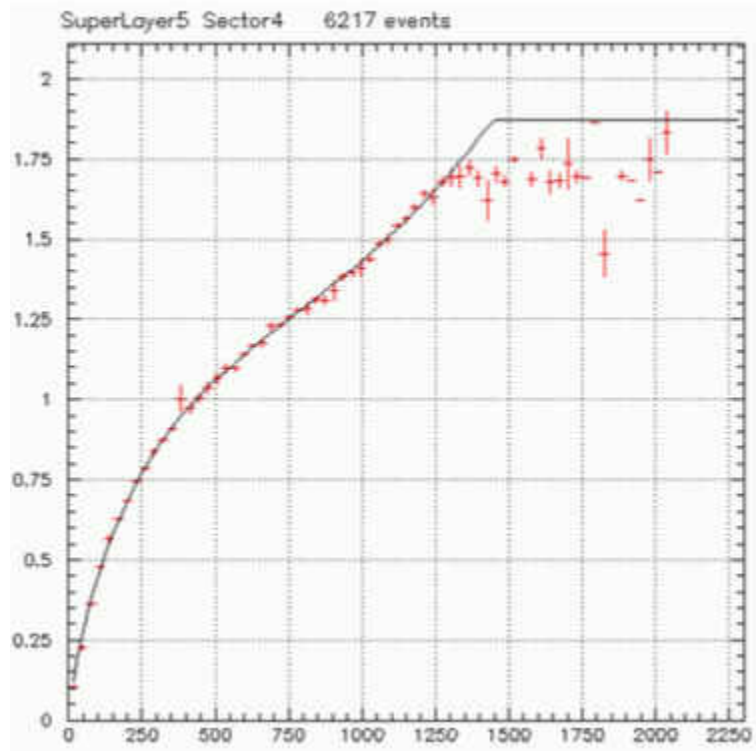
FIG. 26: DOCA vs drift time.

The goal of the drift chamber calibration is to get the parameters of the drift velocity function for each superlayer in every sector. These parameters can be obtained by fitting DOCA versus drift time plots as shown in Fig. 26, which is produced from the experimental data, since the velocity function is the relation between DIST and the time. This process

reiterates until the parameters converge and a small RESI is obtained. Then, 36 new sets of parameters are entered into the calibration database of the experiment.

4.2 TIMING CALIBRATION OF FORWARD CALORIMETER

The electromagnetic calorimeter (EC) in CLAS serves several uses that were discussed in the previous chapter. In this section, the timing calibration of the calorimeter will be discussed since a good EC timing can be used to discriminate between neutrons and photons. In addition, if there is any dead channel in Time Of Flight counters (TOF), the EC timing information can be used as a start time.

After calibrating the TOF counter with eg6 data, the electron's time measured by TOF was used to calibrate the EC timing. The path of the electron between TOF and EC is a straight line because there is no magnetic field between them. The distance between the two detectors and the impact angle of the electron onto the EC plane are known. Therefore, it is possible to calculate the EC timing as follows:

$$T_{EC} = T_{SC} + \frac{D_{path} \cos(\theta)}{c} \tag{46}$$

where T$_{SC}$ is the time measured by TOF, D$_{path}$ is the distance between TOF and EC planes and θ is the impact angle of the electron onto the EC plane. The time measured by EC can be parameterized as:

$$T_{EC} = a_0 + a_1 TDC + \frac{a_2}{\sqrt{ADC}} + a_3 L^2 + a_4 L^2 - \frac{L}{c_{Light}} \tag{47}$$

In the equation above, c_{Light} is the speed of light in the scintillator, L is the distance between the centroid of the shower to the readout edge of the EC strip with the largest ADC value. The first term in the Eq. (47) corresponds to constant times such as delays due to the length of the cable. The second term is the conversion of the TDC value to time in ns. Time-walk correction is the third term. The forth and fifth terms are related to the light attenuation lengths. The last term is the time it takes the light to travel from the hit position to the readout edge of EC. A least-square fit was performed on the estimated time in Eqn. (46) with the parameterized time as in Eqn (47) to obtain the parameters of the measured time in EC. Then, theses parameters were written to the calibration database. The results of the calibration can be seen in Fig. 27.
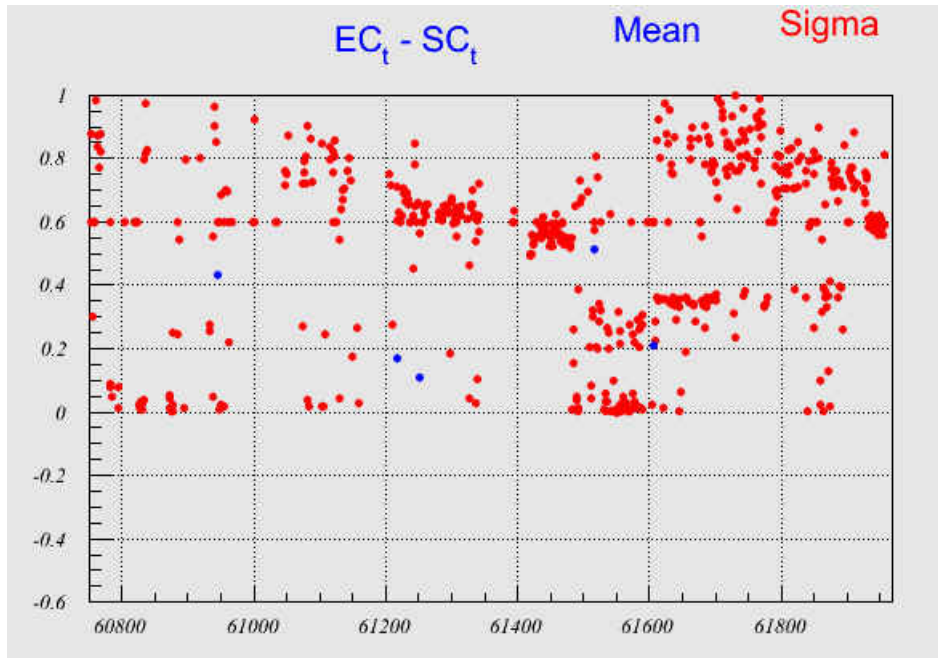
(a)
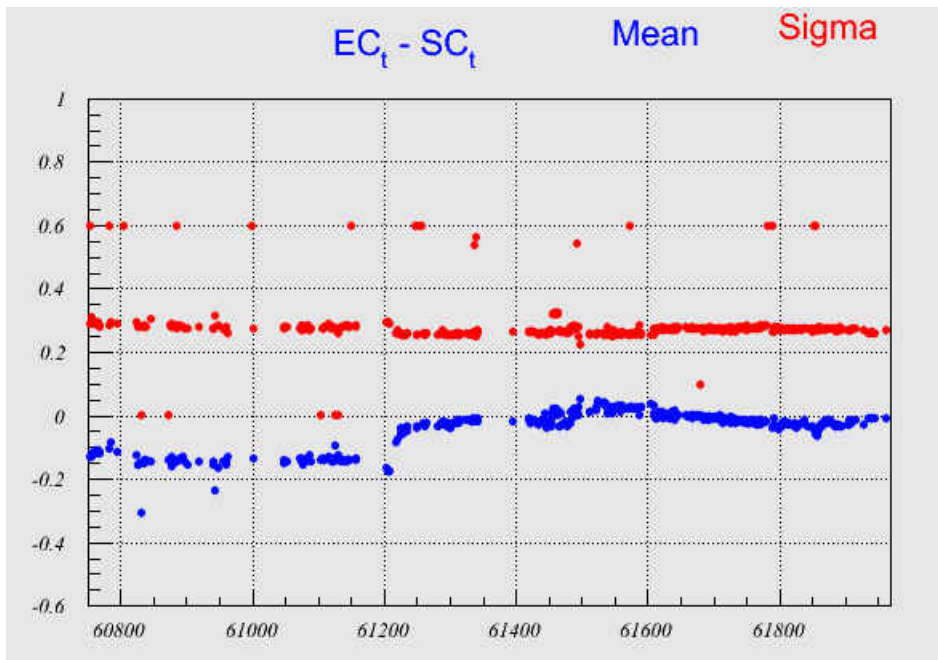
(b)

FIG. 27: Run by run plot of the mean and sigma values of the time difference between EC and SC (a) before and (b) after the calibration.

CHAPTER 5

PARTICLE SELECTION AND DATA ANALYSIS

In this analysis, electroproduction of the π^0 scalar meson off helium-4 is studied in the fully exclusive channel:

$$\text{eHe} \rightarrow \text{e}'\pi^0\text{He}' \tag{48}$$

where the π^0 is reconstructed by two photons. To select coherent π^0 electroproduction events, all final state particles were identified and events with an intact ^{4}He nucleus in the final state were selected. Exclusivity cuts were applied, which will be discussed in the next chapter.

This chapter discusses data quality, particle identification procedures for electron and helium-4, and the π^0 reconstruction process using two photons.

5.1 VERTEX CORRECTION

The vertex of the charged particles is defined as the intersection point of the track with the plane which is perpendicular to the mid plane of the sector and containing the beam line. The CLAS reconstruction software reconstructs the vertices of the charged particles by assuming the beam to be at the point (0, 0). If there is a shift in beam position from (0, 0), the vertex will have a ϕ dependence as shown in Fig. 28(a). In the eg6 experiment, the solenoid magnet was used as a shield from Moller electrons of the RTPC and the IC and to bend the track of the recoiling, charged nucleus. The magnetic field at the vertex is very large, which causes the parameters of the particles reconstructed to be incorrect. In addition, the RTPC uses beam offsets as a starting point of the helical path through the drift volume. Thus, having a correct beam position and vertex [39] is very important.

To get the correct vertex and beam offset, the following equation was used:

$$z_{corr} = z_{rec} + \frac{r}{\tan(\theta)} \cos(\phi - \phi_0) \tag{49}$$

where z_{corr} is the real vertex, z_{rec} is the initially reconstructed vertex by assuming the beam position was at (0, 0) and r is the distance between the beam position and (0, 0) as shown in the Fig. 29. θ and ϕ are polar and azimuthal angles of the scattering electron, respectively. The beam offset parameters, r and ϕ_0, were obtained by fitting the vertex of the electrons with polar angle $\theta = 30°$ at the downstream windows versus ϕ with the function in Eq. 49.
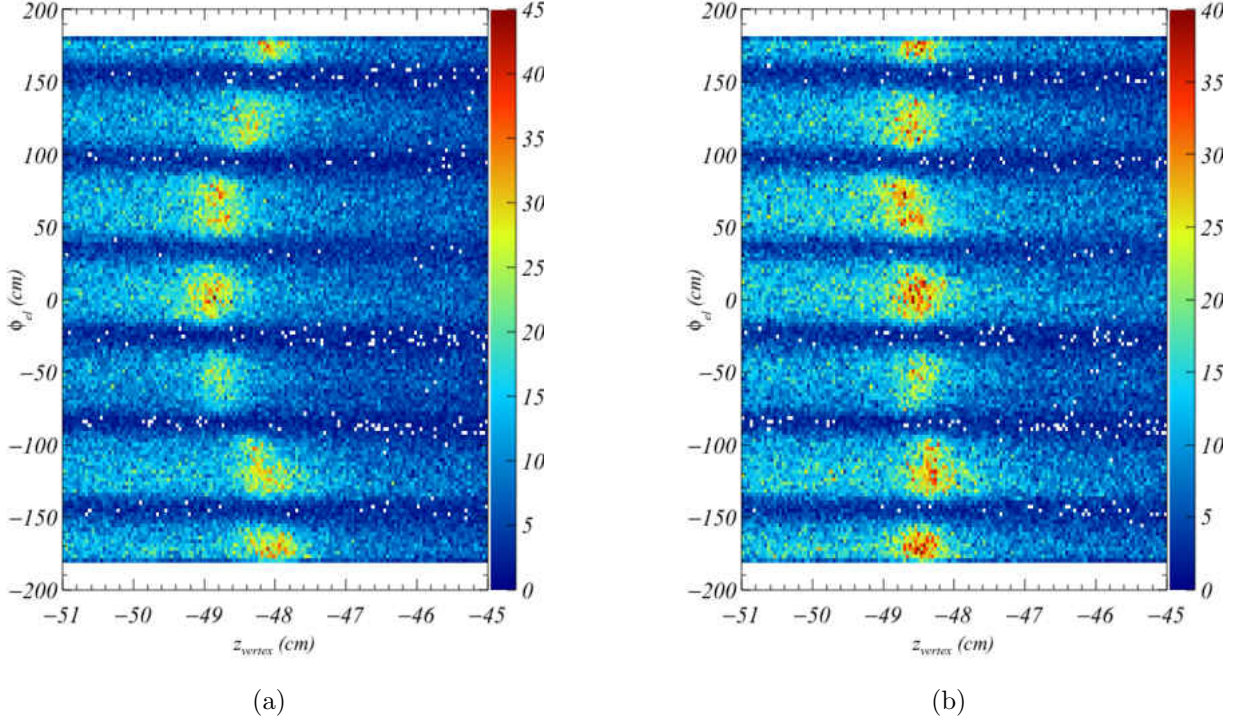
FIG. 28: The vertex z versus ϕ angle of the electron candidates (a) before and (b) after the correction.

The result of the correction can be seen in Fig. 28(b), where there is no angular dependence. Therefore, it is possible to apply the same production vertex cut for all sectors which is discussed in the next section.

5.2 ELECTRON IDENTIFICATION

Identification of electrons in an electroproduction experiment with CLAS is very important since the electron is the triggering particle. In order to select good electrons, several cuts were applied, which are discussed below.

1. **status cut:** Charged particles' tracks in DC are reconstructed in two steps, Hit-Based Tracking(HBT) and Time-Based Tracking(TBT). If *status* variable is required to be positive, the particles that pass the HBT step but fail the TBT step are rejected.

2. **Negative charge:** The Torus Magnet in CLAS provides a magnetic field almost in azimuthal angle which bends the charged particles toward (negatively charged particle)
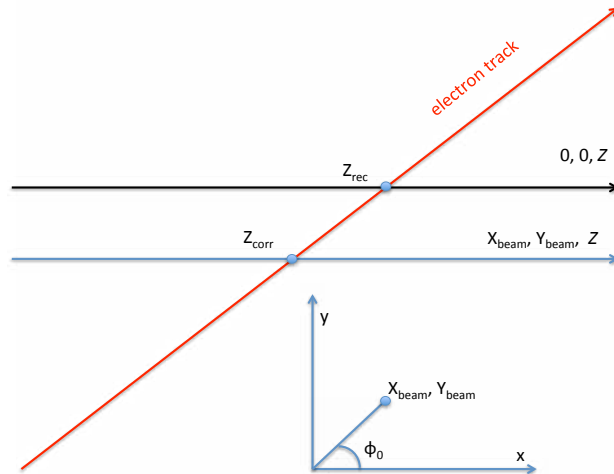
FIG. 29: Schematic veiw of the variables used in the vertex correction.

or away (positively charged particle) from the beamline, depending on the polarity of the Torus. Therefore, the trajectory of the particle in the DC gives information about its charge.

3. **DC momentum cut:** The DC-derived momentum of the particle has to be greater than 0.65 GeV, in order to minimize π^- contamination.

4. **Geometrical match:** As mentioned above, the CLAS detector is divided into six segments or sectors. It is possible to reduce accidentals or coincidences by equating sector numbers of each sub-detector in CLAS.

5. **Vertex cut:** The target center was placed -64 cm (upstream) from the nominal center of CLAS. In Fig. 30, the z-vertex distribution of charged particles is shown after applying vertex corrections and following cuts 1, 2, 3 and 4. The two peaks on the left and right in the same figure are the upstream and downstream target windows, respectively. In this analysis, we select particles with a z-vertex range between -74 cm and -54 cm relative to the CLAS center which corresponds the red lines in Fig. 30. The reason of selecting this range is that it minimizes the particles produced through interaction with target walls and corresponds to the drift region of RTPC.
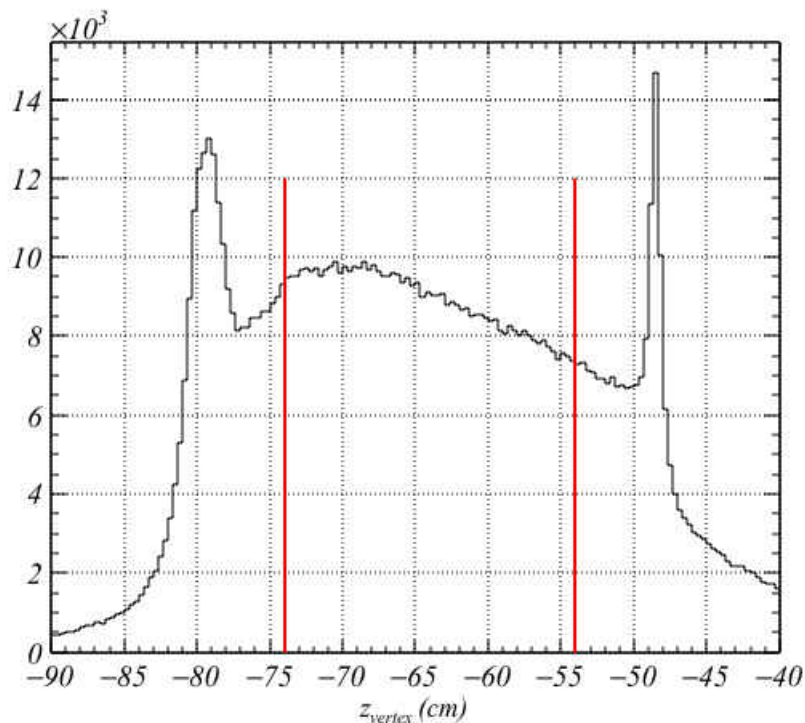
FIG. 30: Charged particles' z vertex distribution that passed the following cuts: 1, 2, 3 and 4. The red lines corresponds to the cut -74 cm $< z_{electron} <$ -54 cm which is the drift region of the RTPC.

6. **EC inner energy cut:** Pions are minimum ionizing particles and loose their energy by ionization. The deposited energy by ionization mainly depends on the thickness of material and is independent of its momentum. The electromagnetic calorimeter consists of 13 layers. Energy deposited by particles in the first 5 super layers are called inner energy and the energy deposited in the remaining 8 super layers is labelled outer energy. The energy deposition rate of negatively charged pions in the inner layer of EC is equal to 2 MeV/cm and the thickness of the layer is 15 cm. Therefore, pions loose about 30 MeV energy when they pass through the inner layer. Fig. 31 shows the inner energy versus outer energy deposited by particles that pass the cuts above. One can see a peak at around 30 MeV, which corresponds to negative pions. The minimum energy in the inner layer of the EC has to be greater than 60 MeV in order to reject these pions.

7. **Soleniod fiducial cut:** In the eg6 experiment, the solenoid magnet was used for
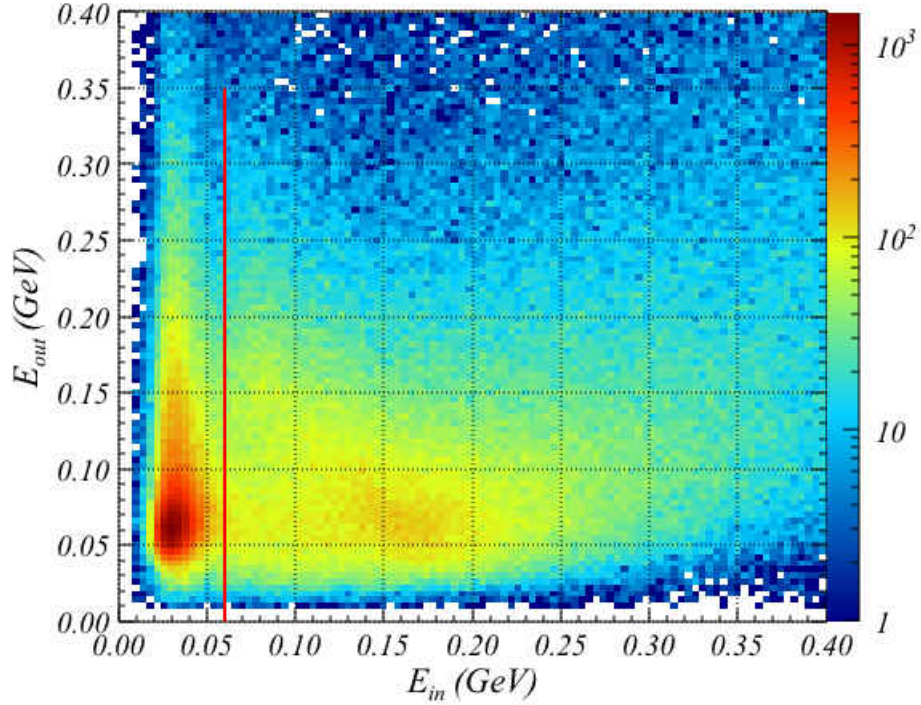
FIG. 31: Energy deposit in the inner layer versus energy deposit in the outer layer.

tracking recoiling nuclei and shielding Moller electrons. The particle with high polar angle interacts with the structure of the magnet and looses energy, so the reconstruction of the momentum and position of the particle is not good enough. Therefore, a vertex dependent polar angle cut was applied to reject these particles. In Fig. 32, the polar angle versus vertex of the particles that pass the cuts above was plotted. The events above the red line were rejected.

8. **EC fiducial cut:** When a particle hits the edges of the EC, some part of its energy is not recovered well. Therefore, standard EC fiducial cuts were applied in order to reject these particles. To apply the cuts, the hit positions in the EC in CLAS coordinates (x, y, z) were converted to the EC coordinate system (u, v, w). In this analysis, the following cuts were applied: 60 cm $< u <$ 390 cm, $v <$ 360 cm and $w <$ 390 cm as shown in Figs. 33 (a), (b) and (c). The effect of the fiducial cut is illustrated in Figs. 33 (d), (e) and (f), where the hit positions of the particle is plotted in (x, y) coordinate.

9. **IC Shadow fiducial cut:** The Inner Calorimeter is positioned in the center of CLAS

FIG. 32: The polar angle θ versus vertex $z_{electron}$ of the electron candidates. The events above the curved red line were rejected since they will interact with the solenoid magnet or with its structure.

which either blocks or interacts with small scattering angle particles. The position and momentum of particles that interacted with IC or with its supporting structure is not reconstructed well. To reject these particles, a fiducial cut was applied. In Fig. 34, the left plot shows the projection of (x, y) position of drift chambers in the first region to the IC front face plane before the fiducial cut. The right one shows the events that passed this cut.

10. **Sampling fraction:** Electrons are showering particles while pions are minimum ionizing particles. Therefore, the ratio of the total deposited energy in the calorimeter by the electron to the momentum of the electron $\left(\frac{E_{tot}}{p}\right)$ should be independent of momentum. The ratio is called sampling fraction and is equal to 0.3. However, the experimental data show a momentum dependence of the sampling fraction which changes with sector number due to energy losses of the electron in CLAS during the flight and attenuation of light collected in the calorimeter as illustrated in Fig. 35. In order to develop momentum dependent cuts to reject pions, the $\frac{E_{tot}}{P}$ vs P distributions were divided into 50 MeV bins along the P axis. Each bin was fitted with a Gaussian function and third
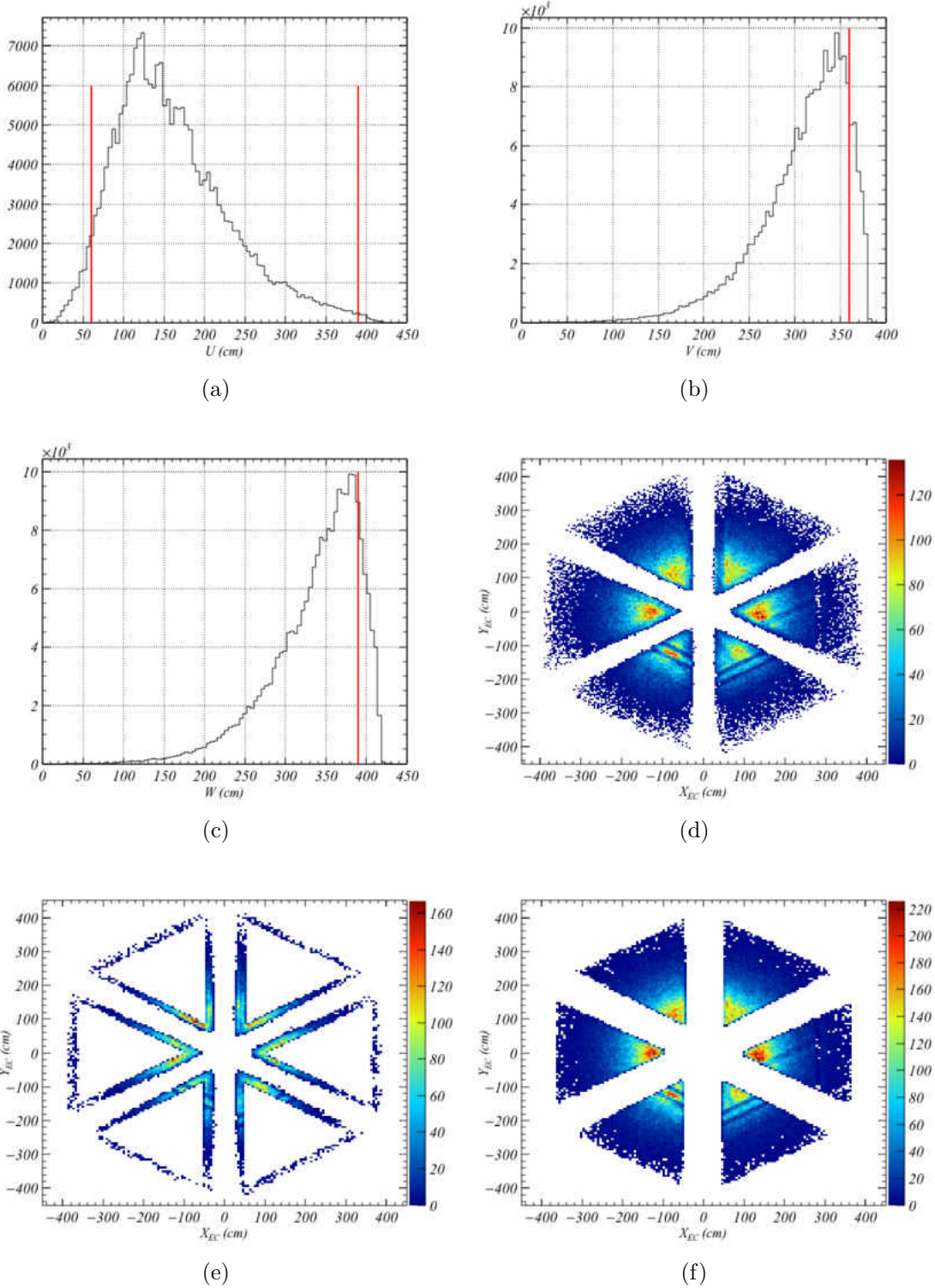
FIG. 33: EC fiducial cut applied on the electron (a) u, (b) v and (c) w coordinates in EC. The red line indicate the cut. The EC x, y hit for (d) all, (e) rejected and (f) accepted events.

(a)   (b)
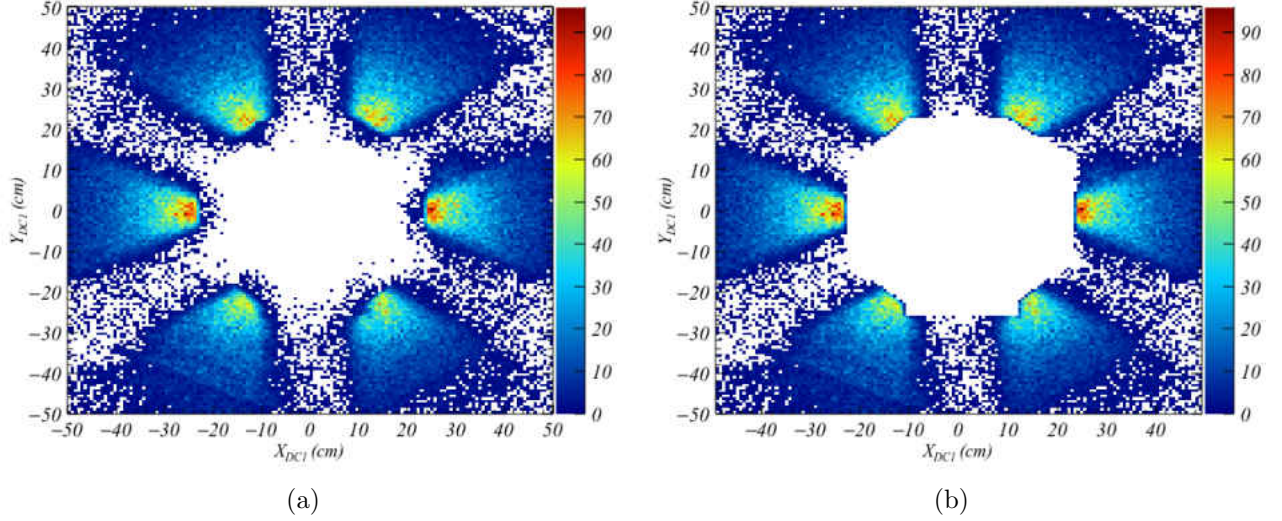
FIG. 34: The IC shadow fiducial cut. The x, y values of the first region of DC (a) before and (b) after the cut.

order polynomial to get the mean and sigma. Then, these mean and sigma values were fitted with the following functions to get a functional form of the mean, μ, and sigma, σ, of the momentum:

$$\mu(p) = a + b \cdot p + c \cdot p^2 + d \cdot p^3 \tag{50}$$

$$\sigma(p) = \frac{e}{\sqrt{f + p}} \tag{51}$$

In Fig. 35, the black line represents $\mu(p)$ and the red lines corresponds to $\mu(p) \pm 3.5\sigma(p)$. The events in between the red lines ($|\frac{E_{tot}}{P} - \mu(P)| < 3.5\sigma(P)$) were accepted as electrons. In Table 1, the values of the parameters of the $\mu(p)$ and $\sigma(p)$ were given for each sector.

TABLE 1: Parameters for sampling fraction.

Parameter	sector1	sector2	sector3	sector4	sector5	sector6
a	0.2490	0.2636	0.2721	0.2727	0.2593	0.2517
b	0.0676	0.0557	0.0563	0.0507	0.0476	0.0562
c	-0.0182	-0.0132	-0.0127	-0.0117	-0.0100	-0.0137
d	0.0019	0.0012	0.0012	0.0011	0.0009	0.0013
e	0.0469	0.0508	0.0518	0.0427	0.0469	0.0440
f	0.6123	1.3342	1.5067	0.6838	0.4713	0.4299

5.3 HELIUM-4 IDENTIFICATION

In coherent electroproduction of neutral pions off ^{4}He with 6 GeV beam energy, the recoiling nuclei will have low momenta well below the CLAS threshold. To detect and identify these recoiling nuclei is very important. Therefore, the RTPC was built and calibrated. In this section of the analysis, the helium-4 identification in RTPC will be discussed. To do so, events with one electron were used and the following cuts were developed:

1. **Number of pads:** The track in RTPC should have at least 4 different active readout pads.

2. **Positive curvature:** The recoiling particles will turn in a clockwise or counterclockwise direction depending on the polarity of the solenoid magnetic field. The curvature of the tracks must have positive curvature as illustrated in Fig. 36(a), since recoiling α-particles are positive and the magnetic field direction is along the beam axis.

3. *edist*: The variable *edist* is the closest ionization point along the track of the helium-4 to the anode. The *edist* distribution is shown in Fig. 36(b) where the left (right) red line represents the cut corresponding to -5 (10) mm.

4. **Vertex cut:** The vertex distribution of the tracks that passed the cuts 1, 2 and 3 above is shown in Fig. 36(c). $|z_{he}| < \pm 110$ (mm) cut was applied to ensure that the particle is inside RTPC.

5. *sdist*: *sdist* is the closest distance of the ionization points along the track to the cathode. The distribution is illustrated in Fig. 36(d) and the cuts (± 5 (mm)) are represented with vertical red lines.

6. χ^2: χ^2 is the fit quality of the helix track and it has to be smaller than 3.0 (see Fig. 36(e).

7. **Polar angle:** Simulation studies showed that the polar angle of the helium-4 can be between $20° < \theta_{he} < 80°$. Thus, events with polar angle ranging from $20°$ to $80°$ were chosen as illustrated in Fig. 36(f).

8. **Fiducial cut:** The track of the recoil nucleus can hit the mechanically supporting structures of the RTPC or some part of the path can be outside the sensitive region. As a result, these tracks may not be reconstructed well. Therefore, these events were

rejected from the sample by applying a fiducial cut as shown in Fig. 37. The left (right) plot shows the distribution of the ϕ angle versus z_{he} before (after) the cut.

9. **Vertex matching:** The distribution of the vertex difference of the electron and helium-4 is shown in Fig. 38. It is fitted with a Gaussian function and third order polynomial. The events within the range $|\delta z - \mu| < 3.5\sigma$ were accepted.

TABLE 2: Summary of the cuts to select helium-4

cuts	variable	value	unit
1	N_{pads}	>3	
2	r_0	>0	
3	$edist$	$\in [-5, 10]$	mm
4	z_{he}	$\in [-110, 110]$	mm
5	$sdist$	$\in [-10, 10]$	mm
6	χ^2	< 3	
7	θ_{he}	$\in [20, 80]$	deg
8	Fiducial cut		
9	δz	$\in [-2.39, 2.31]$	cm

In Table 2, a summary of all cuts is given that were applied to choose good helium-4 events inside the RTPC.

5.4 EC PHOTON IDENTIFICATION

In this experiment, photons were detected by either the electromagnetic calorimeter (EC) or inner calorimeter(IC), each of which has different angular coverage. In this section, the procedure of photon selection will be described. The particles detected in EC, with no associated track in the drift chambers, are assigned as neutral particles. In order to separate photons from neutrons, the following cuts were applied to the events with at least one good electron.

1. **Minimum energy cut:** If the energy of the neutral hits in EC is smaller than 300 MeV, the position and timing of calorimeter is not reconstructed well. Therefore, the minimum energy in EC must be greater than 300 MeV.

2. **EC fiducial cut:** The same fiducial cuts were applied for neutral particles as for electrons. In Fig. 39, the x, y position of EC hits for neutral particles is shown before and after the fiducial cut.

3. β **cut:** The β of the neutral hits in EC can be calculated as following:

$$\beta = \frac{l}{c\Delta t} \tag{52}$$

where l is the distance from the vertex of the electron to the EC hit position and Δt is the difference of EC time and event start time. In order to separate photons from neutrons, a $\beta > 0.95$ cut was applied. In Fig. 40, β versus the energy distribution of photons is shown after applying the above cuts.

5.5 EC ENERGY CORRECTION

In this part of the analysis, the energy correction method, described in [36], of the photons using the two photon decay mode of the pion, $\pi^0 \to \gamma\gamma$, in EC will be explained. To do so, the samples that have at least one good electron and two photons in the same sector of the EC have been selected. The invariant mass of the two photons is calculated as following:

$$M_{\gamma 1 \gamma 2} = 2 \cdot \sqrt{E_{\gamma 1} \cdot E_{\gamma 2}} \cdot \sin(\frac{\theta}{2}) \tag{53}$$

where θ is the opening angle between the direction of the tracks of the two photons and $E_{\gamma 1}$ and $E_{\gamma 2}$ are the energy deposit of the photons in EC divided by the sampling fraction, $\text{f}_{sampl.}$ = 0.3. In Fig. 41, the distribution of the invariant mass of the photons versus energy was plotted where the energy dependence can be seen easily.

In this method, the opening angle between photons is assumed to be reconstructed correctly. Therefore, the energy in each sector is corrected individually since the geometry of the EC is very well described within a single sector. That is, photons have been detected in the same sector of the calorimeter. Lets assume that the correction function is $f(E)$. Then, the reconstructed mass of the pion will be:

$$M_{\pi^0} = 2\sqrt{\frac{E_{\gamma 1}}{f(E_{\gamma 1})} \frac{E_{\gamma 2}}{f(E_{\gamma 2})}} \sin(\frac{\theta}{2}) \tag{54}$$

where M_π = 0.135 GeV. The ratio of the equation 53 and 54 will be

$$\frac{M_{\gamma 1 \gamma 2}}{M_{\pi^0}} = \sqrt{f(E_{\gamma 1} \cdot f(E_{\gamma 2}))} \tag{55}$$

There are two steps involved to find f_E. In the first step, the correction function is obtained by selecting photons with almost same energies. However, this requirement limits the energy ranges. In the second step, one photon is selected within the energy limit where energy correction from the first step can be used. The energy range of the second photon will allow to get the function in a broader energy range. In this section, we will present corrections for the photons that are in the first sector of EC.

5.5.1 FIRST STEP OF THE CORRECTION

In this step, samples of photons with energies that fulfill the condition $1.00 < E_{\gamma 1}/E_{\gamma 2} < 1.04$ were selected. The photons are ordered according to energy $(E_{\gamma 1} > E_{\gamma 2})$. Then, equation 55 reduces to:

$$\frac{M_{\gamma\gamma}}{M_{\pi^0}} = f(E_\gamma) \tag{56}$$

The average energy $(E_{ave} = (E_{\gamma 1} + E_{\gamma 2})/2)$ is sliced into 50 MeV bins. In each bin, the $M_{\gamma\gamma}/M_{\pi^0}$ was fitted with a Gaussian function for the peak and polynomial of third degree for the background to get mean the values as shown in Fig. 42. Then, the mean values were fitted with the following function to get the parameters of the correction as illustrated in Fig. 43:

$$f(E) = p_0 + \frac{p_1}{E} + \frac{p_2}{E^2} \tag{57}$$

The energy range that can be used to correct is 0.4 GeV $< E_\gamma <$ 1.0 GeV from the first step. In Table 3, the parameters obtained from the first step are summarized for each sector.

TABLE 3: Parameters from the first step of the correction

Parameter	sector1	sector2	sector3	sector4	sector5	sector6
p_0	1.0600	1.2482	1.1760	1.1795	1.1915	1.1015
p_1	-0.0050	-0.1651	-0.539	-0.0919	-0.1569	-0.0401
p_2	-0.0236	0.0159	-0.0168	-0.0023	0.0142	-0.0186

(a)

(b)

(c)

(d)

(e)

(f)
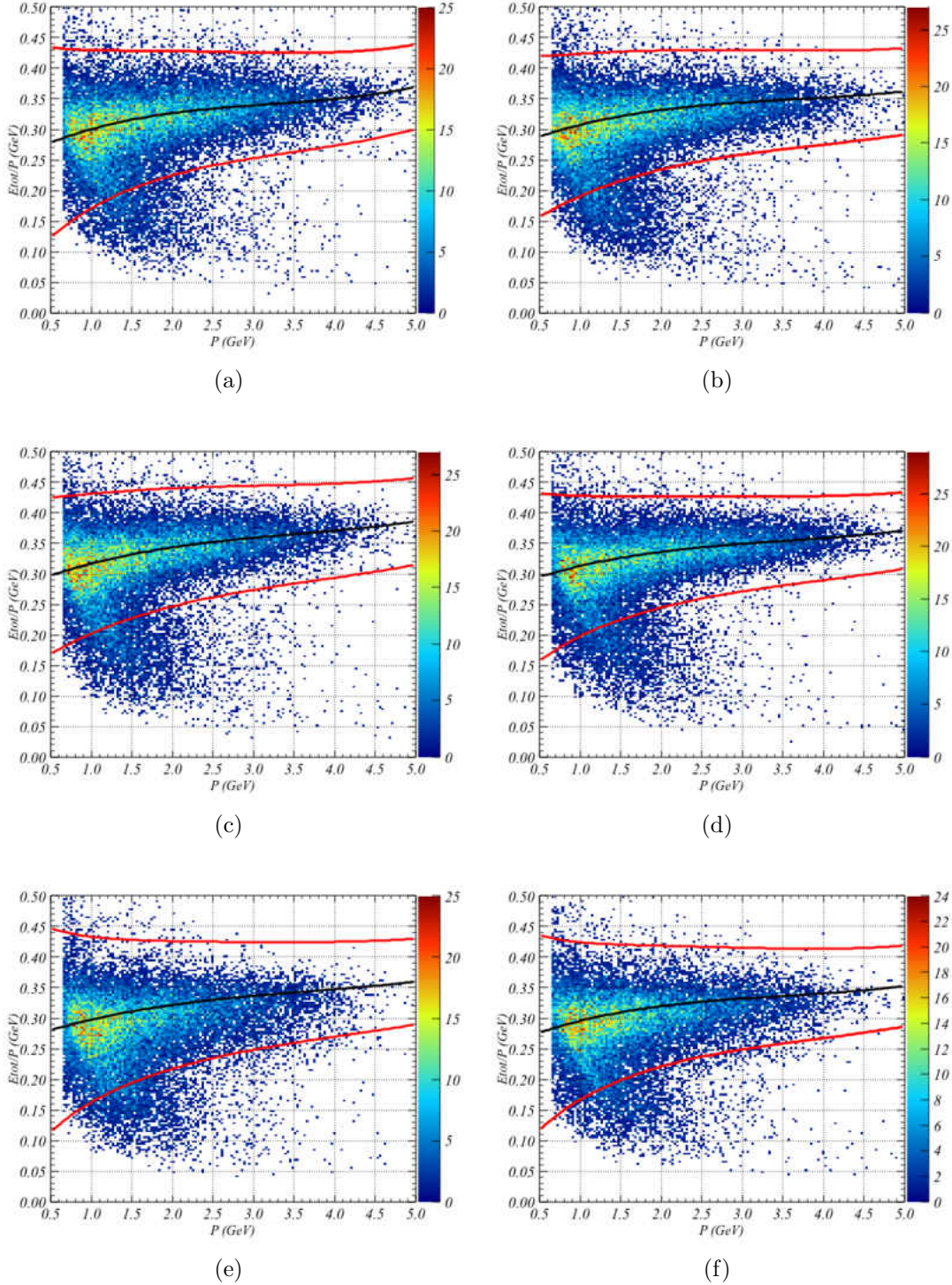
FIG. 35: E_{tot}/P versus P for electron candidates for each sector. The black line indicate the third order polynomial fit of the mean values of each bin in P. The red lines are the momentum dependent $\pm 3.5\sigma(P)$ cuts for sampling fraction.

(a)

(b)

(c)

(d)

(e)

(f)
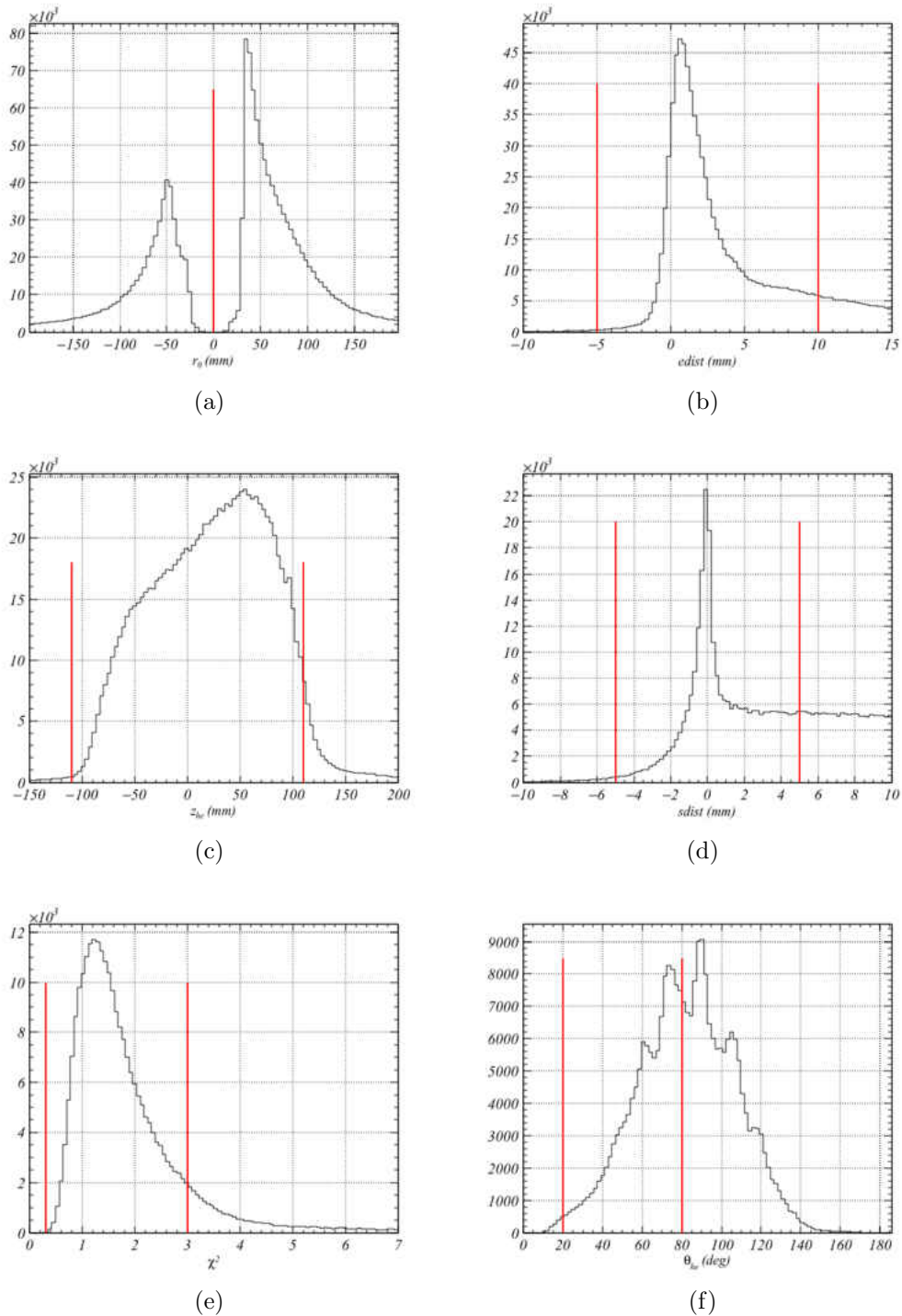
FIG. 36: Summary of the cuts on RTPC variables to select helium-4. (a) The curvature of the path. (b) The closest ionization point to the anode. (c) Vertex of the tracks. (d) The closest ionization point to the cathode. (e) Fit quality cut. (f) Cut on the polar angle of the track.
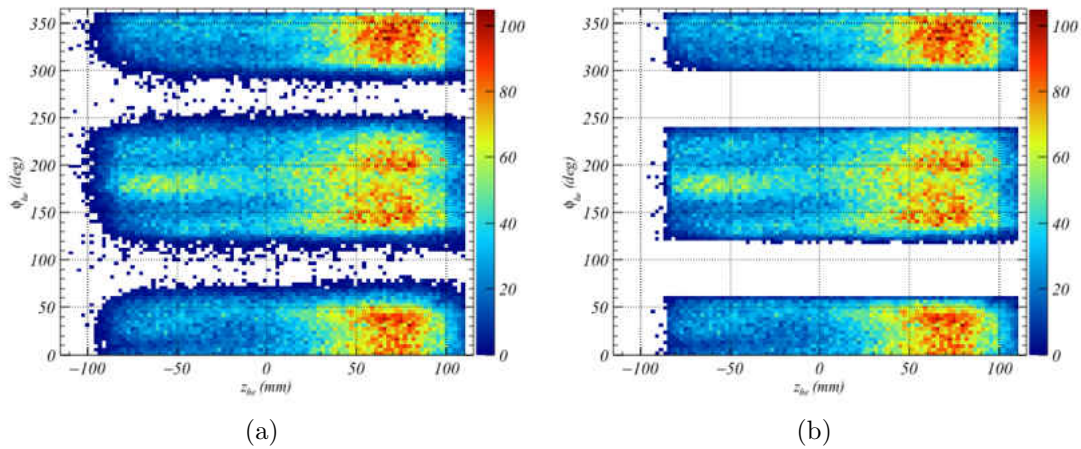
FIG. 37: The azimuthal angle versus vertex of the RTPC track in CLAS coordinates. (a) before and (b) after the fiducial cut.
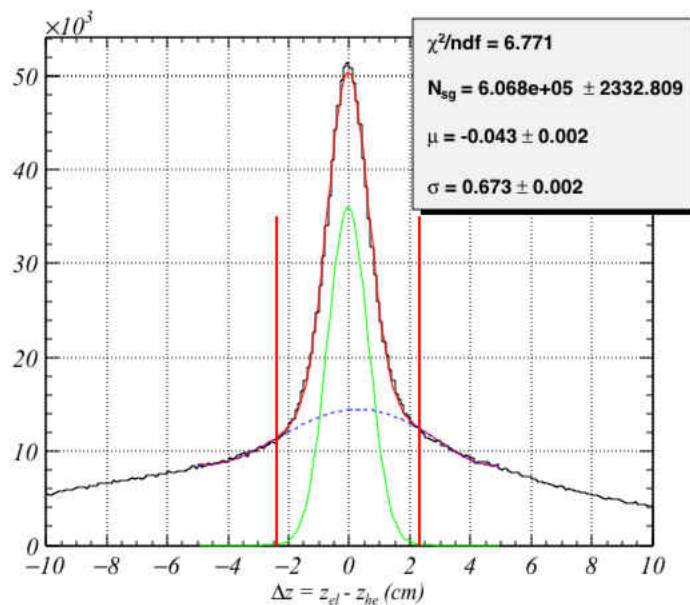
FIG. 38: The distribution of the difference between electron vertex (CLAS) and helium-4 vertex (RTPC). The vertical red lines indicate the cut.

(a)   (b)
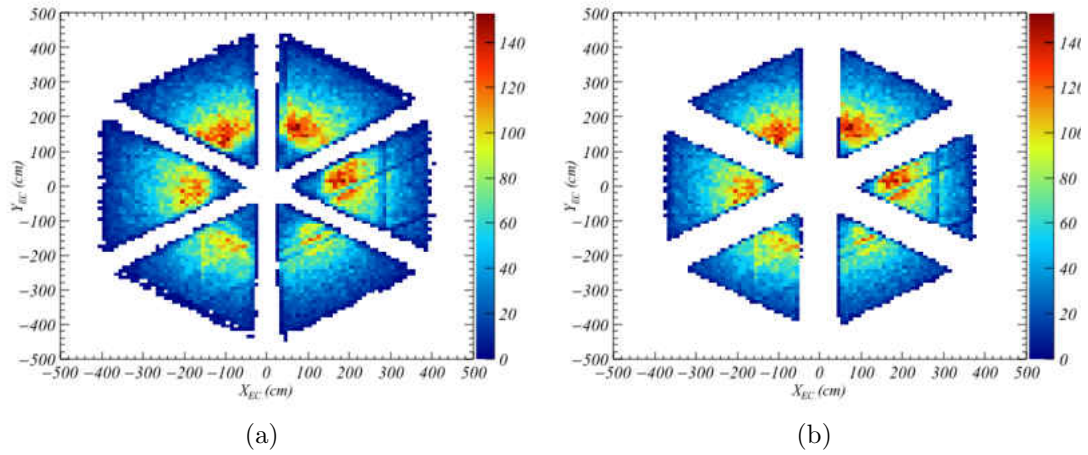
FIG. 39: (a)Before and (b) after applying EC fiducial cut.
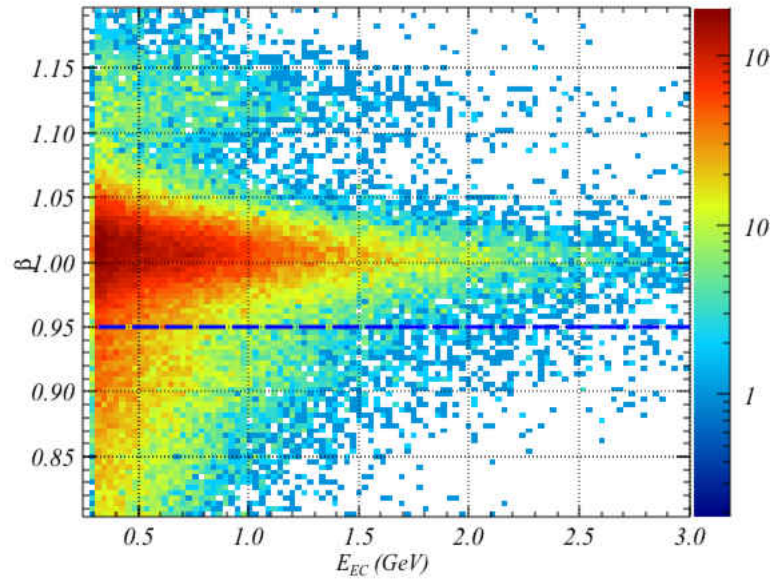
FIG. 40: β versus energy of the neutral hits in EC. The dashed blue line indicates the cut.
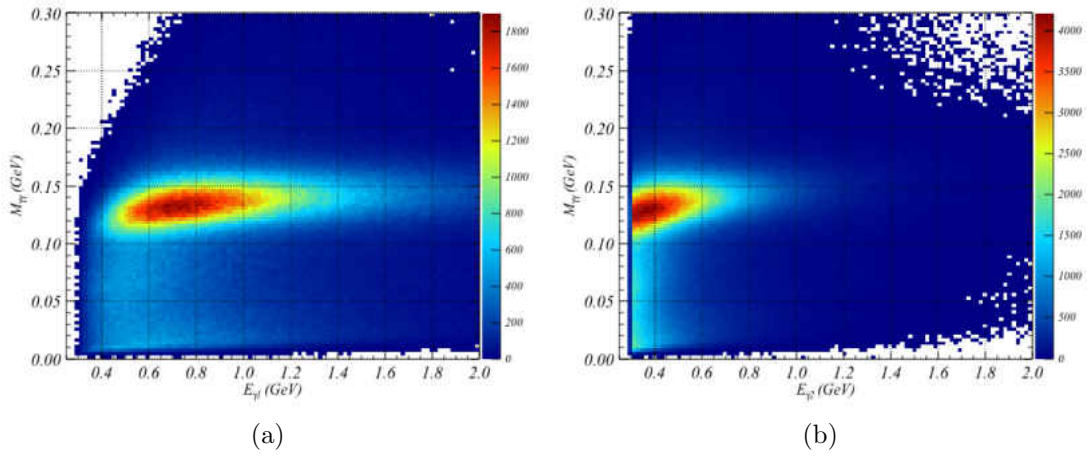
FIG. 41: Invariant mass two photons versus (a) first photon's energy and (b) second photon's energy.
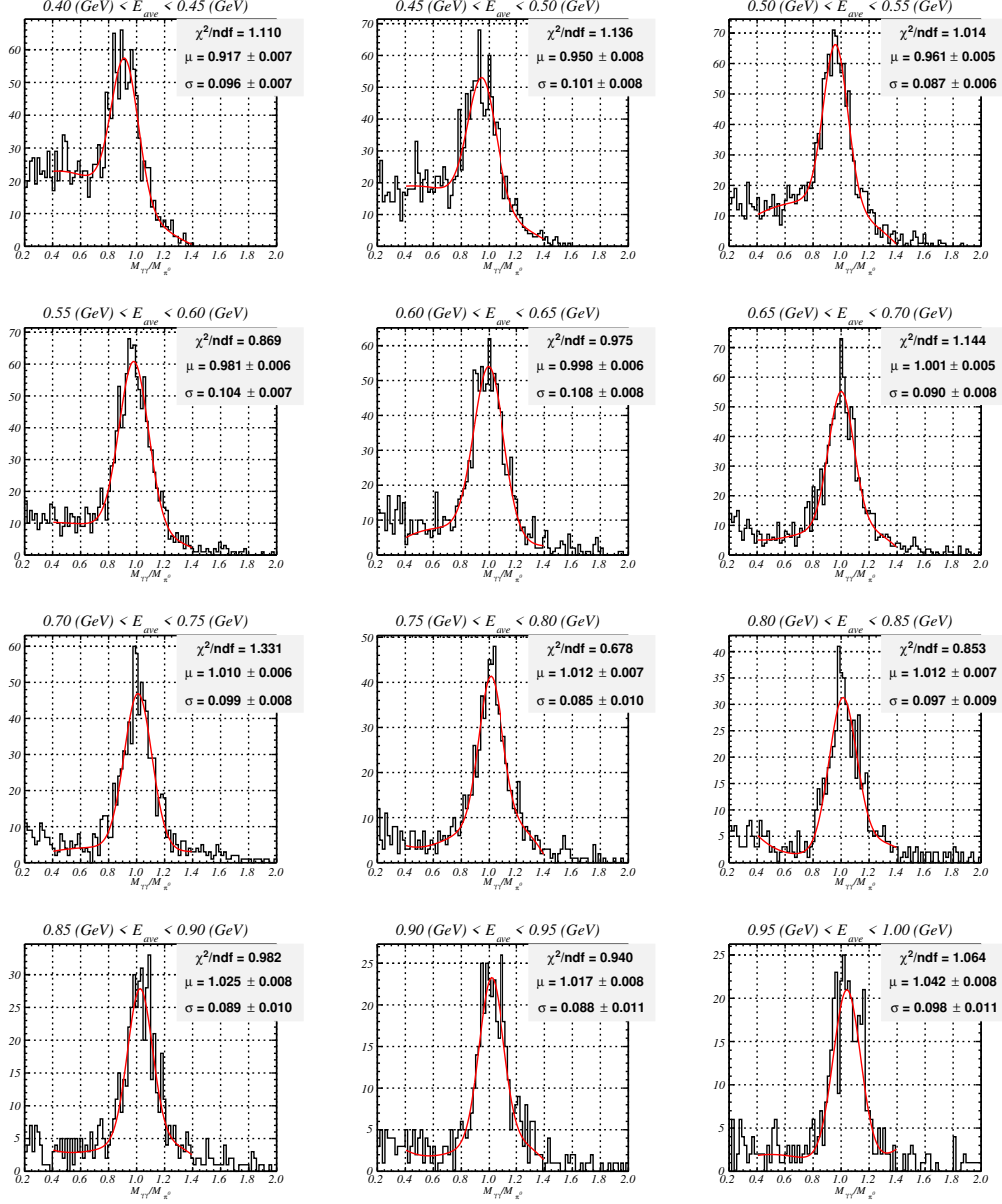
FIG. 42: First step correction. The ration of the $M_{\gamma\gamma}/M_{\pi^0}$ distribution for each bin in average energy. (example of first sector).
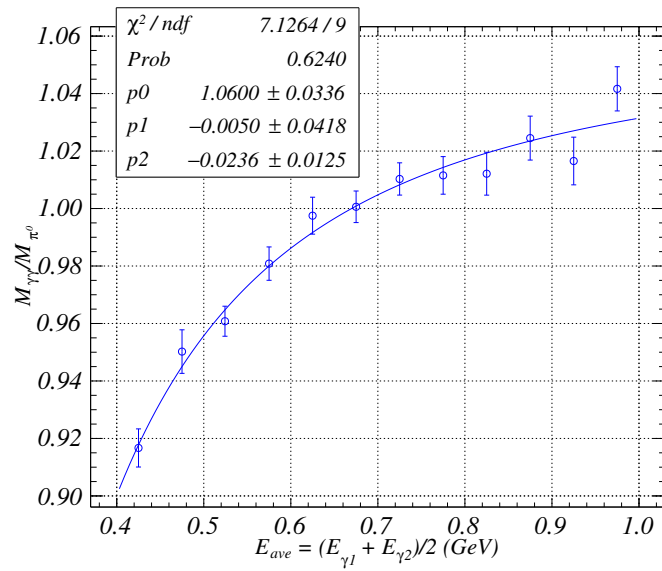
FIG. 43: The $M_{\gamma\gamma}/M_{\pi^0}$ as a function of energy (example of first sector).

5.5.2 SECOND STEP OF THE CORRECTION

In the second step of the correction, the samples that have been selected with the condition that one of the photons should have the energy within the limits from the first step (0.4-1.0 GeV) are taken. Then, this photon's energy is corrected with the correction function obtained from the first step. Assume the first photon's energy is within this limit, then equation 55 reduces to:

$$f(E_{\gamma 2}) = (\frac{M_{\gamma 1 \gamma 2}}{M_{\pi^0}})^2 \tag{58}$$

Again, a very similar procedure is used in this step also. The energy of the uncorrected photon is divided into 50 MeV bins between energy ranges $\in[0.3, 1.8]$ GeV, 100 MeV in the ranges $\in[1.8,2.3]$ GeV and the rest was taken as one bin due to limited statistics. The $(\frac{M_{\gamma 1 \gamma 2}}{M_{\pi^0}})^2$ variable was fitted with a Gaussian and third-degree polynomial to get the mean values for each energy bin (see Figs. 44 and 45). These mean values were fitted with the function in equation 57 to get the parameters for broader energy limits as shown in Fig. 46.

In Table 4, the parameters obtained from the second step are summarized for each sector. The effect of the correction can be seen in Fig. 47, where there is no energy dependence of the invariant mass of the photons when the photons are detected in the same sector of EC.

TABLE 4: Parameters from the second step of the correction.

Parameter	sector1	sector2	sector3	sector4	sector5	sector6
p_0	1.1775	1.2317	1.2343	1.2147	1.1860	1.1681
p_1	-0.1650	-0.1936	-0.1489	-0.1627	-0.1702	-0.1516
p_2	0.0189	0.0246	0.0110	0.0153	0.0172	0.0148
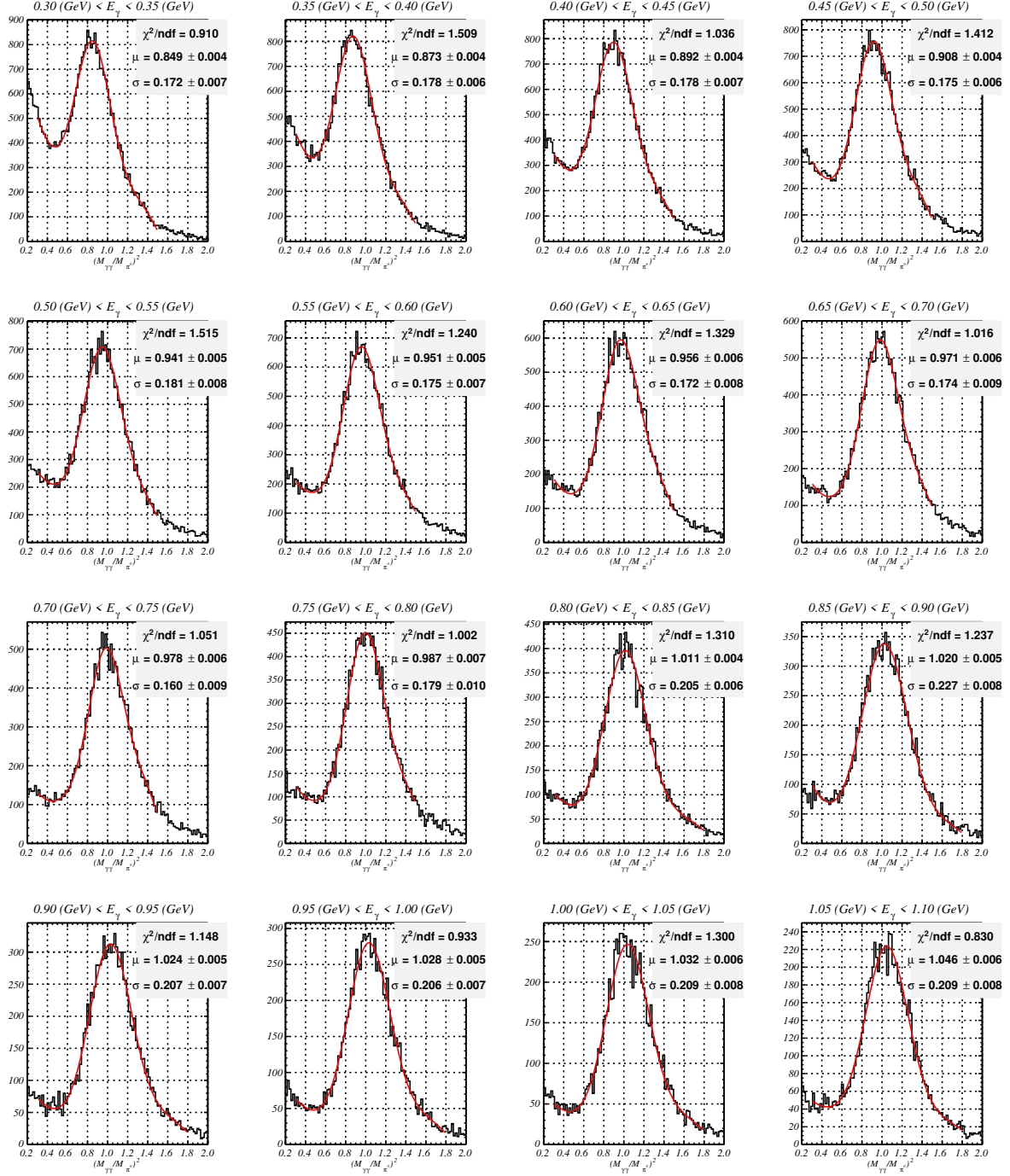
FIG. 44: Second step correction. $(M_{\gamma\gamma}/M_{\pi^0})^2$ distribution for each bin in the energy.
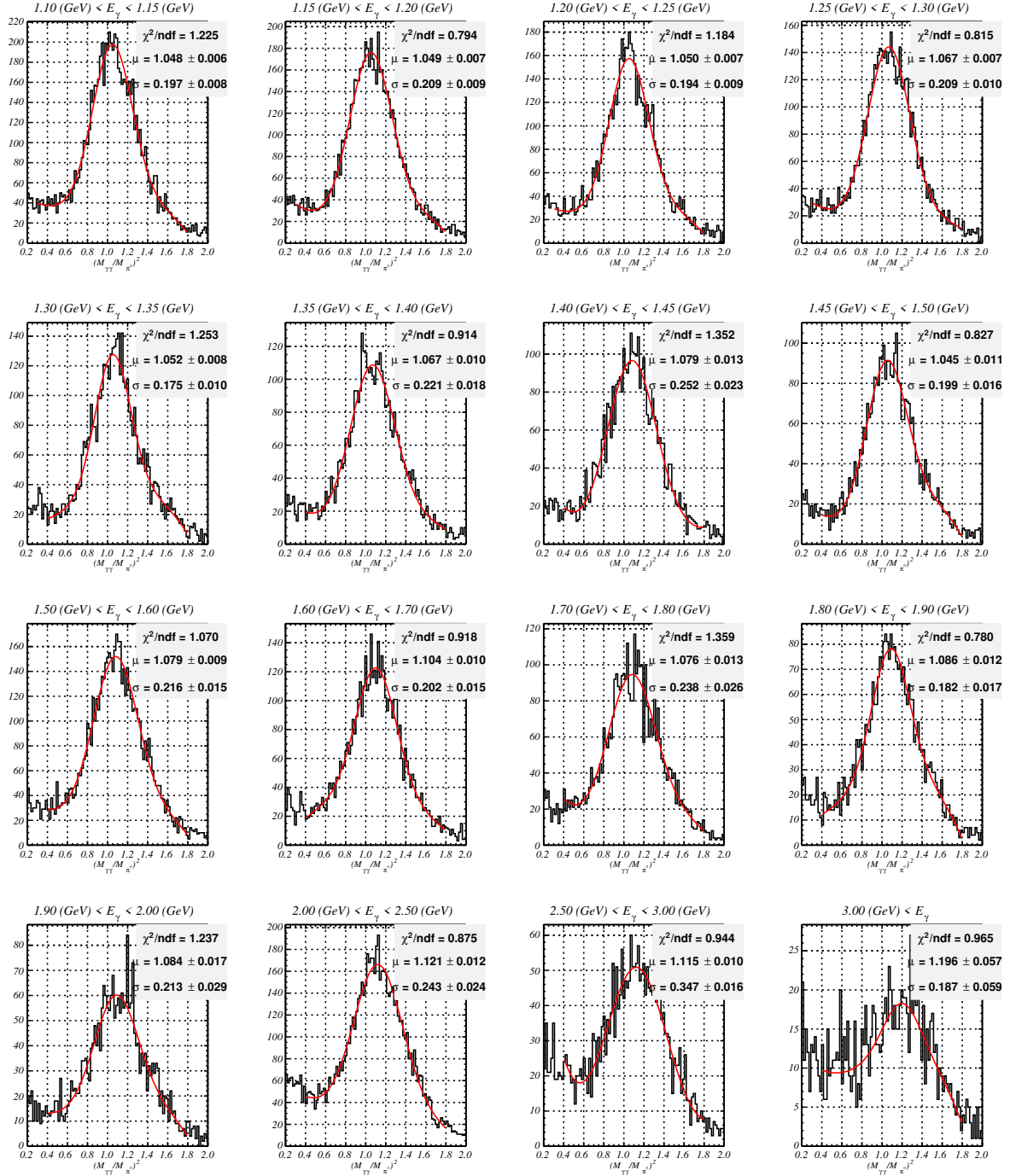
FIG. 45: Second step correction. $(M_{\gamma\gamma}/M_{\pi^0})^2$ distribution for each bin in the energy.
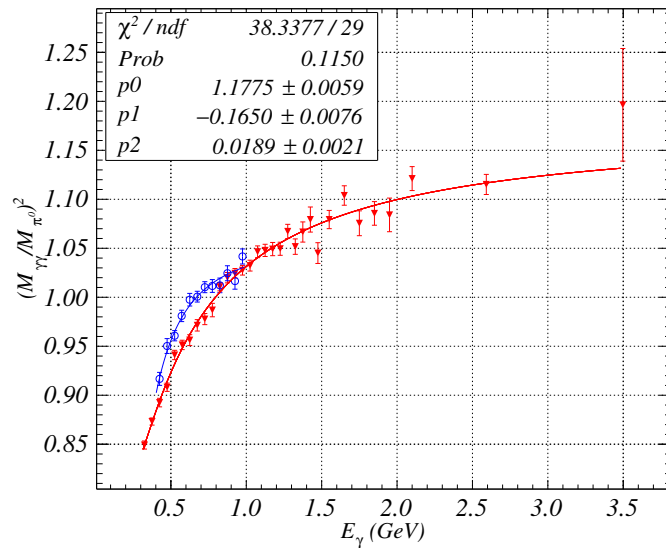
FIG. 46: $(M_{\gamma\gamma}/M_{\pi^0})^2$ as a function of the energy. The blue line correspond to the first step correction function and red line for the second one.

<center>(a)   (b)</center>
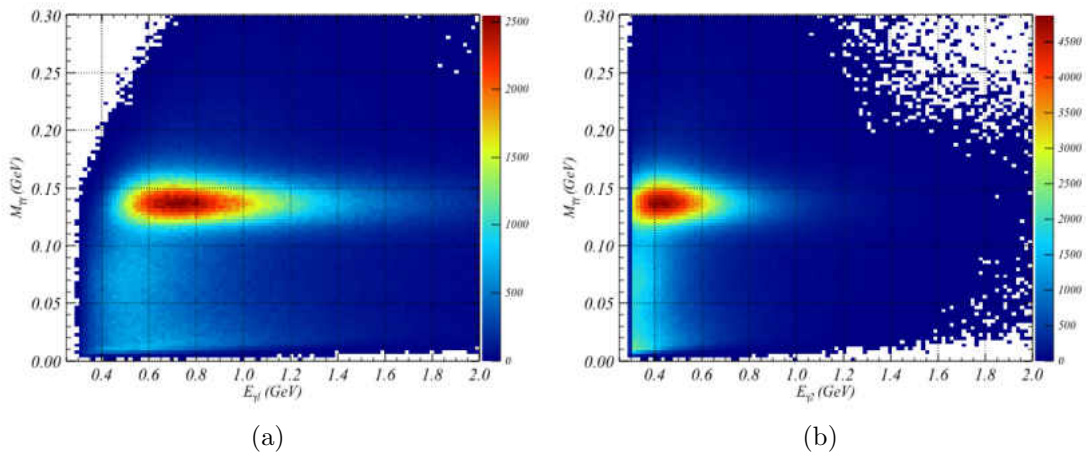
FIG. 47: Invariant mass of the two photons versus (a) first photon's energy and (b) second photon's energy after the correction.

5.6 IC PHOTON SELECTION

All hits in the IC with a minimum energy of 200 MeV are assumed to be photons. The additional cuts described below were applied in order to reduce or eliminate contributions from other particles.

1. **IC fiducial cut:** The energy and momentum of the particle is not reconstructed well when it hits the innermost or outermost parts of IC because only part of its energy is deposited. In addition, some clusters have a very high number of hits which need to be removed. Therefore, a fiducial cut was applied in order to remove these events from the data. In Fig. 48, the x, y distribution of IC before and after the fiducial cut is shown.

(a)   (b)
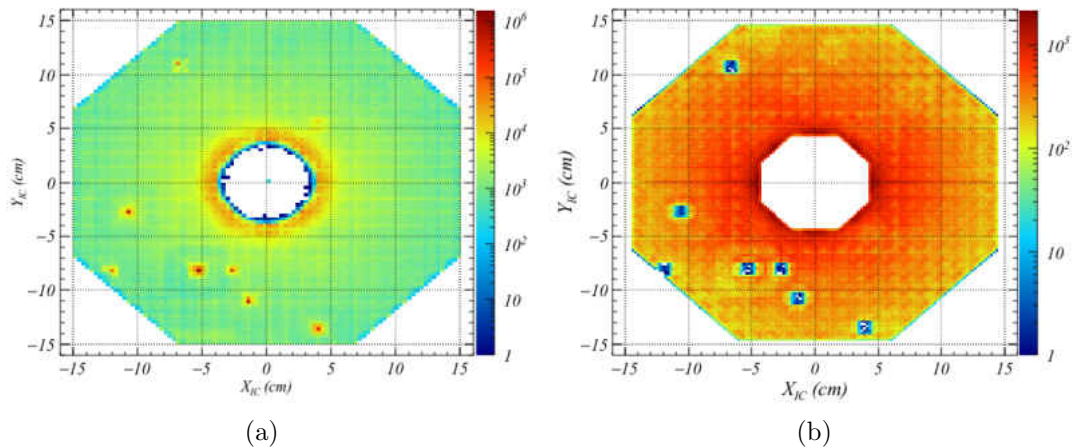
FIG. 48: y vs x hit positions on IC front face (a) before and (b) after applying octagonal fiducial cut and removing hot spots.

2. **Moller electron cut:** In Fig. 49a, the polar angle of photons in IC versus its energy is shown. One can see an overpopulated area in the low angle and low energy region. These are mostly from Moller electrons which need to be removed from the sample. The blue line in Fig. 49 shows the cut of this region.

3. **Timing cut:** Some of the hits, identified as photons, have no timing information or negative timing as shown in Fig. 49(b). These photons can contribute significantly to the background. In Fig. 50, the invariant mass of two photons versus the timing in IC was plotted. It is evident that there are no pions when the timing is negative. In order to select good photons in IC, the photon candidates with no timing or negative time

are removed from the sample. The result of this cut is illustrated in Fig. 51, where the yellow (red) area corresponds to the accepted (rejected) events.

(a)   (b)
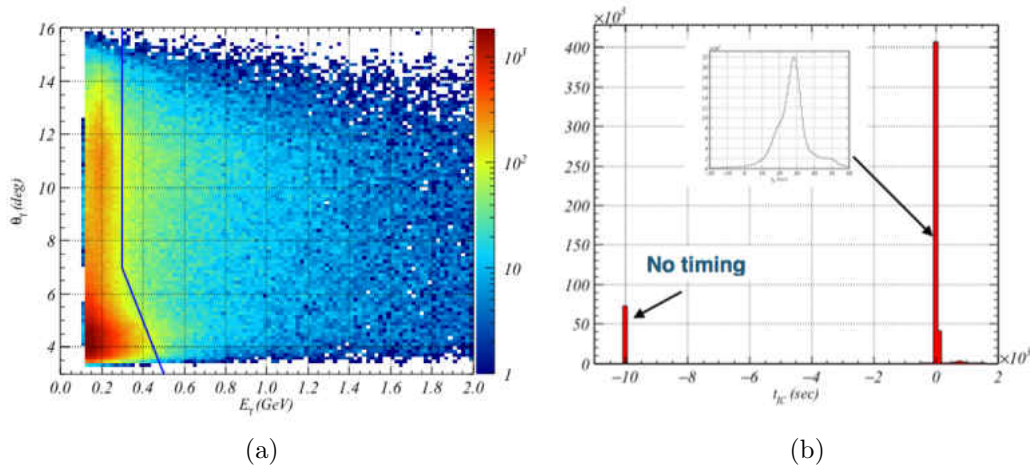
FIG. 49: (a) θ versus energy of the hits in IC. The energy dependent cut (black line) was applied to remove Moller electrons at small angle and lower energies. (b) Some event in IC have no timing information or are negative.

5.7 SIMULATION

Electroproduction of neutral pions, $e^4He \rightarrow e'^4He'\pi^0$, was simulated using the GEANT3 based CLAS simulation software package GSIM for particles detected in CLAS and the IC. The fast Monte-Carlo (fastmc) program was used for the recoiling nuclei. The steps for the simulation procedure are the following:

- **Event generator:** Generating pion electroproduction events off helium-4.

- **GSIM:** Simulation of the particle interactions in the detector and target using the geometrical representations of these.

- **GPP:** GSIM Post-Processing package (GPP) simulates detector resolutions and inefficiencies.

- **Reconstruction process:** Reconstructing tracks and hits after GPP by using REC-SIS software.

- **fast Monte-Carlo:** Simulation of the recoiling helium-4.
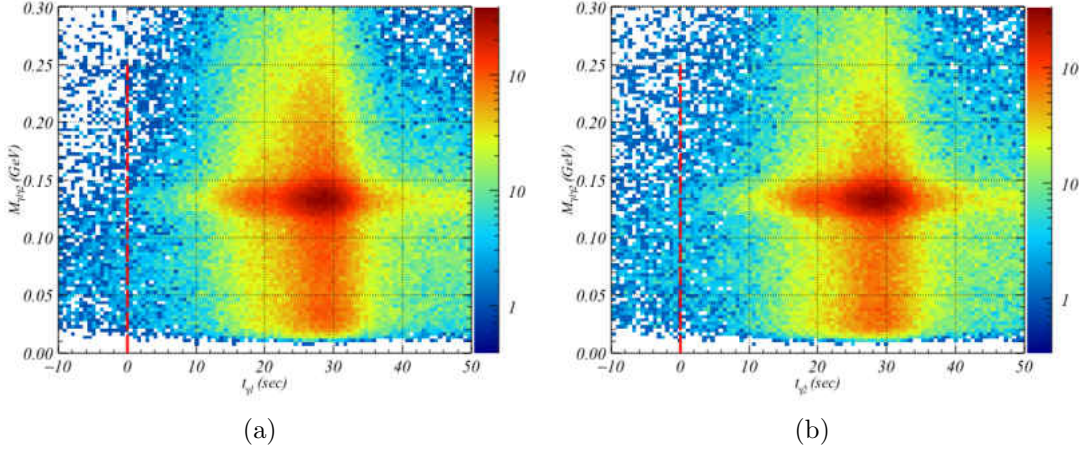
FIG. 50: Invariant mass of two photons versus (a) first and (b) second photons timing information in IC. The events on the lefts side of the vertical red line were removed.

- **Corrections:** Correcting kinematics of the particle's by comparing simulated and generated events.

After the steps above, which will be briefly discussed in the following sections, the simulated data are analyzed like the experimental data using the same detector acceptances, particle selections and exclusivity cuts.

5.7.1 EVENT GENERATOR

Events are generated for the reaction $e^4He \rightarrow e'^4He'\pi^0$ according to the cross section [43] in the kinematic regions summarized in Table 5. These kinematic regions are slightly expanded in comparison to the ones measured in the experimental data. The cross-section is parametrized as:

$$\frac{d^4\sigma}{dQ^2 dx_B dt d\phi} \propto (\frac{Q_0^2}{Q^2})^\alpha \cdot \frac{1}{(1+bt)^\beta} \cdot \frac{1}{1+(\frac{x-0.3}{c})^2} \cdot (1 - d \cdot [1 - \cos(\phi)]) \quad (59)$$

where the values of the parameters are summarized in Table 6.

5.7.2 GSIM

The generated events were then processed by using the GEANT3 based GSIM program. It simulates the detector and target geometry of the eg6 experiment, except the RTPC, which is simulated by using $fastmc$. In addition, the particle interactions with sub-detectors and
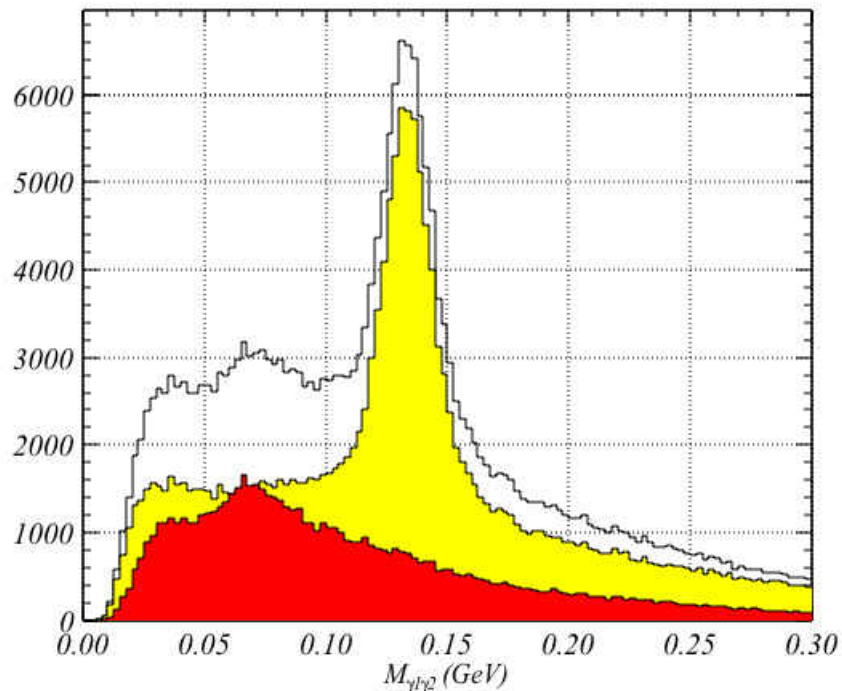
FIG. 51: Invariant mass of two photons in IC. The red area represents either of photons has no timing information or it is negative. Yellow area represent both photons have positive timing information.

material inside the CLAS detector and their responses are simulated by GSIM. All the information gathered from the interactions and responses are written in raw data format.

5.7.3 GPP

The outputs from the previous steps of the simulation are processed through GPP to include the resolutions and inefficiencies of the detectors. The resolutions in drift chambers are included by smearing DOCA's (see section 4.1) in each region in the Gaussian form. The smearing factors a, b and c correspond to region 1, region 2 and region 3, respectively. Moreover, dead wires and inefficiencies in DC results in holes which are also removed by the GPP process. In the GPP program, the IC energy is smeared according to the three parameters, ic_a, ic_b and ic_c while TOF is smeared by factor a_{TOF} only. The smearing factors in GPP are summarized in the Table 7. This step is important to make simulated data more realistic and compatible with the particle's kinematics in the experiment.

TABLE 5: Kinematic ranges.

Parameter	Q^2	$-t$	x_B	$-z$
Exp. data	$\in [0.5, 3.5]$ (GeV^2)	$\in [0.05, 0.35]$ (GeV^2)	$\in [1,2]$	$\in [-74, -54]$ (cm)
Sim. data	$\in [0.5, 3.5]$ (GeV^2)	$\in [0.05, 0.35]$ (GeV^2)	$\in [1,2]$	$\in [-74, -54]$ (cm)

TABLE 6: Parameters

Parameter	Value	Unit
Q_0^2	1.0	GeV^2
α	3.0	
b	-8.8	GeV^2
β	7.3	
c	0.3	
d	0.0	

5.7.4 RECSIS

The simulated data from the steps above are in ADC and TDC formats. These data are then processed through the RECSIS program the same way the experimental data are, converting ADC and TDC values to the corresponding energy and timing information and then reconstruct particle tracks. The data are then treated in a similar way as the experimental data to select final state particles, electron and two photons. The helium-4 selection will be discussed in the next section since the RTPC has not been implemented into GSIM, yet.

5.7.5 FASTMC

The CLAS detector package with additionally the IC and RTPC was used to detect final state particles. All sub-detectors of CLAS and the IC have been simulated using GSIM. However, tracks in the RTPC are simulated using a fast monte-Carlo method. This method smears the helium-4 kinematics according to the smearing factors obtained from the elastic scattering process [34] in Gaussian form. Then, theses tracks are processed through the same acceptance code which was used to select recoiling nuclei in the experimental data.

TABLE 7: Smearing parameters in GPP [34].

DC smearing factors	a	b	c
Values	1.1	0.85	1.1
TOF smearing factor	a_{TOF}		
Value	2.1		
IC smearing factors	ic_a	ic_b	ic_c
Values	0.008	0.036	0.024

The resolutions for RTPC track kinematics are summarized in Table 8.

TABLE 8: Smearing resolutions for RTPC track

RTPC	σ_p	σ_θ	σ_ϕ	σ_z
Left side	0.09 GeV	0.04 deg	0.02 deg	6.03 mm
Right side	0.08 GeV	0.04 deg	0.02 deg	7.40 mm

5.7.6 CORRECTIONS

After all steps above for simulation of the electroproduction of neutral pions, the kinematics of the final state particles must be checked. All reconstructed kinematics of the particles in CLAS and RTPC were in a good agreement with the generated ones. However, there are some deviations in the polar angle and energy of the photons in IC as a shown in Fig. 52.

In Fig. 53(a) (b), the ratio between the reconstructed and generated energy (polar angle) versus generated energy (polar angle) of the photons is plotted. The quantity on the x-axis was sliced and the average values on y-axis for each slice were fitted with a polynomial of third degree to get the correction functions. The parameters of the functions are summarized in Table 9. Then, the photon kinematics in IC was corrected by:

$$E_\gamma^{Corr} = \frac{E_\gamma^{Rec}}{f(E_\gamma)} \qquad \text{and} \quad \theta_\gamma^{Corr} = \frac{\theta_\gamma^{Rec}}{f(\theta_\gamma)} \tag{60}$$

In Fig. 54, the distribution of the invariant mass of two photons was plotted before and after correcting the kinematics.

TABLE 9: Parameters of the correction parameters.

Parameters	a	b	c	d
Energy	1.066	0.008	-0.011	0.002
Polar angle	0.952	0.020	-0.002	0.001

(a) (b) (c) (d) (e) (f)
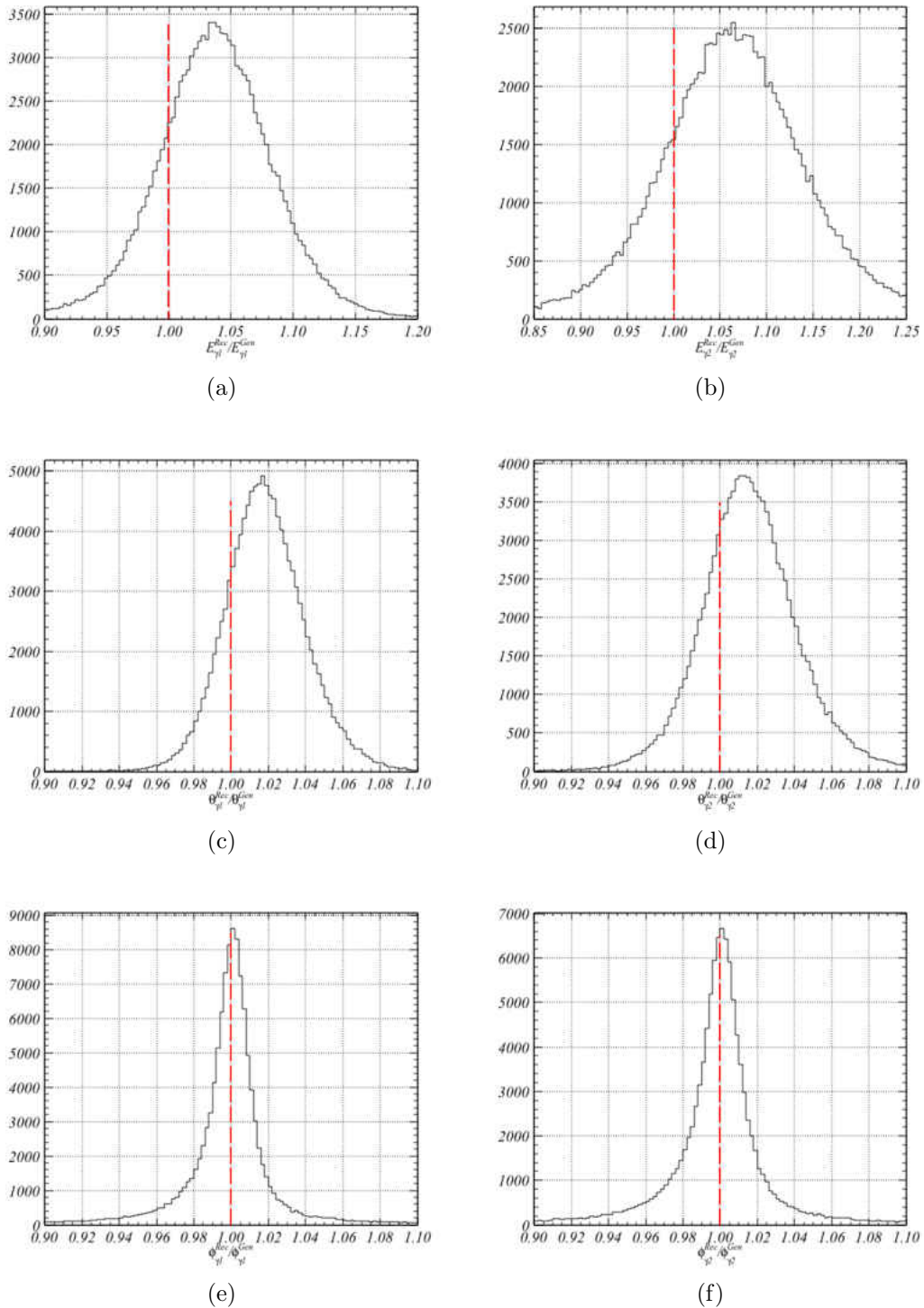
FIG. 52: Comparing the reconstructed kinematics of photons with generated ones. There is a shift in energy and polar angle of photons which can be due to the badly geometry of the IC implemented to GSIM.

(a)   (b)
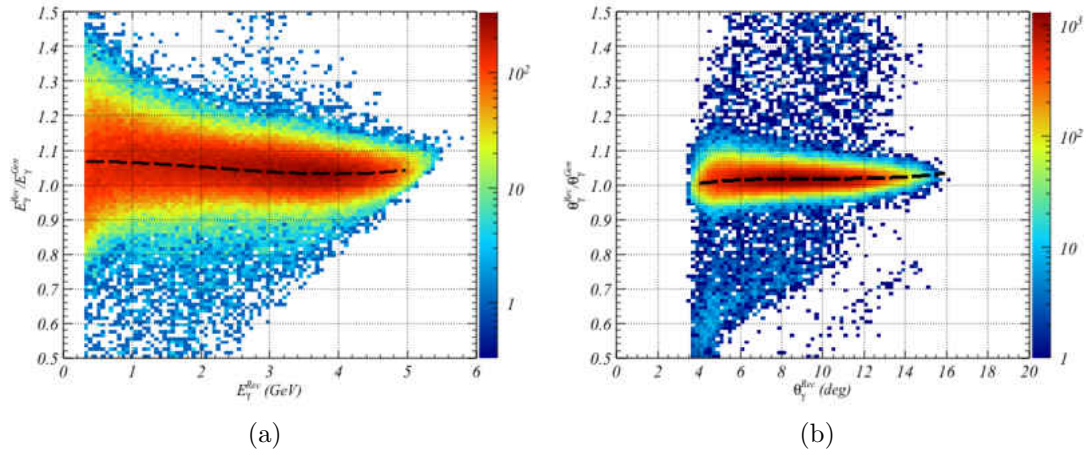
FIG. 53: The ratio of reconstructed to generated (a) energies and (b) polar angles is plotted as a function of reconstructed ones. The mean values of the distribution is fitted with polynomial of third degree to get correction function which is represented by black line.

(a)   (b)
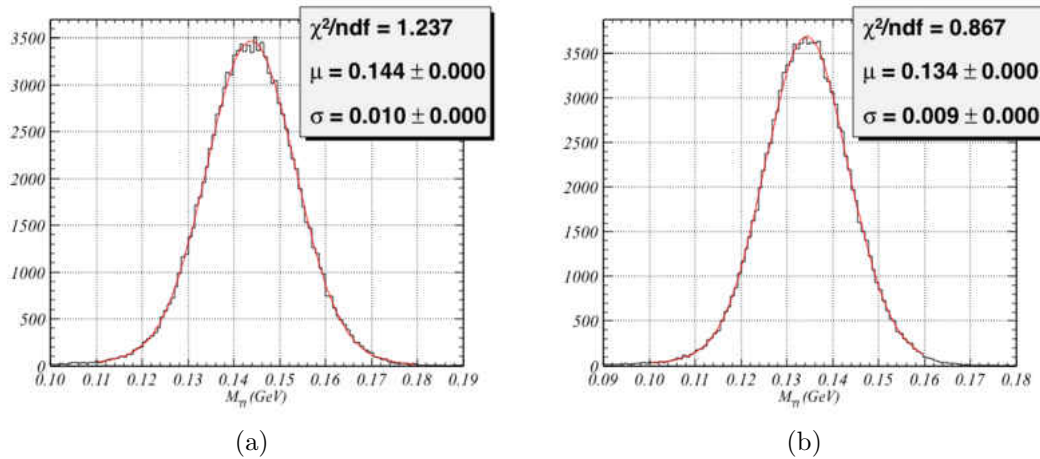
FIG. 54: Invariant Mass of the reconstructed photons (a) before and (b) after the correction.

CHAPTER 6

EXCLUSIVE ELECTROPRODUCTION OF NEUTRAL PIONS

In this chapter, we will describe the procedure for selecting exclusive events after identifying the final state particles for coherent electroproduction of the π^0. These events contain one good electron, one good helium and at least two photons with each a minimum energy of 200 MeV. Samples which have more than two photons were not rejected since some of these photons can be accidentals which will result in removing good events too.

The π^0 decays into two photons which each can be detected in the EC or IC which results in three different combination to reconstruct:

- **EC-EC:** both photons are detected in EC

- **EC-IC:** one photon is detected in EC and the other one in IC

- **IC-IC:** both photons are detected in IC

In the following sections, definitions of exclusive variables and generated cuts will be discussed.

6.1 DEFINITION OF EXCLUSIVE VARIABLES

The process to describe coherent electroproduction of π^0 is:

$$P(e) + P(^4He) \rightarrow P(e') + P(^4He') + P(\pi^0) \tag{61}$$

where $P(particle)$ is the four-vector momentum of the *particle* in the lab frame. The four-vector momentum of the π^0 is calculated from the variables of the photons:

$$P(\pi^0) = ((p_x^{\gamma_1} + p_x^{\gamma_2}), (p_y^{\gamma_1} + p_y^{\gamma_2}), (p_z^{\gamma_1} + p_z^{\gamma_2}), \sqrt{(p^{\gamma_1} + p^{\gamma_2})^2 + M_{\pi^0}^2}) \tag{62}$$

where $p_j^{\gamma_i}$ is the measured energy of photon (i) in the direction (j) and M_{π^0} is the Particle Data Group (PDG) [40] mass of the neutral pion.

There are additional four-vectors generated from the four-vectors above:

$$P_{\gamma^*} = P(e) - P(e') \tag{63}$$

$$P_X^{e'^4He'\pi^0} = P(e) + P(^4He) - P(e') - P(^4He') - P(\pi^0) \tag{64}$$

$$P_X^{e'\pi^0} = P(e) + P(^4He) - P(e') - P(\pi^0) \tag{65}$$

$$P_X^{e'^4He'} = P(e) + P(^4He) - P(e') - P(^4He') \tag{66}$$

Using the equations above, one can calculate **exclusive variables** as following:

- **Definition of missing mass squares:**

$$MM_X^2(e'^4He'\pi^0) = (P_X^{e'^4He'\pi^0})^2 \tag{67}$$

$$MM_X^2(e'\pi^0) = (P_X^{e'\pi^0})^2 \tag{68}$$

$$MM_X^2(e'^4He') = (P_X^{e'^4He'})^2 \tag{69}$$

- **Coplanarity anlge:** In exclusive π^0 production, the virtual photon, recoil helium-4 and π^0 are coplanar. In other words, they lie on the same plane. The normal vector of this plane can be calculated in three different ways as following:

$$\vec{H}_1 = \vec{P}_{^4He'} \times \vec{P}_{\gamma^*} \tag{70}$$

$$\vec{H}_2 = \vec{P}_{^4He'} \times \vec{P}_{\pi^0} \tag{71}$$

$$\vec{H}_3 = \vec{P}_{\gamma^*} \times \vec{P}_{\pi^0} \tag{72}$$

where the $\vec{P}_{^4He'}$, $\vec{P}_{\pi^0}$ and $\vec{P}_{\gamma^*}$ are momentum of the recoil nuclei, pion and virtual photon, respectively. The coplanarity angle $\Delta\phi$ is defined as the angle between normal vectors in the Eqns (70), (71) and (72). The most narrow $\Delta\phi$ was obtained between $(\vec{H}_1, \vec{H}_3)$ vectors, which was used.

- **Cone angle:** The angle between the detected π^0 and reconstructed one from $P_X^{e'^4He'}$ is called cone angle and it is calculated as:

$$\Delta\theta(\pi^0, e'^4He') = \cos^{-1}\left(\frac{\vec{P}_{\pi^0} \cdot \vec{P_X^{e'^4He'}}}{|\vec{P}_{\pi^0}||\vec{P_X^{e'^4He'}}|}\right) \tag{73}$$

- **Missing energy and momenta:** The components of $P_X^{e'^4He'\pi^0}$ are missing energy and momenta in (x, y, z) direction.

FIG. 55: Invariant mass of two photons detected by EC. The histogram has been fitted with Gaussian function (green line) and polynomial (dashed blue line). The red line indicates total fit function. Vertical dashed red lines corresponds to the cut positions: 0.084 GeV $< M_{\gamma\gamma} <$0.186 GeV.

6.2 EC-EC COMBINATION

In this section of the analysis, we require that there are at least two photons in the EC. The invariant mass of these photons is calculated via

$$M_{\gamma\gamma} = 2 * \sqrt{E_{\gamma 1} * E_{\gamma 2}} * sin^2(\frac{\theta_{\gamma\gamma}}{2}) \tag{74}$$

where $E_{\gamma 1}$ and $E_{\gamma 2}$ are the energies deposited in EC by photons. $\theta_{\gamma\gamma}$ is the opening angle between the two photons. The invariant mass distribution of photons is shown in Fig.55. This distribution has been fitted with a Gaussian function (π^0 peak) plus a polynomial (background) and then a $\pm 3\sigma$ cut was applied around the mean value to select neutral pions. The next histogram in Fig. 56 is the missing mass square $MM_X^2(e'^4He'\pi^0)$ after selecting pions. One can easily decide that there is no evidence for coherent production of π^0 when photons were detected by EC since there is no signal (enhancement) at 0.

6.3 EC-IC COMBINATION

A similar procedure was followed for the **EC-IC** combination. The invariant mass of two
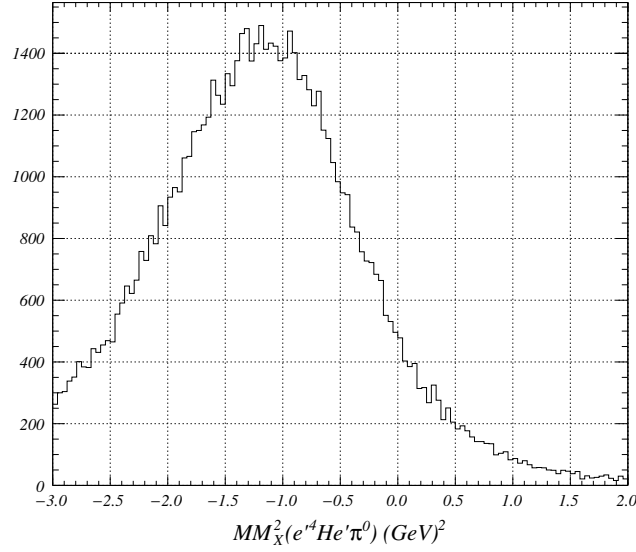
FIG. 56: Missing mass $MM_X^2(e'^4He'\pi^0)$ spectrum for EC-EC combination.

photons, one in EC and one in IC, is calculated via equation (74). Neutral pions were selected by applying a $\pm 3\sigma$ cut around the mean value after fitting with a Gaussian and polynomial functions as illustrated in Fig. 57. The missing mass spectrum after pion selection is shown in Fig. 58, where there is no evidence for the exclusive reaction of interest either.

6.4 IC-IC COMBINATION

The last combination of photons to reconstruct π is when both of them are detected in IC. The invariant mass of these photons is presented in Fig. 59. This histogram has been fitted with a Gaussian distribution to determine the width and mean of the peak, plus third order polynomial which represents background. The cut was placed on $M_{\gamma\gamma}$ around the mean value to select π^0. After the selection of final state particles (electron, helium-4 and π^0), there is a peak around zero on the exclusive missing mass variable ($MM_X^2(e'^4He'\pi^0)$) as illustrated in Fig. 60, which can be the coherent reaction of interest. The following cuts were applied to select a clean channel of coherent production of π^0 :

1. **Pion momentum cut:** The missing mass distribution in Fig.60 has a lot of background. The 2-dimensional histogram of $MM_X^2(e'^4He'\pi^0)$ vs P_{π^0} was plotted as shown in the Fig. 61. All events with pion momentum less than 3 GeV were rejected in order to suppress background.
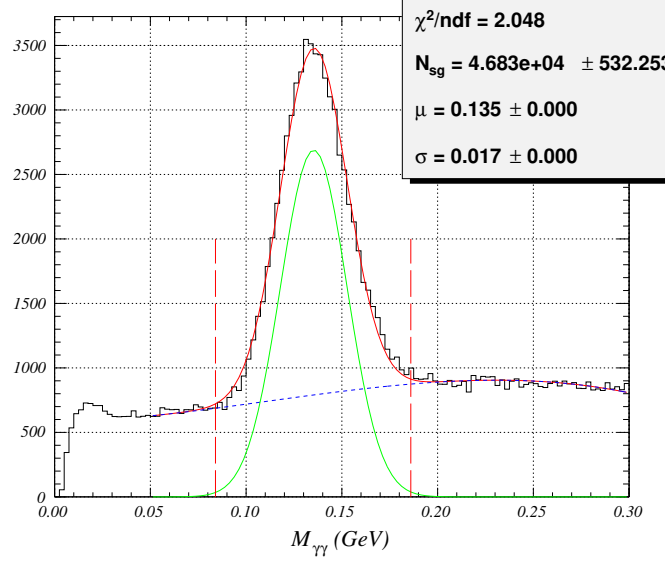
FIG. 57: Invariant mass of photons detected by EC and IC. The histogram has been fitted with Gaussian function (green line) and polynomial (dashed blue line). The red line indicates total fit function. Vertical dashed red lines corresponds to the cut positions: 0.099 GeV $< M_{\gamma\gamma} < 0.177$ GeV

2. **Missing mass square:** The missing mass spectrum of $MM_X^2(e'^4He'\pi^0)$ exclusive variable has been fitted with a Gaussian function and a polynomial as illustrated in Fig. 62 to obtain the width of the peak after the pion momentum cut. To get the exclusive events of interest, a $\pm 3\sigma$ cut was applied inidicated by the vertical dashed red lines.

3. **Coplanarity angle cut:** In coherent electroproduction of π^0 events, the $\Delta\phi$ angle between the plane of the virtual photon and the π^0 and the plane of the virtual photon and the recoil helium-4 must peak around zero since these particles are coplanar. If the events have additional particles, then the π^0 may not be in the same plane with the virtual photon and recoil target which means $\Delta\phi$ does not need to be zero. The $\Delta\phi$ angle distribution is illustrated in Fig.63 after the cuts above which has been fitted with Gaussian function and polynomial. The events which are inside of $\pm 3\sigma$ are considered to be exclusive events. Vertical dashed red lines show where the cuts were applied.

4. **Cone angle cut:** The direction of the $\pi0$ can be reconstructed from four-vectors of initial and final electron and helium-4. In principle, the angle between reconstructed
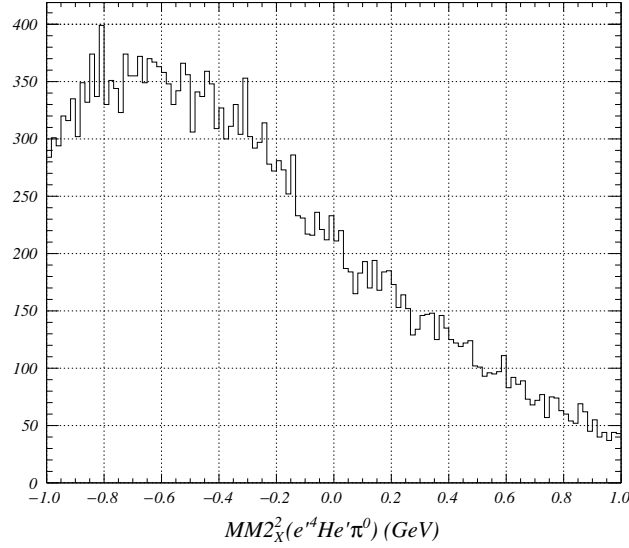
FIG. 58: Missing mass $MM_X^2(e'^4He'\pi^0)$ spectrum for EC-IC combination.

pion and detected one by IC should be zero. However, if there are additional produced particles, the cone angle does not need to be close to zero. The $\Delta\theta(\pi^0, e'^4He')$ angle distribution is shown in Fig.63 after the cuts (1), (2) and (3) above. All events where the cone angle is smaller than 2.5 degree were accepted to be coherent reactions of interest. The vertical red line shows where the the cut was applied.

5. **Missing mass square of helium-4:** After all exclusive cuts above, the missing mass distribution of helium-4 calculated using equation 68 is shown in Fig.65. This distribution has been fitted with Gaussian function plus polynomial to determine the width and a $\pm 3\sigma$ cut applied: $|MM_X^2(e'\pi^0) - \mu| < 3\sigma$. The vertical red lines show the cut boundary.
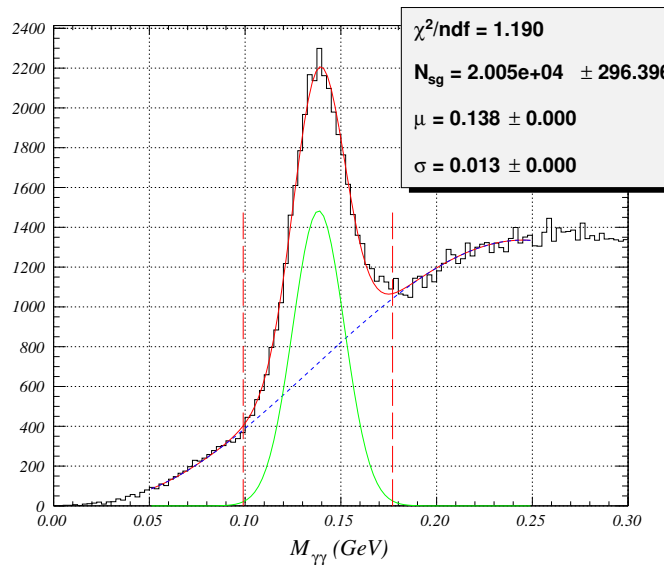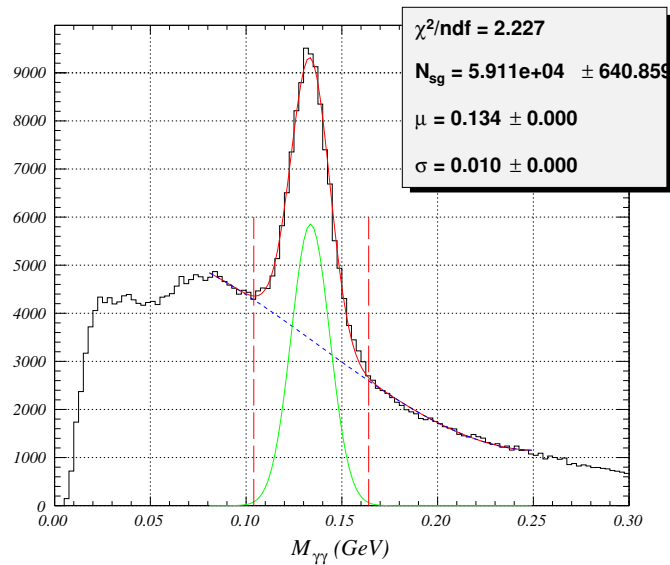
FIG. 59: Invariant mass of photons detected by IC. The histogram has been fitted with Gaussian function (green line) and polynomial (dashed blue line). The red line indicates total fit function. Vertical dashed red lines corresponds to the cut positions: 0.104 GeV $< M_{\gamma\gamma} < 0.164$ GeV
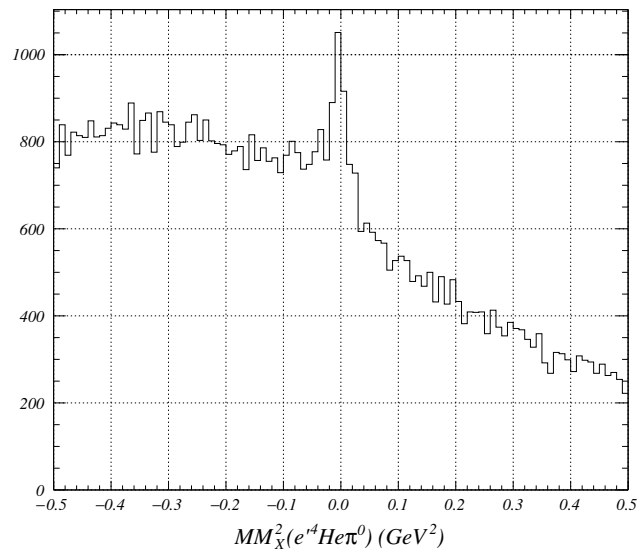
FIG. 60: Missing mass $MM_X^2(e'^4He'\pi^0)$ spectrum for IC-IC combination.
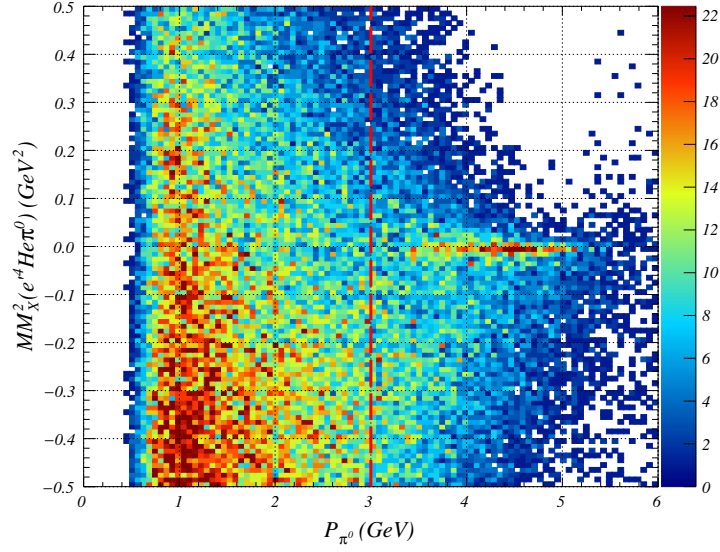
FIG. 61: $MM_X^2(e'^4He'\pi^0)$ vs P_{π^0} for IC-IC combination where vertical-dashed red line represents the cut: $P_{\pi^0} > 3.0$ GeV.
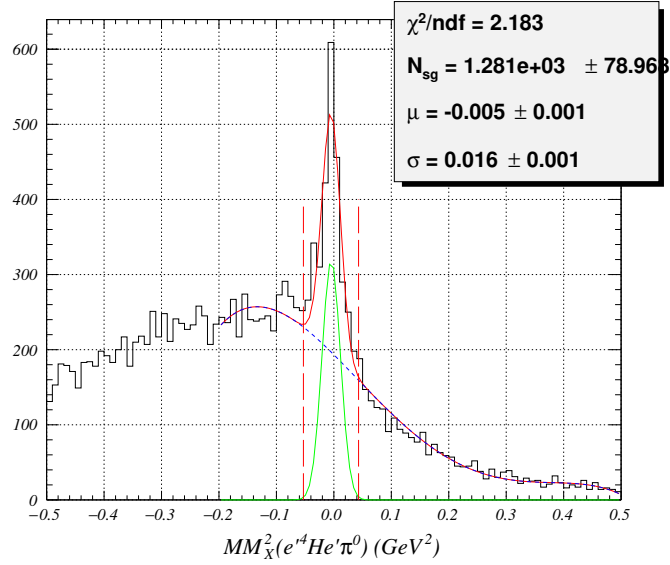
FIG. 62: $MM_X^2(e'^4He'\pi^0)$ spectrum for IC-IC combination, fitted with Gaussian function (green line)and polynomial (dashed-blue line). The red line indicates total fit function. The vertical dashed-red lines represent $\pm 3\sigma$ cut: -0.043 GeV^2 < $MM_X^2(e'^4He'\pi^0)$ <0.053 GeV^2.
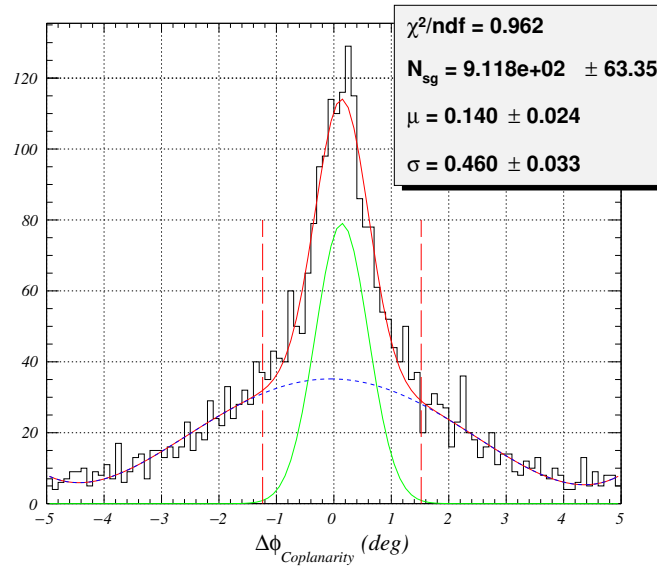
FIG. 63: The $\Delta\phi$ coplanarity angle distribution which has been fitted with Gaussian function (green line) and polynomial (dashed-blue line). The curved red line indicates total fit function and dashed-vertical lines represent cuts around mean value: $-1.24° < \Delta\phi < 1.52°$.
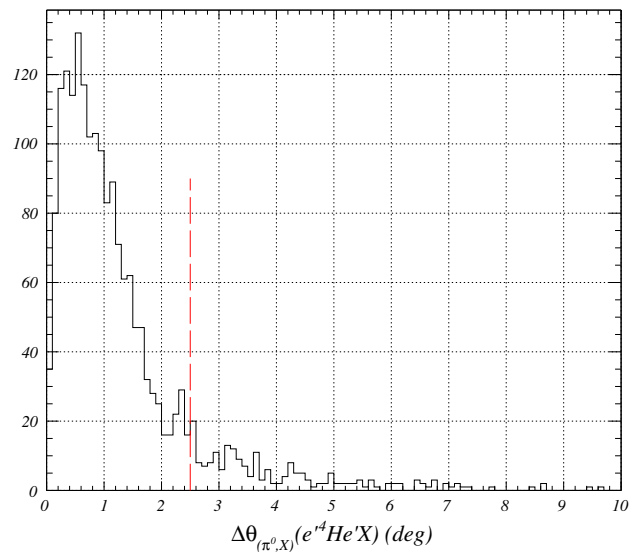
FIG. 64: Cone angle $\Delta\theta(\pi^0, e'^4He')$ distribution for IC-IC case. The dashed-vertical line indicates cut value: $\Delta\theta(\pi^0, e'^4He') < 2.5°$
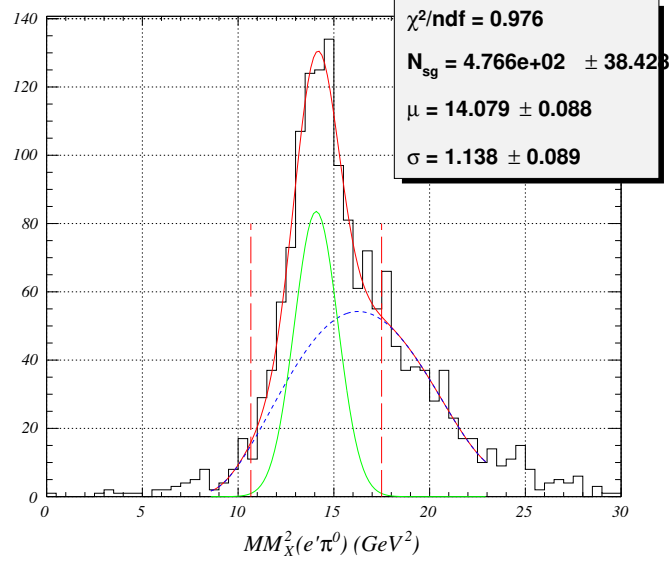
FIG. 65: $MM_X^2(e'\pi^0)$ spectrum for IC-IC combination, fitted with Gaussian function (green line)and polynomial (dashed-blue line). The red line indicates total fit function. The vertical dashed-red lines represent $\pm 3\sigma$ cut: $10.665 \text{ GeV}^2 < MM_X^2(e'\pi^0) < 17.493 \text{ GeV}^2$.
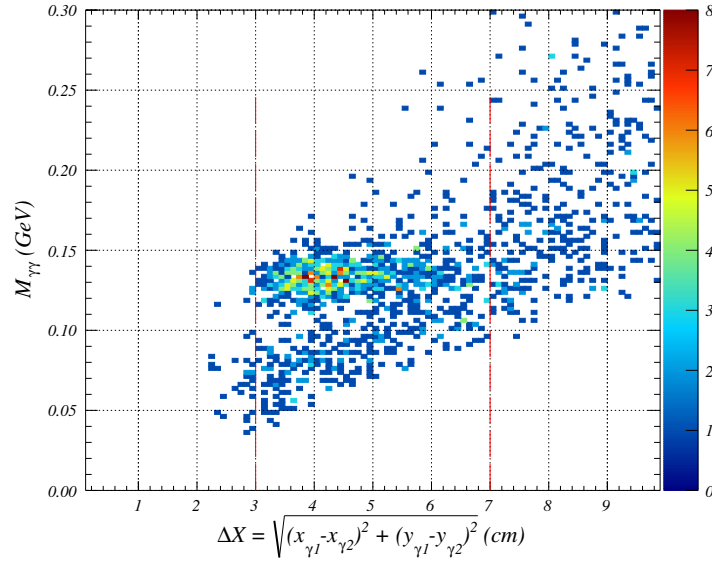
FIG. 66: Invariant mass of photons $M_{\gamma\gamma}$ vs the distance between them on the IC face ΔX. The dashed-vertical red lines indicate cut: $3.0 \text{ cm} < \Delta x < 7.0 \text{ cm}$.
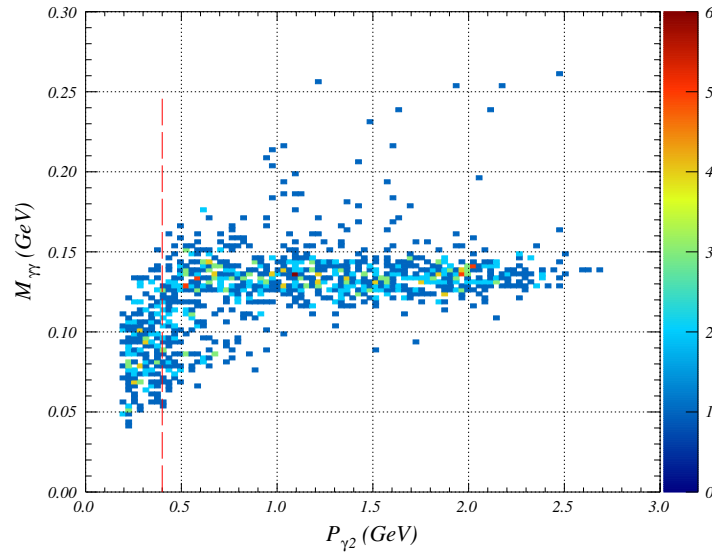
FIG. 67: Invariant mass of two photons $M_{\gamma\gamma}$ vs momentum of slower photons $P_{\gamma 2}$ distribution, where dashed-vertical red line represents minimum momentum of photon: $P_{\gamma 2} > 0.4$ GeV.
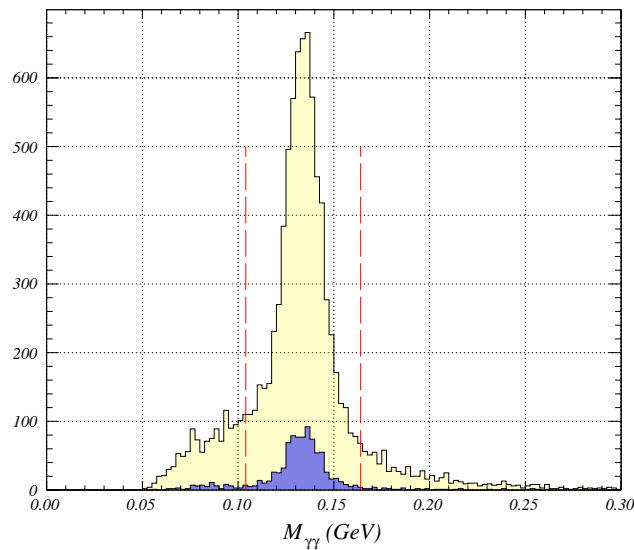
FIG. 68: The distribution of invariant mass of two photons. Yellow area represents events with one electron, one helium and at least two photons after applying cuts (1) and (6). Blue region corresponds to the events which pass all cuts. The vertical-dashed red lines indicate $\pm 3\sigma$ cut.

6. **Background suppression:** There might still be a non-negligible background after applying exclusivity cuts. In order to reduce the background further, the following cuts were applied on photons detected in IC:

   (a) **Distance between the photons on IC:** To suppress the background, invariant mass of two photons $M_{\gamma\gamma}$ vs distance Δx of them on the IC face was plotted and is shown in Fig.66. The Δx distance was chosen between 3 cm and 7 cm which is represented by vertical red lines.

   (b) **Momentum cut of slower photon:** Fig.67 shows invariant mass of photons vs momentum of the slower photon. All events with photon momentum smaller than 400 MeV were rejected which corresponds to the vertical dashed red line.

The results of the cuts described above are summarized in Figure 68 and Figure 69. In these histograms, the yellow region corresponds to electron, helium-4 and pion final state events after cuts (1) and (6). The blue shaded area represents events after all the cuts except the variable that was plotted on the histogram. In Table 10, a summary of all cuts for accepted coherent electroproduction of π^0 events are listed.

TABLE 10: Summary of cuts for variables for good coherent events.

cut	variable	value	units
1	P_{π^0}	> 3.00	(GeV)
2	$|MM_X^2(e'^4He'\pi^0) - 0.005|$	< 0.048	(GeV^2)
3	$|\Delta\phi_{Coplanarity} - 0.16|$	< 1.38	(deg)
4	$\Delta\theta_{\pi^0,X}(e'^4He'X)$	< 2.50	(deg)
5	$|MM_X^2(e'\pi^0) - 14.079|$	< 3.414	(GeV^2)
6-a	ΔX	$\in [3.0, 7.0]$	(cm)
6-b	$P_{\gamma 2}$	> 0.400	(GeV)
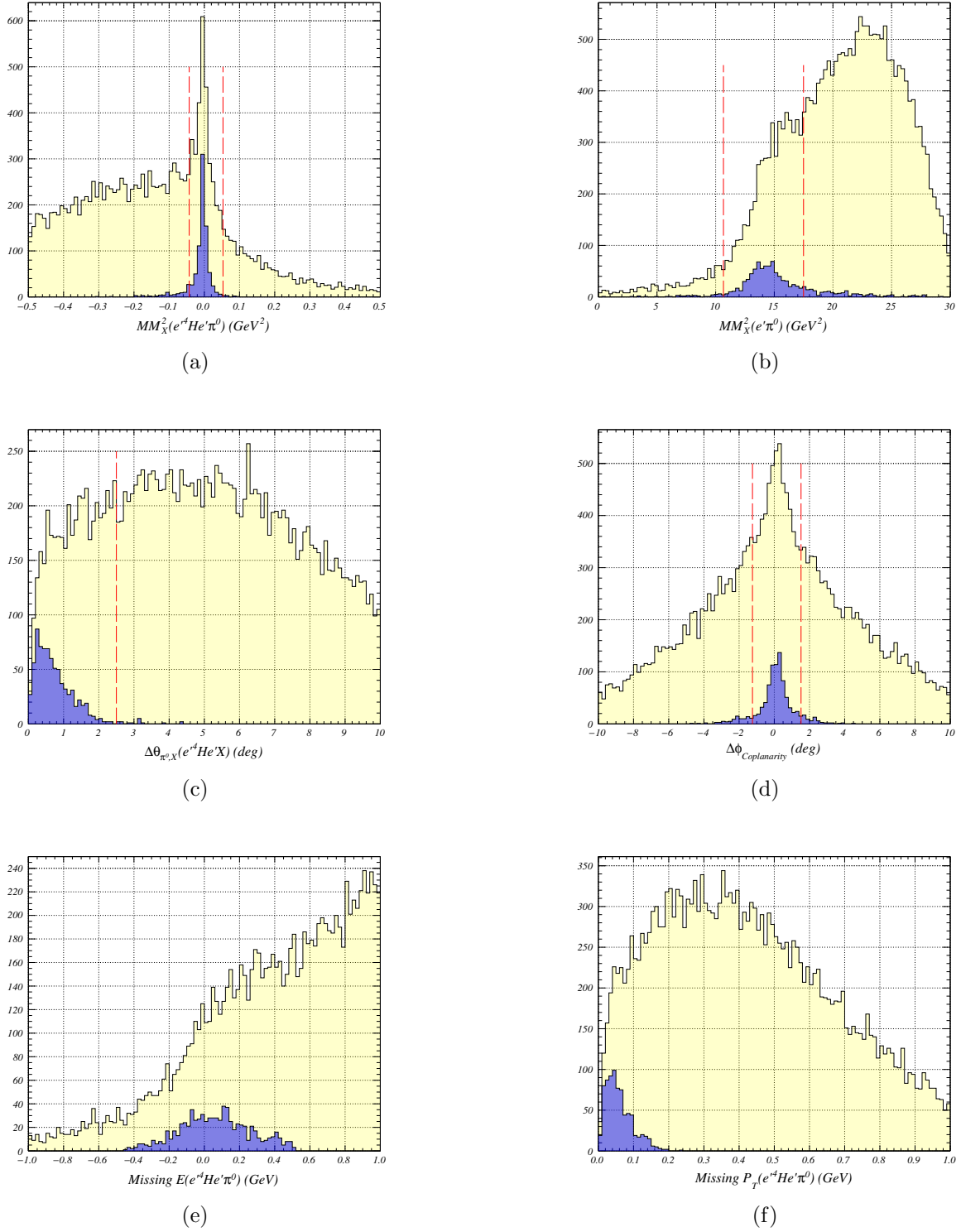
FIG. 69: The distribution of exclusive cuts. Yellow area represents events with one electron, one helium and pion after applying cuts (1) and (6). Blue region corresponds to the events which pass all cuts except the quantity that was plotted. The vertical red lines indicate cuts that were used to select coherent events.

6.5 COMPARING EXPERIMENTAL RESULTS WITH SIMULATION

The simulated events were produced using the methods that were described in section 5.7. Then, these events were processed through the same analysis code as the experimental data. To compare the results, simulated events were scaled to experimental data as shown in Fig. 70, Fig. 71 and Fig. 72.
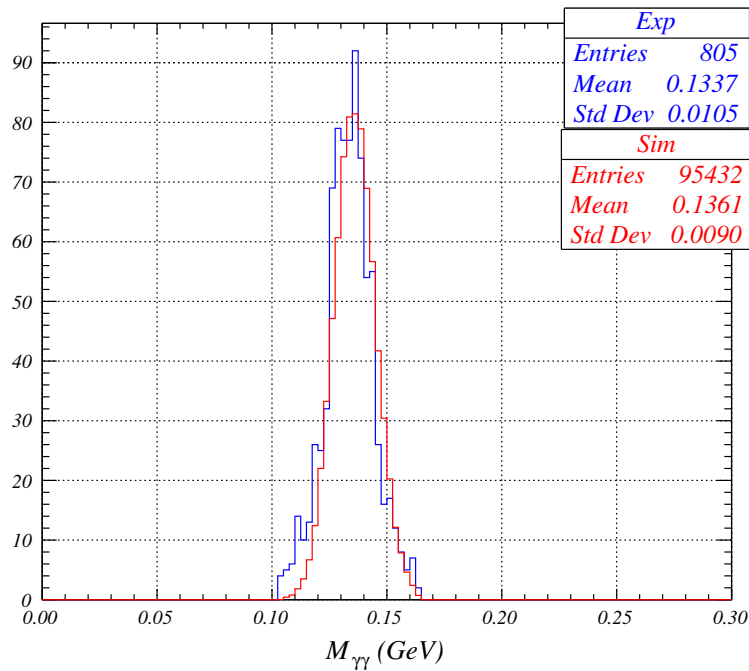
FIG. 70: Comparison of simulated data to the experimental data for the invariant mass of two photons after all particle identification and event selection cuts. The blue line corresponds to the experimental data while the red one corresponds to the simulation data.
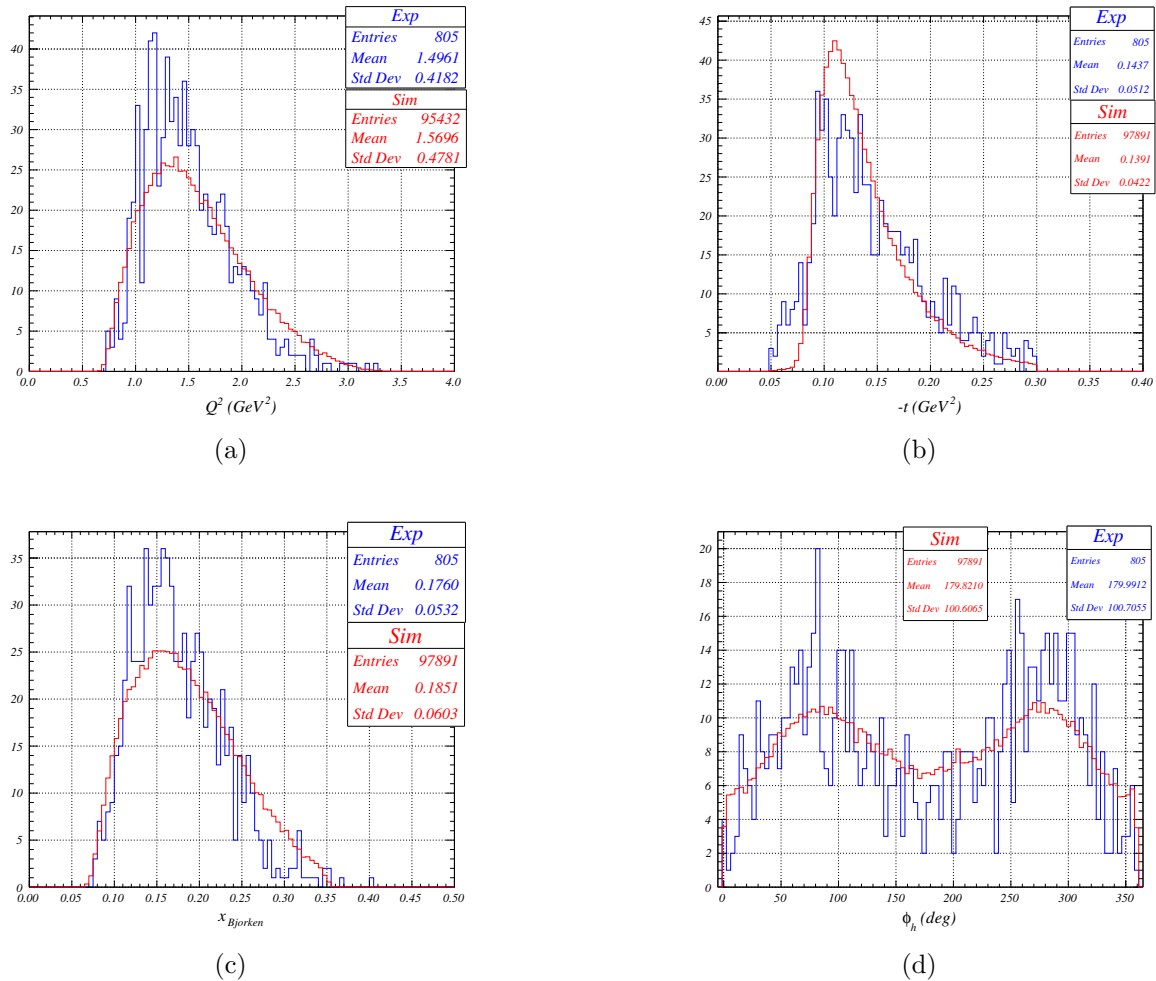
FIG. 71: Comparison between simulated data and experimental data for kinematic variables, Q^2, $-t$, x_B and ϕ_h after all particle identification and event selection cuts. The blue line corresponds to the experimental data while the red one corresponds to the simulation data.
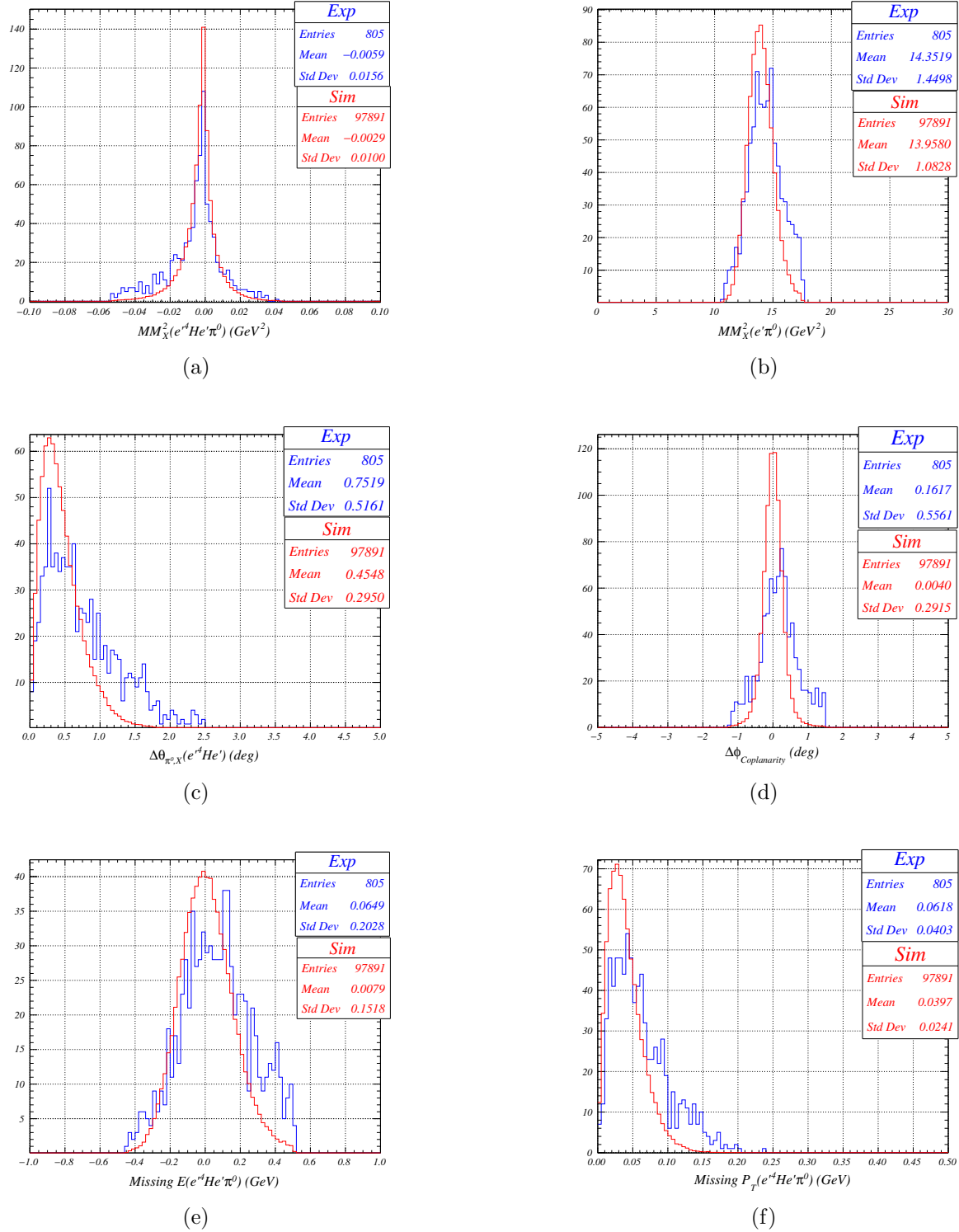
FIG. 72: Comparison of simulated data to experimental data for exclusive variables after all particle identification and event selection cuts. The histograms correspond to: (a) missing mass square of $(e'^4he'\pi^0)$, (b)missing mass square of $(e'\pi^0)$, (c) Cone-Angle matching, (d) Coplanarity, (e) missing energy and (f) missing tranverse momentum. The blue lines correspond to the experimental data while the red ones correspond to the simulation data.

6.6 EVENT NUMBERS AND BINNING

The list of event numbers is summarized in Table 11 for each event selection cut described above.

TABLE 11: Number of events left after event selection cuts.

cut	variable	event number
1	P_{π^0}	23073
2	$MM_X^2(e'^4He'\pi^0)$	3283
3	$MM_X^2(e'\pi^0)$	1871
4	$\Delta\phi_{Coplanarity}$	1662
5	$\Delta\theta_{\pi^0,X}$	1110
6-a	ΔX	903
6-b	$P_{\gamma 2}$	805

CHAPTER 7

EXTRACTION OF BEAM-SPIN ASYMMETRY

In this chapter, the extraction of the beam-spin asymmetry and the method of error estimation (statistical and systematic) of the coherent electroproduction of π^0 will be discussed.

7.1 STATISTICAL UNCERTAINTIES

The beam-spin asymmetry is extracted from the number of events in each helicity state as following:

$$A_{LU} = \frac{\sigma^+ - \sigma^-}{\sigma^+ + \sigma^-} = \frac{1}{P_B} \frac{N^+ - N^-}{N^+ + N^-} \tag{75}$$

where P_B is the beam polarization, $N^+(N^-)$ is the number of events in positive (negative) beam helicity state normalized to Faraday Cup. The events have been divided into eight equal bins in ϕ. The average ϕ of the each bin was calculated as:

$$\phi = \frac{\sum_i^{events} \phi_i}{N_i} \tag{76}$$

From the equation (75) above, the statistical uncertainties are calculated as:

$$\Delta A_{LU} = \frac{2}{P_B} \frac{\sqrt{(N^- \Delta N^+)^2 + (N^+ \Delta N^-)^2}}{(N^+ + N^-)^2} \tag{77}$$

where $\Delta N^\pm$ is estimated as $\sqrt{N^\pm}$. The beam-spin asymmetry has been extracted by fitting the asymmetry for each ϕ bin with the function $\alpha \sin(\phi)$ as illustrated in Fig. 73. The function has been obtained from Eqn. (41) where γ and β terms were neglected. The extracted asymmetry is equal to $\alpha = -0.089$ with statistical uncertainty $\Delta\alpha^{Stat} = \pm 0.053$.

The variation of beam polarization during the run period is assumed to have no effect on statistical uncertainties and its contribution on systematic uncertainties will be discussed later.

7.2 SYSTEMATIC UNCERTAINTIES

The beam-spin asymmetry is the ratio of the difference of opposite helicity states to sum of them. The variables that are directly proportional to the cross-section cancel each
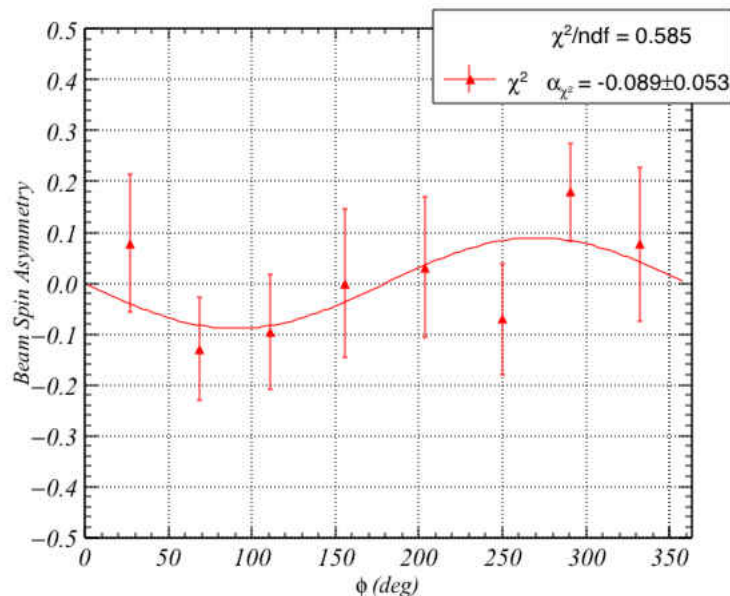
FIG. 73: Extracted beam-spin asymmetry for coherent π^0 electroproduction.

other while measuring the asymmetry. However, there are still some sources that effect the asymmetry such as beam polarization and exclusivity cuts. For estimating systematic uncertainty, the following sources were checked:

- **The variation of event selection cuts:** One of the main sources for systematic uncertainty is the value of the coherent π^0 selection cuts since these cuts directly effect the number of events. Therefore, to estimate the uncertainty, one needs to vary the value of the cuts and measure the asymmetry. The largest difference between asymmetries for different cuts and the nominal value of the asymmetry was accounted for as a systematic uncertainty.

- **The fitting method:** The asymmetry was measured by binning the data in ϕ angle and fitting with the function $\alpha \sin(\phi)$. Due to very low statistics, the value of the asymmetry is very sensitive to the binning. Therefore, the dataset was also fitted via the un-binned likelihood method which will be explained later in this chapter. The differences of the asymmetries from different fitting methods was taken as systematic uncertainty.

- **Beam polarization:** The statistical uncertainty of the beam polarization was taken

as a systematic uncertainty.

7.2.1 SYSTEMATIC UNCERTAINTY FROM VARIATION OF MISSING MASS SQUARED $MM_X^2(e'\pi^{0'})$ CUT

In order to estimate the systematic uncertainty associated with the exclusivity variable, one needs to change the cut value of the variable and calculate asymmetry again. The distribution of $MM_X^2(e'\pi'^0)$ is shown in the Fig. 74. The dashed-vertical lines correspond to the different cuts on the exclusivity variable. For each cut, the data were binned in ϕ angle and fitted with $\alpha \sin(\phi)$ function to extract the α value as illustrated in Fig. 75. The summary of the extracted asymmetries from a variation of the $MM_X^2(e'\pi^0)$ variable is shown in Table 12. The maximum deviation of the asymmetry associated with other cuts from the nominal value is taken as a systematic uncertainty. The relative systematic uncertainty is equal to $\Delta\alpha^{Sys} = 6.74\%$.
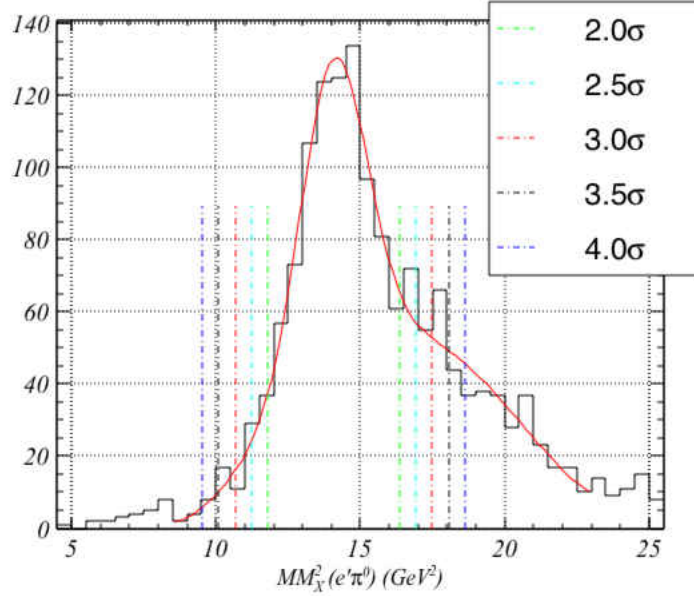
FIG. 74: The variations of $MM_X^2(e'\pi^0)$ cuts. The vertical-dashed lines indicate different cuts: 2σ, 2.5σ, 3.0σ ... . The nominal cut is shown by vertical red line.
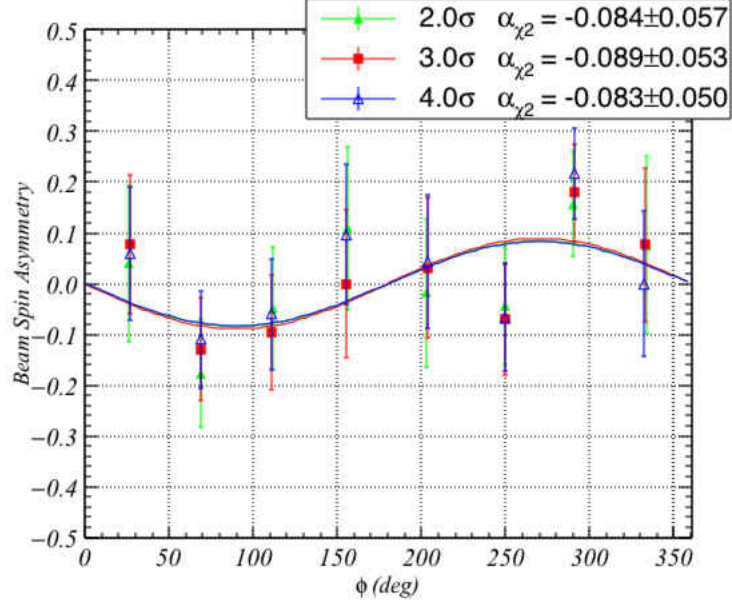
FIG. 75: Systematic uncertainty results for different cuts on Missing Mass Squared of $(e'^4He'\pi^0)$. The beam-spin asymmetry is calculated for each ϕ bin and fitted with $\alpha\sin(\phi)$.

TABLE 12: Systematic uncertainties measured by altering from Missing Mass Squared variable

variation	α	$\Delta\alpha_{sys}$
2.0σ	-0.084	0.005
2.5σ	-0.087	0.002
3.0σ	-0.089	
3.5σ	-0.091	0.002
4.0σ	-0.083	0.006

7.2.2 SYSTEMATIC UNCERTAINTY STUDY BY VARYING THE DISTANCE BETWEEN TWO PHOTONS ON IC

In Fig. 76, the distribution of the invariant mass of two photons versus distance between hit position's of photons on IC is shown. The distance has been varied from 6 cm to 8 cm with 0.5 cm steps which is represented by vertical-dashed lines. For each step, the obtained data were binned in ϕ and fitted with the $\alpha \sin(\phi)$ function to measure the asymmetry as illustrated in Fig. 77. The extracted asymmetry for each cut is summarized in Table 13. The systematic uncertainty associated with the distance is $(\Delta \alpha)^{Sys} = 20\%$.
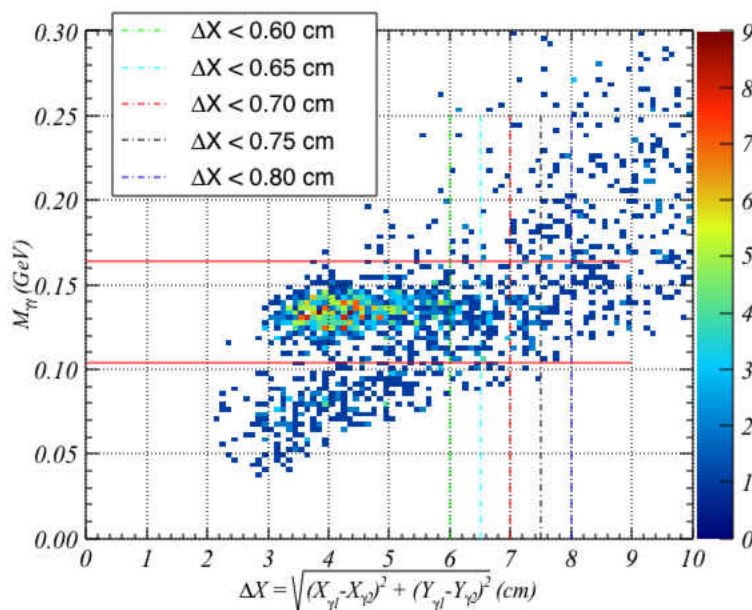
FIG. 76: The variations of ΔX cuts. The vertical-dashed lines indicate different cuts: 0.60 cm, 0.65 cm, 0.70 cm ... . The nominal cut is shown by vertical red line.
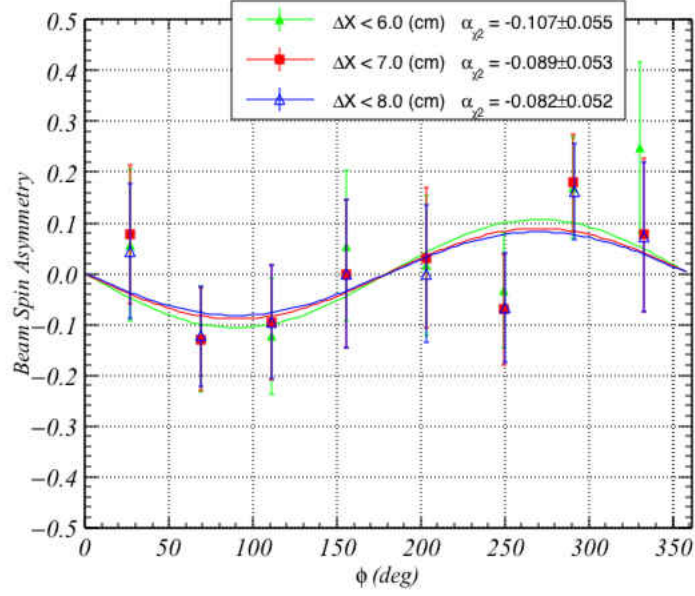
FIG. 77: Systematic uncertainty results for different ΔX. The beam-spin asymmetry is calculated for each ϕ bin and fitted with $\alpha \sin(\phi)$.

TABLE 13: Systematic uncertainties obtained by altering the distance between two photons on IC

variation	α	$\Delta\alpha_{sys}$
$\Delta X < 6.0$	-0.107	0.018
$\Delta X < 6.5$	-0.097	0.008
$\Delta X < 7.0$	-0.089	
$\Delta X < 7.5$	-0.080	0.009
$\Delta X < 8.0$	-0.082	0.007

7.2.3 SYSTEMATIC UNCERTAINTY BY VARIATION OF MINIMUM ENERGY OF SLOWER PHOTON

A similar analysis was done by changing the minimum energy cut of the slower photon. The invariant mass of two photons versus energy of the slower photon is shown in Fig. 78. The vertical-dashed lines represent the cuts and horizontal red-solid lines are 3σ cuts of the invariant mass. The asymmetry versus ϕ angle for each point is plotted in Fig. 79 for different cuts of the photon energy. The summary of the asymmetries extracted by changing the minimum energy is listed in Table 14. The systematic uncertainty is estimated as $(\Delta\alpha)^{Sys} = 4.5\%$.
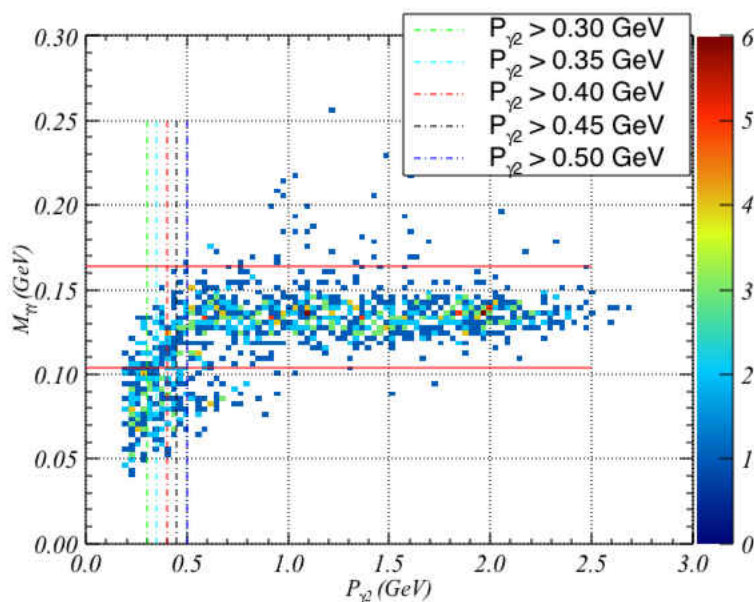
FIG. 78: The variations of $P_{\gamma 2}$ cuts. The vertical-dashed lines indicate different cuts: 0.30 GeV, 0.35 GeV, 0.40 GeV ... . The nominal cut is shown by vertical red line.
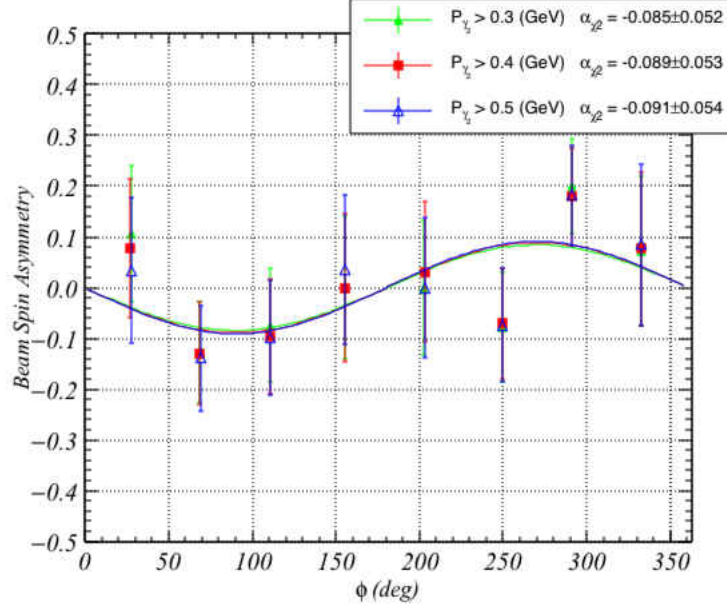
FIG. 79: Systematic uncertainty results for different cuts on $P_{\gamma 2}$. The beam-spin asymmetry is calculated for each ϕ bin and fitted with $\alpha \sin(\phi)$.

TABLE 14: Systematic uncertainties measured by altering the minimum energy of the slower photon

variation	α	$\Delta\alpha_{sys}$
$P_{\gamma 2} > 0.30$	-0.085	0.004
$P_{\gamma 2} > 0.35$	-0.092	0.003
$P_{\gamma 2} > 0.40$	-0.089	0.000
$P_{\gamma 2} > 0.45$	-0.091	0.002
$P_{\gamma 2} > 0.50$	-0.091	0.002

7.2.4 SYSTEMATIC UNCERTAINTY FROM FITTING

To extract the beam-spin asymmetry, a χ^2 fitting method was performed. In this section, the un-binned maximum likelihood fitting technique and its advantages will be discussed. The results will be compared with the χ^2 method of fitting and the extracted asymmetry difference between these two methods will be taken as a systematic uncertainty.

7.2.5 UN-BINNED MAXIMUM LIKELIHOOD METHOD

We assume an experiment that performed N independent measurements to obtain a value of a dependent variable $y_i(x_i)$ on an independent variable x_i space, where i counts from 1 to N. Let the distribution of the x_i variable be known and follow a *probability density function,* $f(\alpha; x)$, where α is a set of unknown parameters. The product of these *pdf* functions for each event is called likelihood function:

$$\mathcal{L}(\alpha) = \prod_{i=1}^{N} f(\alpha; x_i) \tag{78}$$

If the functional form of $f(\alpha; x_i)$ is known, one can estimate the maximum likelihood values of the unknown parameters by minimizing $\mathcal{L}(\alpha)$ with respect to the parameters [41]. It is more convenient to work with a negative logarithm of likelihood function.

$$-\frac{\delta log \mathcal{L}(\alpha)}{\delta \alpha} = -\frac{\delta \sum_{i=1}^{N} log(f(\alpha; x_i))}{\delta \alpha} = 0 \tag{79}$$

The difficult and important part of the un-binned likelihood method is to find the functional form of the *probability density functions.* In this part of the analysis, we will discuss the application of this method to extract the beam-spin asymmetry. The cross-section of the polarized lepton and proton reaction is:

$$\sigma = \sigma_{UU} + P_L^B \sigma_{LU} + P_L^T \sigma_{UL} + P_L^B P_L^T \sigma_{LL} + P_T^T \sigma_{UT} + P_L^B P_T^T \sigma_{LT} \tag{80}$$

where the superscript of $P^{B(T)}$ corresponds to beam (target). The polarization status of beam and target are represented by U (unpolarized), L (longitudinally) and T transversely polarized.

In this experiment, longitudinally polarized beam and unpolarized *helium*-4 was used as a target. Therefore, $P_L^T = 0$ and the equation (80) reduces to:

$$\sigma = \sigma_{UU} + P_L^B \sigma_{LU} \tag{81}$$

The reaction rate of the experiment will be:

$$\delta N = L\epsilon\bar{\sigma}_{UU}[1 + A_{UU}^{cos(\phi)}cos(\phi) + A_{UU}^{cos(2\phi)}cos(2\phi) + P_L^B A_{LU}^{sin(\phi)}sin(\phi)] \tag{82}$$

where L is the luminosity, ϵ is the detector acceptance and $\bar{\sigma}_{UU}$ is the unpolarized cross section. In equation (82), the $A_{UU}^{cos(\phi)}$ and $A_{UU}^{cos(2\phi)}$ terms are ignored for simplification. Thus, the equation of the reaction rate will be:

$$\delta N = L\epsilon\bar{\sigma}_{UU}[1 + P_L^B A_{LU}^{sin(\phi)}sin(\phi)] \tag{83}$$

In order to get *pdf*, one needs to get normalization factor of the equation (83).

$$N = \int_0^{2\pi} \delta N = L\epsilon\bar{\sigma}_{UU}[\delta\phi - P_L^B A_{LU}^{\sin(\phi)}\cos(\phi)]_0^{2\pi} = L\epsilon\bar{\sigma}_{UU}2\pi \tag{84}$$

Then, the *probability density function* of interest will be:

$$f(\alpha;\phi) = \frac{\delta N}{N} = \frac{1 + P_L^B A_{LU}^{sin(\phi)}sin(\phi)}{2\pi} \tag{85}$$

where $A_{LU}^{\sin(\phi)}$ is the amplitude of the beam-spin asymmetry and denoted by α in this analysis.

$$A_{LU}^{sin(\phi)} \equiv \alpha \tag{86}$$

The final likelihood function that needs to be minimized in order to estimate maximum values of the asymmetry is:

$$-log\mathcal{L} = -\sum_{i=1}^{N} log(1 + \alpha P_L^B sin(\phi_i)) + Nlog(2\pi) \tag{87}$$

The neutral pion production data were fitted with both χ^2 and un-binned likelihood method. The results are shown in Fig. 80. The solid red line represents χ^2 fitting result while dashed red line corresponds to the un-binned fitting method. The results of two different fitting methods show a good level of agreement. The difference of the results is taken as a source of the systematic uncertainty which is equal to $\Delta\alpha_{sys} = 14.6\%$.

7.2.6 SYSTEMATIC UNCERTAINTY FROM POLARIZATION OF BEAM

A Moller polarimeter measures the angular distributions of Moller electrons to obtain the beam polarization. In eg6 experiment, the beam polarization was measured several times during the run period by the Hall B Moller polarimeter. The polarization measurements
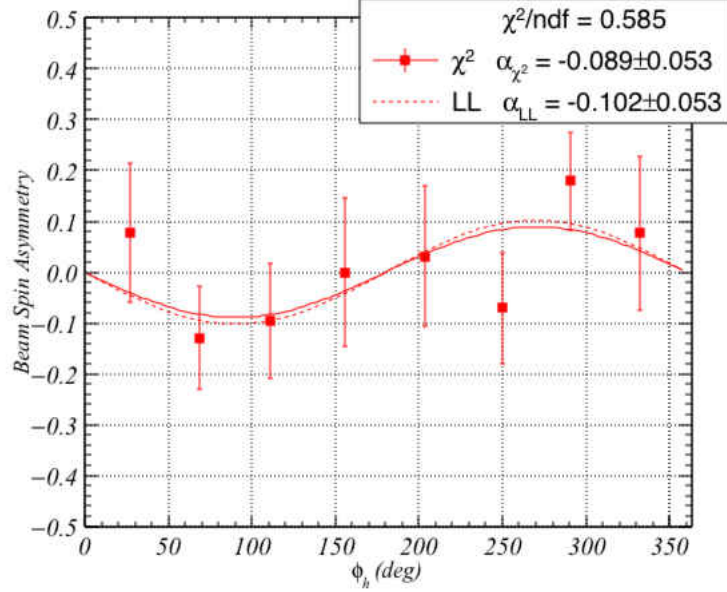
FIG. 80: Systematic uncertainty results for different cuts on Missing Mass Squared of $(e'^4 He'\pi^0)$. The beam-spin asymmetry is calculated for each ϕ bin and fitted with $\alpha \sin(\phi)$.

have been fitted with a linear function to obtain the average value $(P_B \approx 83.67\%)$ for 6 GeV run period as shown in Fig. 81. A global estimated error of the polarization is 3.5% which results in relative $\Delta\alpha^{Sys} = 3.5\%$ systematic error in the measured asymmetry.

7.2.7 SUMMARY OF SYSTEMATIC UNCERTAINTIES

The total relative systematic error is estimated as $\Delta\alpha^{Sys} = \sqrt{\sum_i^N (\Delta\alpha_i^{Sys})^2}$ where N is the number of uncertainty sources and i represents individual source of uncertainty. The summary of the systematic uncertainties is shown in Table 15 which is estimated as $\Delta\alpha^{Sys} = 26.3\%$.

FIG. 81: The beam polarization of the eg6 experiment during the run period [42].

TABLE 15: Summary of the relative systematic uncertainties for the measured beam-spin asymmetry in coherent channel.

variation	$\Delta\alpha_{sys}$
MM_X^2	6.7%
ΔX	20.0%
$P_{\gamma 2}$	4.5%
Beam polarization	3.5%
Fitting method	14.6%
Total	26.3%

CHAPTER 8
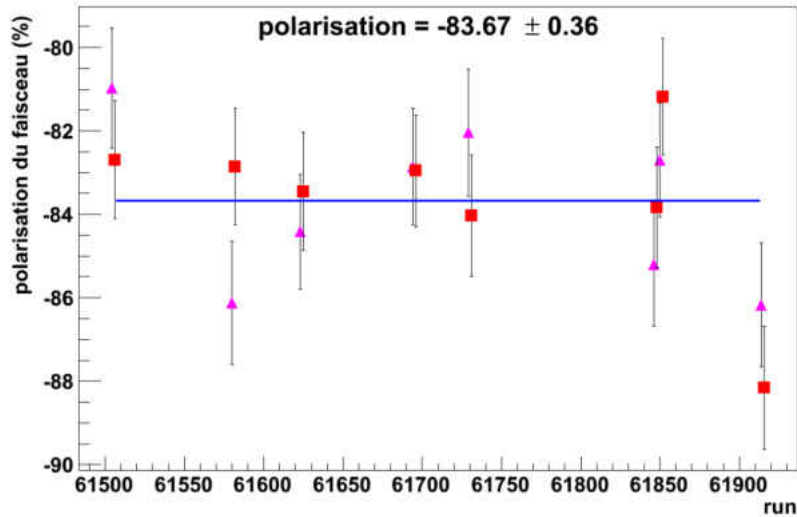
DISCUSSION AND CONCLUSION

The analysis presented in this work is the first measurement of the beam-spin asymmetry in coherent electroproduction of neutral pions off a helium-4 target in the deep exclusive regime at $Q^2 = 1.50$ GeV^2, $x_B = 0.18$ and $-t = 0.14$ GeV^2. The experiment was carried out in the experimental Hall B at Thomas Jefferson National Accelerator Facility. In this experiment, the 6 GeV longitudinally polarized electron beam was scattered of a 20 cm long helium-4 gas target. The data were collected in 2009 over a period of three months. All produced final state particles were detected by using the large acceptance CLAS detector package. In addition to CLAS, a RTPC was used to detect low momentum recoil α particles and the IC was used to detect small polar angle photons.

The beam-spin asymmetries was fitted as a function of the azimuthal angle ϕ which is the angle between leptonic and hadronic planes. The fitting function $\alpha \sin(\phi)$ obtained from Eqn. (41) was used to extract the asymmetry. The systematic uncertainties have been studied by varying the event selection cuts and using different fitting methods. One of the cuts that has the largest contribution to the systematic error was the opening angle between the two photons since this cut reduces background the most. Another large systematic uncertainty was estimated by comparing different fitting methods. In the least-square fitting method, the beam-spin asymmetry was extracted by binning the events in ϕ angle which may result in insufficient data to satisfy the necessity of Gaussian statistics for each bin due to limited statistics. However, in the un-binned likelihood method, the asymmetry was extracted event by event which may have advantages over least-square method in low statistics.

In this analysis, the non-zero beam-spin asymmetry was measured in the coherent electro-production of π^0 off a helium-4. This non-zero asymmetry arises from the $\sigma_{LT'}$. In order to extract the longitudinal cross section in the deep exclusive regime considered here which can be expressed in terms of the GPDs, it is necessary to perform L/T separation. The beam-spin asymmetries for the exclusive π^0 electroproduction of the proton were previously measured in the CLAS experiment [25]. The beam-spin asymmetry of the neutral pion production on a helium-4 has opposite sign comparing to the asymmetry measured on π^0 production on the proton. Further studies of the beam-spin asymmetry of the π^0 electroproduction on a helium-4 in the incoherent channel with limited statistics indicate that the asymmetries

have opposite sign in comparison between coherent and incoherent π^0 electroproduction on a helium-4.

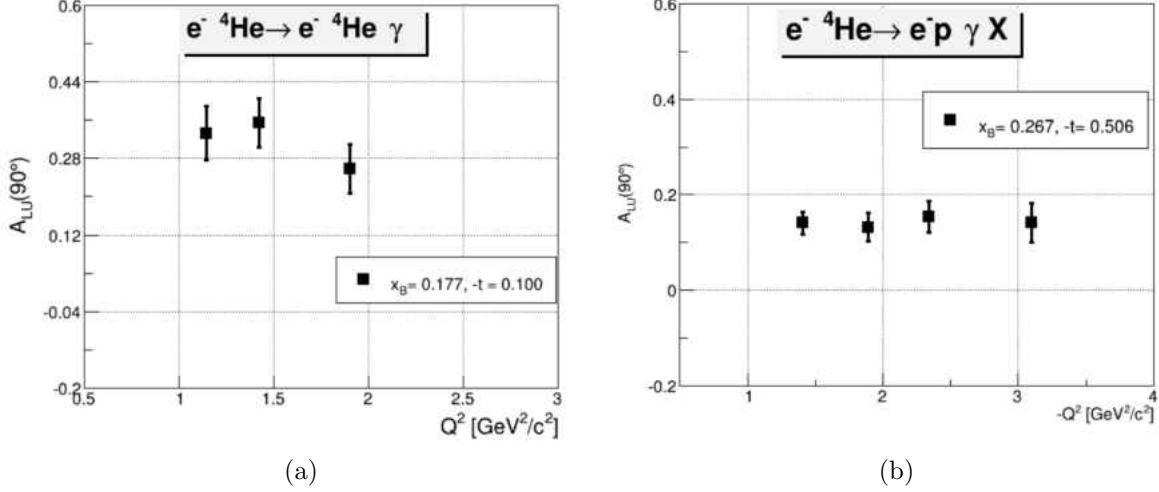(a)   (b)

FIG. 82: The extracted beam-spin asymmetries in coherent (left) and incoherent (right) DVCS as a function of Q^2 [34].

In addition, the beam-spin asymmetries have been measured in the deep exclusive photon electroproduction processes in both coherent and incoherent channels [34]. In Fig. 82, the extracted asymmetries of coherent (left histogram) and incoherent (right histogram) DVCS as a function of the Q^2 have been shown. Unlike neutral pion production process, the asymmetries in the photon production process have the same sign comparing coherent and incoherent photon production processes. In the theoretical side, it is being worked on Regge-based model by Jean-Marc Laget to understand the non-zero asymmetry.

BIBLIOGRAPHY

[1] A. W. Thomas and W. Weise, *The Structure of the Nucleon*, (Wiley-VCH, 2001).

[2] R. Hofstadter and R. McAllister, Phys. Rev. **98**, 217 (1955).

[3] R. Hofstadter, Rev. Mod. Phys. **28**, 214 (1956).

[4] M. Gell-Mann, Phys. Lett. **8**, 214 (1964).

[5] S. D. Drell and J. D. Walecka, Annals Phys. **28**, 1 (1964)

[6] J. Beringer et al. Phys. Rev. D **86**, 10001 (2012).

[7] A.V. Radyushkin, Phys. Lett. B**380**, 417 (1996).

[8] X. Ji, Phys. Rev. Lett **78**, 610 (1997).

[9] D. Muller, D. Robaschik, B.Geyer, F.M. Dittes and J.D. Horejsi, Fortsch. Phys. **42**, 101 (1994).

[10] J.C. Collins and A. Freund, Phys. Rev. D**59**, 074009 (1999).

[11] J.C. Collins, L. Frankfurt and M. Strikman, Phys. Rev. D**56**, 2982 (1997).

[12] P. Hoodboy and X. Ji, Phys. Rev. D**58**, 054006 (1998).

[13] M. Diehl, Phys. Rep. **388**, 41 (2003).

[14] K. Goeke, M.V. Polyakov and M. Vanderhaeghen, Nucl. Phys. **47**, 401 (2001).

[15] S. V. Goloskov and P. Kroll, Eur. Phys. J. C **65**, 137 (2010).

[16] S. V. Goloskov and P. Kroll, Eur. Phys. J. A **47**, 112 (2011).

[17] S. Ahmad, G. R. Goldstein and S. Luiti, Phys. Rev. D **79**, 054014 (2009).

[18] I. Bedlinskiy et al. (CLAS Collaboration), Phys. Rev. Lett. **109**, 112001 (2012).

[19] I. Bedlinskiy et al. (CLAS Collaboration), Phys. Rev. Lett. C **90**, 025205 (2014).

[20] M. Guidal. J. M. Laget and M. Vanderhaeghen, Nucl. Phys. A **627**, 645 (1997)

[21] J. M. Laget, Phys. Rev. C **73**, 044003 (2006).

[22] J. M. Laget, Phys. Lett. B **685**, 146 (2010).

[23] A. S. Raskin and T. W. Donnelly, Annals Phys. **191**, 78 (1989).

[24] S. Ahmad, G.R. Goldstein and S. Liuti, Phys. Rev. D $textbf$79, 054014 (2009).

[25] R. De Masi et al. (CLAS Collaboration), Phys. Rev. C **77**, 042201 (2008)

[26] B. A. Mecking et al. Nucl. Inst. and Meth. A **503**, 513 (2003).

[27] M. D. Mestayer et al. Nucl. Inst. and Meth. A **449**, 81 (2000).

[28] G. Adams et al. Nucl. Inst. and Meth. A **465**, 414 (2002).

[29] E. S. Smith et al. Nucl. Inst. and Meth. A **443**, 265 (1999).

[30] M. Amaryan et al. Nucl. Inst. and Meth. A **460**, 239 (2001).

[31] R. Niyazov and S. Stepanyan CLAS Note 2005-007 (2005).

[32] H. Fenker et al. Nucl. Inst. and Meth. A **592**, 273 (2008)

[33] S. Tkachenko et al. Phys. Rev. C **89**, 045206 (2014).

[34] M. Hattawy, *Deeply virtual Compton scattering off* ^4He, (Ph.D Thesis, Universite Paris-Sud XI, 2015).

[35] M. Mestayer CLAS Note 2006-015 (2006).

[36] R. De Masi et al. CLAS Note 1999-018 (1999).

[37] N. Baltzell CLAS Note 2013-009 (2013).

[38] N. Baltzell CLAS Note 2013-009 (2013).

[39] N. Baltzell CLAS Note 2013-008 (2013).

[40] C. Patrignani et al. Chin. Phys. C, **40**, 100001 (2016).

[41] P. R. Bevington and D. K. Robinson, *Data Reduction and Error Analysis for the Physical Sciences* (The McGraw-Hill Companies, Inc., New York, 1992)

[42] Y. Perrin, *Etude de la structure partonique du noyau dehlium*, (Ph.D Thesis, Universite De Grenoble 2012).

[43] F. -X. Girod et al. CLAS Note 2007-026 (2007).

VITA

Bayram Torayev

Department of Physics

Old Dominion University

Norfolk, VA 23529

EDUCATION

    2007-2009   **M.S.** Physics, Old Dominion University

    2002-2007   **B.A.** Physics, Middle East Technical University, Ankara/TURKEY

TEACHING EXPERIENCE

    2007-2009   Teaching Assistant *Old Dominion University*

RESEARCH EXPERIENCE

    2009-Present   **Graduate Research Assistant** *Old Dominion University*

- **Experiment E07-009:** Meson spectroscopy in the Coherent Production on ^{4}He with CLAS

- **Experiment E08-024:** Deeply Virtual Compton Scattering off ^{4}He

Typeset using LaTeX.